Analysis of High Pressure H_2/O_2, H_2/Air and $Kerosene/Air$ Reacting Shear Flows

---

A PhD Dissertation
Presented to
the Graduate School of
Clemson University

In Partial Fulfillment
of the Requirements for the Degree
PhD
Mechanical Engineering

---

by
Ayse Korucu
December 2016

Accepted by:
Dr. Richard S. Miller, Committee Chair
Dr. Donald E. Beasley
Dr. Richard S. Figliola
Dr. Xiangchun Xuan

Abstract

Direct Numerical Simulation (DNS) data for high pressure H_2/O_2 and H_2/Air flames using the compressible flow formulation, detailed kinetics, a real fluid equation of state, and generalized diffusion are analyzed. The DNS is filtered over a range of filter widths to provide exact terms in the Large Eddy Simulation (LES) governing equations, including unclosed terms. The filtered heat flux vector is extensively compared with the heat flux vector calculated as a function of the filtered primitive variables (i.e. the exact LES term is compared with its form available within an actual LES). The difference between these forms defines the subgrid heat flux vector. The analyses are done both globally across the entire flame, as well as by conditionally averaging over specific regions of the flame; including regions of large subgrid kinetic energy, subgrid scalar dissipation, subgrid temperature variance, flame temperature, etc. In this work, both the subgrid heat flux vector and its divergence are found to be substantially larger in reacting flows in comparison with mixing due to the associated larger temperature gradients. However, the divergence of the subgrid heat flux vector tends to be significantly smaller than other unclosed terms in the energy equation with decreasing significance with increasing Reynolds number.

Then a reduced (29 step, 10 species) $Kerosene/Air$ mechanism including a semi-global soot formation/oxidation model associated with an optically thin medium radiative heat flux model has been added to the same code to investigate soot formation/oxidation processes in a temporarily developing hydrocarbon flame operating at both atmospheric and elevated pressures for a both real gas law (RGL) and the ideal gas law (IGL) equation of states (EOS). Good agreement with the limited literature of atmospheric pressure flames [97, 46, 45] has been achieved for both 3D the RGL and the IGL EOS predictions for the soot formation/oxidation process. High values of the soot volume fraction have

been shown to be independent from high temperature flame regions by occupying the flame volumes whose temperature varies from 1300 K to 1800 K. Additionally, the soot number density has been shown to be highly dependent on the temperature, while the soot volume fraction is dominated by local flow characteristics which is also in good agreement with Ref. [97]. Lignell at *el.* [46, 45] have reported two distinct behaviors of soot mass farction I- the slow soot nucleation process has caused the soot mass fraction to be widely scattered in the flame, and II - turbulent transportation has carried the soot to the fuel rich region by emphasizing the importance of the turbulence transportation in sooting flames. Similar behavior has been also observed in the current work. The soot generation rate has been shown to have a similar trend with soot mass fraction, while Lignell at *el.* [46, 45] have observed a high dependency on flame temperature for the soot generation rate.

Furthermore, a slight difference has been observed between the RGL and the IGL EOS model predictions of soot quantities in atmospheric pressure flames. This implies employing the IGL EOS might be reasonable to eliminate the complexity of mathematical models of real gas effects. However, at 35 atm, the IGL EOS model has been shown to extremely over-predict not only the flame temperature but also the soot quantities by 25% to 100% in comparison with the RGL EOS model predictions. In elevated pressure flames, a similar trend has been observed for the soot volume fractions and the soot number density, while high values of the soot mass fraction exhibits a less scattered profile in the mixture fraction coordinate which is limited in the range of ϕ =0.4 to 0.9. The soot generation rate has been observed to a have smaller standard deviation than its means in elevated pressure flames, while they have been observed to be larger than its means in atmospheric pressure flames. Additionally, like Lignell at *el.* [45] have reported due to the short simulation time, and small soot load in comparison to the domain size, radiative heat transfer is found to be insignificant. The radiative heat flux effect is needed to be analyzed artificially by increasing the Planck mean absorption coefficient of the optically thin medium model.

The unity Lewis (Le) number assumption on the soot formation/oxidation process has been studied in 2D DNS of atmospheric pressure flames for both the RGL and the IGL EOS models. The results have shown that the unity Le number assumption results under-predicting the soot quantities and the

flame temperature. The known effect of unity Le number on the enthalpy has been clearly seen in these atmospheric pressure flames. Ignoring Le number effects has been shown to under-predict the soot quantities by at least an order of magnitude. A further investigation of the unity Le number assumpton is required for 3D DNS at elevated pressures for both RGL and IGL EOS models.

After testing the validity of the current model with past literature, and revealing the importance of real gas effects on the soot formation/oxidation process, 2D DNS have been conducted to investigate pressure effects on the process in a much deeper manner. It has been known for decades that in hydrocarbon flames soot production has been increased by increased ambient pressure. Such a behavior has been noted in the current work by investigating flames of 1, 5, 10 and 35 atm with the RGL and the IGL EOS models. These predictions show the clear effects of pressure on the soot production/oxidation processes. For the first three pressures the IGL EOS model has not deviated from the RGL EOS model significantly. However, for the flames of 35 atm the differences becomes highly significant. In order to gain insight into effects of pressure on the process 3D DNS flames need to be studied with an artificially enhanced radiative heat flux model.

Table of Contents

Title Page . . . . . **i**

Abstract . . . . . **ii**

List of Tables . . . . . **vi**

List of Figures . . . . . **vii**

1 Introduction **1**

2 A Priori Analysis of Subgrid Scale Pressure and Heat Flux in High Pressure Mixing and Reacting Shear Layers **3**
2.1 Introduction 3
2.2 Objectives 5
2.3 Governing Equations 5
2.4 Subgrid Analysis 10

3 *Kerosene/Air* Reacting Shear Flows Including Soot Formation/Oxidation With Radiative Heat Transfer **22**
3.1 Introduction 22
3.2 Objectives 24
3.3 Chemical Kinetics and Numerical Approach 25
3.4 Soot Model 28
3.5 Radiation Model 31
3.6 Real Gas and Pressure Effects on Soot Formation Including Radiative Heat Transfer . 33
3.7 Results 38

4 Differential Diffusion and Equation of State Effects on Soot Production/Oxidation Process in Kerosene/Air Shear Flames **75**
4.1 Introduction 75
4.2 Objectives 77
4.3 Results 78

5 Conclusions and Future Work **111**

Bibliography **113**

List of Tables

2.1 Summary of simulation parameters from all cases considered. P_0 is initial pressure, T_0 is the initial temperature, Re_0 the initial Reynolds number, $Re_\delta(t_f)$ the Reynolds number calculated based on the vorticity thickness at the final simulation time, N_2, N_2, N_3 are the number of grid points in the x_1, x_2, x_3 direction respectively, and t_f^* is non-dimensionlized final simulation time. 9
2.2 The local regions within which statistical analyses have been done. 11
2.3 Filtering diameter size used to postprocess the DNS data. 'Run' corresponds to the DNS cases presented in Table 2.1, $\Delta_1 = 3\delta_{\omega 0}$ is the spherical filter diameter this work focuses on, Δx_1 is the DNS grid spacing in the x_1 direction, $\delta_{\omega 0}$ is the DNS initial vorticity thickness, $(N_1 \times N_2 \times N_3)_{LES}$ are the equivalent LES grid resolutions in x_1, x_2, and x_3 directions, respectively, for, $\Delta_1 = 3\delta_{\omega 0}$. 13

3.1 Kerosene quasi global combustion kinetics mechanism [94]. 26
3.2 Comparison of thermophysical−chemical characterization of model fuel with reported data [94]. 27
3.3 Thermodynamic coefficients for C_P of $C_{12}H_{24}$[94]. 27
3.4 Summary of simulation parameters from all cases considered. P_0 is initial pressure, T_0 is the initial temperature, Re_0 the initial Reynolds number, N_1, N_2 and N_3, are the number of grid points in the x_1, x_2, and x_3, direction respectively, and t_f^* is non-dimensionalized final simulation time. 28
3.5 The coefficients used to calculate Planck mean absorption coefficient of H_2O and CO_2 [1]. 32
3.6 The coefficients used to calculate Planck mean absorption coefficient of CO [1]. . . . 32
3.7 The density and compressibility of $C_{12}H_{24}$ at 1, 5, 10 and 35 atm flames. 61

4.1 Summary of simulation parameters from all cases considered. P_0 is initial pressure, T_0 is the initial temperature, Re_0 the initial Reynolds number, N_1, N_2, are the number of grid points in the x_1, x_2 direction, respectively, and t_f^* is non-dimensionalized final simulation time. 78
4.2 Summary of simulation parameters from all cases considered. P_0 is initial pressure, T_0 is the initial temperature, Re_0 the initial Reynolds number, N_1, N_2 and N_3, are the number of grid points in the x_1, x_2, and x_3, direction respectively, and t_f^* is non-dimensionalized final simulation time. 78
4.3 Summary of simulation parameters from all cases considered. P_0 is initial pressure, T_0 is the initial temperature, Re_0 the initial Reynolds number, N_1, N_2 and N_3, are the number of grid points in the x_1, x_2, and x_3, direction respectively, and t_f^* is non-dimensionalized final simulation time. 108

List of Figures

2.1 Direct Numerical Simulation domain schematic 6
2.2 PDFs of $|\overline{Q_j(\Psi)}|/|Q_j(\overline{\Psi})|$, conditioned on: (a) $0.01 \leq \phi \leq 0.99$, (b) the stoichiometric surface, (c) $\dot{\omega}^{OH}/E(\dot{\omega}^{OH} \geq 2)$. 16
2.3 PDFs of $|\overline{\partial Q_j(\Psi)/\partial x_j}|/|\partial Q_j(\overline{\Psi})/\partial x_j|$, conditioned on: (a) $0.01 \leq \phi \leq 0.99$, (b) the stoichiometric surface, (c) $\dot{\omega}^{OH}/E(\dot{\omega}^{OH} \geq 2)$. 17
2.4 PDFs of $|Q_{sgs_j}|/|(\rho e_t u_j)_{sgs}|$, conditioned on: (a) $0.01 \leq \phi \leq 0.99$, (b) the stoichiometric surface, and (c) $\dot{\omega}^{OH}/E(\dot{\omega}^{OH} \geq 2)$. 18
2.5 PDFs of $|\partial Q_{sgs_j}/\partial x_j|/|\partial(\rho e_t u_j)_{sgs}/\partial x_j|$, conditioned on: (a) $0.01 \leq \phi \leq 0.99$, (b) the stoichiometir surface, and (c) $\dot{\omega}^{OH}/E(\dot{\omega}^{OH} \geq 2)$. 19
2.6 PDFs of $|Q_{sgs_j}|/|(Pu_j)_{sgs}|$, conditioned on: (a) $0.01 \leq \phi \leq 0.99$, (b) the stoichiometric surface, and (c) $\dot{\omega}^{OH}/E(\dot{\omega}^{OH} \geq 2)$. 20
2.7 PDFs of $|\partial Q_{sgs_j}/\partial x_j|/|\partial(Pu_j)_{sgs}/\partial x_j|$, in regions described by: (a) $0.01 \leq \phi \leq 0.99$, (b) the stoichiometric surface, and (c) $\dot{\omega}^{OH}/E(\dot{\omega}^{OH} \geq 2)$. 21

3.1 On the left the RGL EOS model and on the right the IGL EOS model predictions of $< T/T_0|\phi >$ for Re= 2500, Le $\neq$ 1, and 1 atm ambient pressure at time of 65. 40
3.2 On the left the RGL EOS model and on the right the IGL EOS model predictions of $< fv|\phi >$ for Re= 2500, Le $\neq$ 1, and 1 atm ambient pressure at time of 65. 41
3.3 On the left the RGL EOS model and on the right the IGL EOS model predictions of $< N|\phi >$ for Re= 2500, Le $\neq$ 1, and 1 atm ambient pressure at time of 65. 41
3.4 On the left the RGL EOS model and on the right the IGL EOS model predictions of $< Ys|\phi >$ for Re= 2500, Le $\neq$ 1, and 1 atm ambient pressure at time of 65. 42
3.5 On the left the RGL EOS model and on the right the IGL EOS model predictions of $< \chi|\phi >$ for Re= 2500, Le $\neq$ 1, and 1 atm ambient pressure at time of 65. 42
3.6 On the left the RGL EOS model and on the right the IGL EOS model predictions of $< w_{soot}|\phi >$ for Re= 2500, Le $\neq$ 1, and 1 atm ambient pressure at time of 65. 43
3.7 Contour plots of T(K) for pressure 1 atm, Le$\neq$1 and Re=2500, top is the RGL model and bottom is the IGL EOS model predictions time of 65, 3D data. 44
3.8 Contour plots of fv for pressure 1 atm, Le$\neq$1 and Re=2500, top is the RGL model and bottom is the IGL EOS model predictions time of 65, 3D data. 45
3.9 Contour plots of Ys for pressure 1 atm, Le$\neq$1 and Re=2500, top is the RGL model and bottom is the IGL EOS model predictions time of 65, 3D data. 46
3.10 On the left the RGL EOS model and on the right the IGL EOS model predictions of $< T/T_0|\phi >$ for Re= 2500, Le $\neq$ 1, and 5 atm ambient pressure at time of 80. 48

3.11 On the left the RGL EOS model and on the right the IGL EOS model predictions of$< fv|\phi >$ for Re= 2500, Le $\neq$ 1, and 5 atm ambient pressure at time of 80. 48
3.12 On the left the RGL EOS model and on the right the IGL EOS model predictions of $< N|\phi >$ for Re= 2500, Le $\neq$ 1, and 5 atm ambient pressure at time of 80. 49
3.13 On the left the RGL EOS model and on the right the IGL EOS model predictions of $< Ys|\phi >$ for Re= 2500, Le $\neq$ 1, and 5 atm ambient pressure at time of 80. 49
3.14 On the left the RGL EOS model and on the right the IGL EOS model predictions of $< \chi|\phi >$ for Re= 2500, Le $\neq$ 1, and 5 atm ambient pressure at time of 80. 50
3.15 On the left the RGL EOS model and on the right the IGL EOS model predictions of $< w_{soot}|\phi >$ for Re= 2500, Le $\neq$ 1, and 5 atm ambient pressure at time of 80. 50
3.16 On the left the RGL EOS model and on the right the IGL EOS model predictions of $< T/T_0|\phi >$ for Re= 2500, Le $\neq$ 1, and 5 atm ambient pressure at time of 80 radiation included. 51
3.17 On the left the RGL EOS model and on the right the IGL EOS model predictions of$< fv|\phi >$ for Re= 2500, Le $\neq$ 1,and 5 atm ambient pressure at time of 80 radiation included. 51
3.18 On the left the RGL EOS model and on the right the IGL EOS model predictions of $< N|\phi >$ for Re= 2500, Le $\neq$ 1, and 5 atm ambient pressure at time of 80 radiation included. 52
3.19 On the left the RGL EOS model and on the right the IGL EOS model predictions of $< Ys|\phi >$ for Re= 2500, Le $\neq$ 1, and 5 atm ambient pressure at time of 80 radiation included. 52
3.20 On the left the RGL EOS model and on the right the IGL EOS model predictions of $< \chi|\phi >$ for Re= 2500, Le $\neq$ 1, and 5 atm ambient pressure at time of 80 radiation included. 53
3.21 On the left the RGL EOS model and on the right the IGL EOS model predictions of$< w_{soot}|\phi >$ for Re= 2500, Le $\neq$ 1, and 5 atm ambient pressure at time of 80 radiation included. 53
3.22 On the left the RGL EOS model and on the right the IGL EOS model predictions of $< T/T_0|\phi >$ for Re= 2500, Le $\neq$ 1, and 10 atm ambient pressure at time of 80. 54
3.23 On the left the RGL EOS model and on the right the IGL EOS model predictions of$< fv|\phi >$ for Re= 2500, Le $\neq$ 1, and 10 atm ambient pressure at time of 80. 55
3.24 On the left the RGL EOS model and on the right the IGL EOS model predictions of $< N|\phi >$ for Re= 2500, Le $\neq$ 1, and 10 atm ambient pressure at time of 80. 55
3.25 On the left the RGL EOS model and on the right the IGL EOS model predictions of $< Ys|\phi >$ for Re= 2500, Le $\neq$ 1, and 10 atm ambient pressure at time of 80. 56
3.26 On the left the RGL EOS model and on the right the IGL EOS model predictions of $< \chi|\phi >$ for Re= 2500, Le $\neq$ 1, and 10 atm ambient pressure at time of 80. 56
3.27 On the left the RGL EOS model and on the right the IGL EOS model predictions of $< w_{soot}|\phi >$ for Re= 2500, Le $\neq$ 1, and 10 atm ambient pressure at time of 80. 57
3.28 On the left the RGL EOS model and on the right the IGL EOS model predictions of $< T/T_0|\phi >$ for Re= 2500, Le $\neq$ 1, and 10 atm ambient pressure at time of 80 radiation included. 57

3.29 On the left the RGL EOS model and on the right the IGL EOS model predictions of$< fv|\phi >$ for Re= 2500, Le $\neq$ 1,and 10 atm ambient pressure at time of 80 radiation included. 58
3.30 On the left the RGL EOS model and on the right the IGL EOS model predictions of $< N|\phi >$ for Re= 2500, Le $\neq$ 1, and 10 atm ambient pressure at time of 80 radiation included. 58
3.31 On the left the RGL EOS model and on the right the IGL EOS model predictions of $< Ys|\phi >$ for Re= 2500, Le $\neq$ 1, and 10atm ambient pressure at time of 80 radiation included. 59
3.32 On the left the RGL EOS model and on the right the IGL EOS model predictions of $< \chi|\phi >$ for Re= 2500, Le $\neq$ 1, and 10 atm ambient pressure at time of 80 radiation included. 59
3.33 On the left the RGL EOS model and on the right the IGL EOS model predictions of $< w_{soot}|\phi >$ for Re= 2500, Le $\neq$ 1, and 10 atm ambient pressure at time of 80 radiation included. 60
3.34 On the left the RGL EOS model and on the right the IGL EOS model predictions of $< T/T_0|\phi >$ for Re= 2500, Le $\neq$ 1, and 35 atm ambient pressure at time of 70. 62
3.35 Contour plots of T(K) for pressure 35 atm, Le$\neq$1 and Re=2500, top is the RGL model and bottom is the IGL EOS model predictions time of 65, 3D data. 63
3.36 On the left the RGL EOS model and on the right the IGL EOS model predictions of $< fv|\phi >$ for Re= 2500, Le $\neq$ 1, and 35 atm ambient pressure at time of 65. 64
3.37 On the left the RGL EOS model and on the right the IGL EOS model predictions of $< N|\phi >$ for Re= 2500, Le $\neq$ 1, and 35 atm ambient pressure at time of 65. 64
3.38 Contour plots of fv for pressure 35 atm, Le$\neq$1 and Re=2500, top is the RGL model and bottom is the IGL EOS model predictions time of 65, 3D data. 65
3.39 Contour plots of Ys for pressure 35 atm, Le$\neq$1 and Re=2500, top is the RGL model and bottom is the IGL EOS model predictions time of 65, 3D data. 66
3.40 On the left the RGL EOS model and on the right the IGL EOS model predictions of $< Ys|\phi >$ for Re= 2500, Le $\neq$ 1, and 35 atm ambient pressure at time of 65. 67
3.41 On the left the RGL EOS model and on the right the IGL EOS model predictions of $< \chi|\phi >$ for Re= 2500, Le $\neq$ 1, and 35 atm ambient pressure at time of 65. 67
3.42 On the left the RGL EOS model and on the right the IGL EOS model predictions of $< w_{soot}|\phi >$ for Re= 2500, Le $\neq$ 1, and 35 atm ambient pressure at time of 65. 68
3.43 The comparison of RGL EOS model of $< T/T_0|\phi >$ for Re= 2500, Le $\neq$ 1, and 35 atm ambient pressure at time of 65 and 80. 68
3.44 The comparison the RGL EOS model predictions of $< fv|\phi >$ for Re= 2500, Le $\neq$ 1, and 35 atm ambient pressure at time of 65 and 80. 69
3.45 The comparison the RGL EOS model predictions of $< N|\phi >$ for Re= 2500, Le $\neq$ 1, and 35 atm ambient pressure at time of 65 and 80. 69
3.46 The comparison the RGL EOS model predictions of $< Ys|\phi >$ for Re= 2500, Le $\neq$ 1, and 35 atm ambient pressure at time of 65 and 80. 70
3.47 The comparison the RGL EOS model predictions of $< \chi|\phi >$ for Re= 2500, Le $\neq$ 1, and 35 atm ambient pressure at time of 65 and 80. 70
3.48 The comparison the RGL EOS model predictions of $< w_{soot}|\phi >$ for Re= 2500, Le $\neq$ 1, and 35 atm ambient pressure at time of 65 and 80. 71

3.49 The RGL and the IGL EOS pressure effects on mean variables Re=2500, left is RGL and right is IGL time of 80 2D data 72
3.50 Pressure effects on means of $< fv|\phi >$ for Re=2500, Le≠1 and 1 atm on the left the RGL model predictions and on the right the IGL model predictions time of 80 2D data 72
3.51 Pressure effects on means of $< Ys|\phi >$ for Re=2500, Le≠1 and 1 atm, on the left the RGL model predictions and on the right the IGL model predictions time of 80 2D data 73
3.52 The RGL and the IGL EOS pressure effects on mean variables Re=2500, left is RGL and right is IGL time of 80 2D data 73
3.53 The RGL and the IGL EOS pressure effects on mean variables Re=2500, left is RGL and right is IGL time of 80 2D data 74
3.54 Pressure effects on mean of $< Y_{OH}|\phi >$ for Re=2500, Le≠1 and 1 atm, on the left the RGL model predictions and on the right the IGL model predictions time of 80 2D data 74

4.1 On the left the RGL EOS model Le≠1 and on the right the RGL EOS model Le=1 predictions of $< T/T_0|\phi >$ for Re=2500, and 1 atm ambient pressure at time of 65. . 79
4.2 The comparison of contour plots of T(K) top is Le≠1 and bottom is Le=1 both coupled with the RGL EOS model for pressure 1 atm and Re=2500 at time of 65 predictions of 3D data. 80
4.3 On the left the RGL EOS model Le≠1 and on the right the RGL EOS model Le=1 predictions of $< fv|\phi >$ for Re= 2500, and 1 atm ambient pressure at time of 65. . . 81
4.4 The comparison of contour plots of fv for pressure 1 atm and Re=2500, top is Le=1 and bottom is l ≠1predictions time of 65 3D data. 82
4.5 On the left the RGL EOS model Le≠1 and on the right the RGL EOS model Le=1 predictions of $< N|\phi >$ for Re= 2500, and 1 atm ambient pressure at time of 65. . . . 83
4.6 On the left the RGL EOS model Le≠1 and on the right the RGL EOS model Le=1 predictions of $< Ys|\phi >$ for Re=2500, and 1 atm ambient pressure at time of 65. . . . 83
4.7 The comparison of contour plots of Ys for pressure 1 atm and Re=2500, top is Le=1 and bottom is l ≠1predictions time of 65 3D data. 84
4.8 On the left the RGL EOS model Le≠1 and on the right the RGL EOS model Le=1 predictions of $< \chi|\phi >$ for Re=2500, and 1 atm ambient pressure at time of 65. . . . 85
4.9 On the left the RGL EOS model Le≠1 and on the right the RGL EOS model Le=1 predictions of $< w_{soot}|\phi >$ for Re=2500, and 1 atm ambient pressure at time of 65. . . 85
4.10 On the left the IGL EOS model Le≠1 and on the right the IGL EOS model Le=1 predictions of $< T/T_0|\phi >$ for Re=2500, and 1 atm ambient pressure at time of 65. . 86
4.11 On the left the IGL EOS model Le≠1 and on the right the IGL EOS model Le=1 predictions of $< fv|\phi >$ for Re= 2500, and 1 atm ambient pressure at time of 65. . . 86
4.12 On the left the IGL EOS model Le≠1 and on the right the IGL EOS model Le=1 predictions of $< N|\phi >$ for Re= 2500, and 1 atm ambient pressure at time of 65. . . . 87
4.13 On the left the IGL EOS model Le≠1 and on the right the IGL EOS model Le=1 predictions of $< Ys|\phi >$ for Re=2500, and 1 atm ambient pressure at time of 65. . . . 87
4.14 On the left the IGL EOS model Le≠1 and on the right the IGL EOS model Le=1 predictions of $< \chi|\phi >$ for Re=2500, and 1 atm ambient pressure at time of 65. . . . 88
4.15 On the left the IGL EOS model Le≠1 and on the right the IGL EOS model Le=1 predictions of $< w_{soot}|\phi >$ for Re=2500, and 1 atm ambient pressure at time of 65. . . 88

4.16 On the left the RGL EOS model and on the right the IGL EOS model predictions of $< T/T_0|\phi >$ for Re=2500, Le =1, and 1 atm ambient pressure at time of 80, 3D DNS data. 89
4.17 The comparison of contour plots of T(K) for pressure 1 atm, Le=1 and Re=2500, top sub-figure is created the RGL EOS, and bottom one is created with the IGL EOS model at time of 80 for 3D data. 90
4.18 On the left the RGL EOS model and on the right the IGL EOS model predictions of $< fv|\phi >$ for Re=2500, Le =1, and 1 atm ambient pressure at time of 80, 3D DNS data. 91
4.19 The comparison of contour plots of fv for pressure1 atm, Le=1 and Re=2500, top sub-figure is created the RGL EOS, and bottom one is created with the IGL EOS model at time of 80 for 3D data. 92
4.20 On the left the RGL EOS model and on the right the IGL EOS model predictions of $< N|\phi >$ for Re=2500, Le =1, and 1 atm ambient pressure at time of 80, 3D DNS data. 93
4.21 On the left the RGL EOS model and on the right the IGL EOS model predictions of $< Ys|\phi >$ for Re=2500, Le =1, and 1 atm ambient pressure at time of 80, 3D DNS data. 93
4.22 The comparison of contour plots of Ys for pressure 1 atm, Le=1 and Re=2500, top sub-figure is created the RGL EOS, and bottom one is created with the IGL EOS model at time of 80 for 3D data. 94
4.23 On the left the RGL EOS model and on the right the IGL EOS model predictions of $< \chi|\phi >$ for Re=2500, Le =1, and 1 atm ambient pressure at time of 80, 3D DNS data. 95
4.24 On the left the RGL EOS model and on the right the IGL EOS model predictions of $< w_{soot}|\phi >$ for Re= 2500, Le =1, and 1 atm ambient pressure at time of 80, 3D DNS data. 95
4.25 On the left the RGL EOS model and on the right the IGL EOS model predictions of $< T/T_0|\phi >$ for Re=2500, Le =1, and 1 atm ambient pressure at time of 65, 2D DNS data. 96
4.26 On the left the RGL EOS model and on the right the IGL EOS model predictions of log10$< fv|\phi >$ for Re=2500, Le =1, and 1 atm ambient pressure at time of 80, 2D DNS data. 96
4.27 On the left the RGL EOS model and on the right the IGL EOS model predictions of $< Ys|\phi >$ for Re=2500, Le =1, and 1 atm ambient pressure at time of 80, 2D DNS data. 97
4.28 On the left the RGL EOS model and on the right the IGL EOS model predictions of $< Y_{CO}|\phi >$ for Re=2500, Le =1, and 1 atm ambient pressure at time of 80, 2D DNS data. 97
4.29 On the left the RGL EOS model and on the right the IGL EOS model predictions of $Y_H|\phi >$ for Re= 2500, Le =1, and 1 atm ambient pressure at time of 80, 2D DNS data. 98
4.30 On the left the RGL EOS model and on the right the IGL EOS model predictions of $< Y_{OH}|\phi >$ for Re= 2500, Le =1, and 1 atm ambient pressure at time of 80, 2D DNS data. 98
4.31 The comparison of $< T/T_0|\phi >$ for different ambient pressures, the EOS models and diffusion assumptions flames (a) 1 atm, (b) 5 atm, (c) 10 atm and (d) 35 atm ambient pressures. 100
4.32 The comparison of $< fv|\phi >$ for different ambient pressures, the EOS models and diffusion assumptions flames (a) 1 atm, (b) 5 atm, (c) 10 atm and (d) 35 atm ambient pressures. 102

4.33 The comparison of $< Y_s|\phi >$ for different ambient pressures, the EOS models and diffusion assumptions flames (a) 1 atm, (b) 5 atm, (c) 10 atm and (d) 35 atm ambient pressures. 103
4.34 The comparison of $< Y_H|\phi >$ for different ambient pressures, the EOS models and diffusion assumptions flames (a) 1 atm, (b) 5 atm, (c) 10 atm and (d) 35 atm ambient pressures. 105
4.35 The comparison of $< Y_{OH}|\phi >$ for different ambient pressures, the EOS models and diffusion assumptions flames (a) 1 atm, (b) 5 atm, (c) 10 atm and (d) 35 atm ambient pressures. 106
4.36 The comparison of $< Y_{CO}|\phi >$ for different ambient pressures, the EOS models and diffusion assumptions flames (a) 1 atm, (b) 5 atm, (c) 10 atm and (d) 35 atm ambient pressures. 107
4.37 On the left the RGL EOS model and on the right the IGL EOS model Le number calculated for the adiabatic atmospheric pressure flame. 108
4.38 On the left the RGL EOS model and on the right the IGL EOS model Le number calculated for the adiabatic 5 atm pressure flame. 109
4.39 On the left the RGL EOS model and on the right the IGL EOS model Le number calculated for the adiabatic 10 atm pressure flame. 109
4.40 On the left the RGL EOS model and on the right the IGL EOS model Le number calculated for the adiabatic 35 atm pressure flame. 110

Chapter 1

A Priori Analysis of Subgrid Scale Pressure and Heat Flux in High Pressure Mixing and Reacting Shear Layers

1.1 Introduction

To simulate practical reacting flows, which are often accompanied by high Reynolds numbers and complex geometry, Large Eddy Simulation (LES) is quickly becoming widely used [28, 30, 71, 35]. In LES, each primitive variable is filtered into a 'resolved' scale plus a subgrid scale fluctuating component; mathematically represented by $\Phi = \bar{\Phi} + \Phi'$. The LES governing equations yield several unclosed terms that may require modeling as they contain unresolved information about the subgrid scales. Of these unclosed terms, the filtered chemical reaction rate, $\overline{S_{Y_\alpha}}$, and subgrid turbulent stresses, $\Pi_{ij} = \overline{\rho u_i u_j} - \overline{\rho}\langle\langle u_i \rangle\rangle\langle\langle u_j \rangle\rangle$, have received the most attention [43, 70, 78, 71, 72]. Here, $\langle\langle . \rangle\rangle$ indicates density weighted Favre filtering that can be related to the standard filtering by the following expression, $\langle\langle \Phi \rangle\rangle = \overline{\rho\Phi} \,/\overline{\rho}$. Decomposition of a Favre filtered instantaneous variable includes the Favre filtered component plus a fluctuating component, $\Phi = \langle\langle \Phi \rangle\rangle + \Phi''$.

In addition to these unclosed terms, the filtered heat flux vector, $\overline{Q_j(\Psi)}$, may also be unclosed terms depending on the formulation, where Ψ is the set of composition variables (mass fraction, Y_α

temperature, T, density, ρ, etc.). Few previous studies regarding $\overline{Q_j(\Psi)}$ in the total energy equation exist. Subgrid mass flux vectors were recently studied by Foster and Miller [27, 28], who found that subgrid mass flux vectors can be important in reacting flows (see below).

The subgrid heat flux vector has been considered in: (1) natural convection dominated turbulent thermal flows [102, 93, 41], (2) forced convection dominated turbulent thermal flows [96, 64, 21] and (3) atmospheric turbulent boundary layers [76, 75, 11]. However, little literature addresses the subgrid heat flux vector in either supercritical reacting or non-reacting flows. Exceptions include Selle *et al.* [81] and Borghesi and Bellan [7] who provide *a priori* and *a posteriori* analyses of the subgrid heat flux vector for binary mixing. They pointed out in oxygen/hydrogen mixing that the gradient of the subgrid heat flux is of the same order of magnitude as the leading order terms in the filtered energy equation. The model introduced in Ref. [81] for the subgrid heat flux vector was further investigated in Refs. [88, 89] by Taskinoglu and Bellan. However, these studies have been limited to non-reacting mixing layers.

In a related matter, Foster and Miller [27, 28] have conducted *a priori* analyses of DNS data of high pressure turbulent combustion to examine the importance of the subgrid mass flux vectors. They argue that for reacting flows a more detailed examination of unclosed subgrid terms is needed than purely global statistics. This is because turbulent flame dynamics can be strongly influenced by localized phenomena, including extinction and reignition. Therefore, in addition to a global analysis, they have also considered conditioning statistics on localized regions of the stoichiometric region, regions of large filtered subgrid scalar dissipation, large temperature subgrid variance, large reaction rate, and large scalar subgrid variance. They show that even though the subgrid mass flux vector's contribution is relatively small when analyzed globally, it is much more important for regions of large subgrid scalar dissipation and large subgrid temperature variance. Furthermore, the divergence of the subgrid mass flux vectors is of the same order, or larger, than the divergence of the filtered mass flux vectors in these regions. Foster and Miller [25] have also pointed out that with increasing Reynolds number, and filter widths, the contribution of the subgrid mass flux vector increases.

1.2 Objectives

Based on the above, the primary objectives of this chapter are to: I- conduct an *a priori* analysis of the subgrid heat flux vector, both in mixing and reacting flows, based on the DNS data generated in Refs. [27, 28, 25, 24], and II- test the hypothesis that the subgrid heat flux vector may require modeling in LES of realistic, high pressure, variable density, multicomponent, turbulent flames.

1.3 Governing Equations

The following sections in this chapter provide a post processing analysis of a previously generated DNS database of high pressure H_2/O_2 and H_2/Air non-premixed shear flames. The DNS solves the fully compressible form of the continuity, momentum, total energy, and all species' partial density equations in a temporarily developing reacting shear layer geometry (Fig. 2.1). The Peng-Robinson real gas state equation, real property models, and generalized heat and mass diffusion are also incorporated. The chemical reaction is calculated by a detailed pressure dependent 19-step and 8-species mechanism [85] for the H_2/O_2 flame. For the H_2/Air simulations either a 4-step 3-species nitrogen mechanism is added [85]. The details are provided in Refs. [27, 28, 25].

Equally spaced grid points from $0 \leq x_1 \leq L_1$ and $0 \leq x_3 \leq L_3$ in x_1 and x_3 directions are used for the computational mesh. In the x_2 direction an analytical mapping function proposed in [36] is employed to stretch the mesh in the cross-stream direction. In the vorticity thickness region a fine grid spacing ($\Delta x_2 \approx \Delta x_1$) is used, while the spacing stretches towards each of the free stream boundaries where $\Delta x_2 \approx 5\Delta x_1$ [23]. Assigning a coarser mesh in the free stream regions reduces the computational time significantly. Detail of the mapping the can be found in [23].

An eight order central explicit finite difference method and a forth order Runge-Kutta are employed to solve for the spatial and time derivatives, respectively. At each Runge-Kutta stage tenth order filtering is also applied to control spurious oscillations. The message passing interface (MPI) routines are used to parallize the code in all three directions. Further information about the numerical algorithms can be found in Ref. [38].

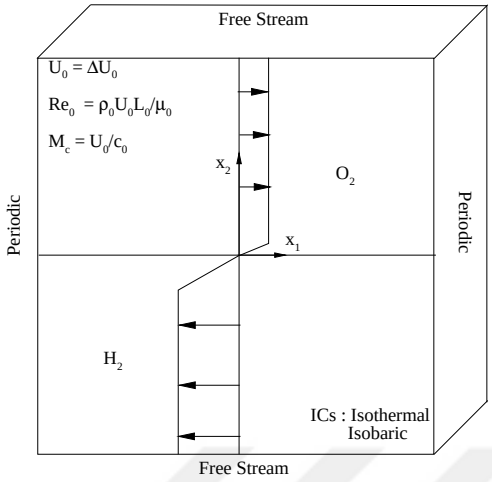


Figure 1.1: Direct Numerical Simulation domain schematic

The current work only provides the summarized forms of the governing equations. For a more detailed formulation see: Palle [65], Palle and Miller [66], Vasudevan [91] and Foster [23]. The compressible form of the Navier-Stokes, energy, and species transport equations are:

$$\frac{\partial \rho}{\partial t} + \frac{\partial}{\partial x_j}[\rho u_j] = 0, \tag{1.1}$$

$$\frac{\partial}{\partial t}(\rho u_i) + \frac{\partial}{\partial x_j}[\rho u_i u_j + P\delta_{ij} - \tau_{ij}] = 0, \tag{1.2}$$

$$\frac{\partial}{\partial t}(\rho e_t) + \frac{\partial}{\partial x_j}[(\rho e_t + P)u_j - u_i\tau_{ij} + Q_j + \sum_{\alpha=1}^{N} H'_\alpha J'_{j,\alpha}] = S_e, \tag{1.3}$$

$$\frac{\partial}{\partial t}(\rho Y_\alpha) + \frac{\partial}{\partial x_j}[\rho Y_\alpha u_j + J'_{j,\alpha}] = S_{Y_\alpha}, \tag{1.4}$$

where t is time, x_j is the spatial coordinate vector, ρ is the mixture density, u_j is the mixture velocity, P is the pressure, δ_{ij} is the Kronecker delta tensor, τ_{ij} is the (Newtonian) viscous stress tensor, e_t the total specific energy (internal plus kinetic), Q_j is the Bearman-Kirkwood form of the heat flux vector, $\sum_{\alpha=1}^{N} H'_\alpha J'_{j,\alpha}$ is the enthalpy flux (N is the total number of species) in which the partial molar enthalpy

for species α is $H'_\alpha = \partial H' / \partial X_\alpha$ (X_α is the mole fraction of species α), and the molar mass flux vector for species α is $J_{j,\alpha}$. The relation $J'_{j,\alpha} = M_\alpha J'_{j,\alpha}$ (M_α stands for the molecular weight of species α) converts the molar flux vector to the mass flux vector, S_e is the chemical reaction source term for the energy equation ($S_e = -\sum_{\alpha=1}^{N} \dot{\omega_\alpha} \Delta H^0_\alpha$), where $\dot{\omega_\alpha}$ is the reaction rate for species α and ΔH^0_α is the enthalpy of formation. For Eq. (2.4), Y_α represents the mass fraction of species α, and $S_{Y,\alpha}$ is the chemical reaction source term for species α.

In order to capture real gas effects, the Peng-Robinson equation of state is used:

$$P = \frac{RT}{V' - B_m} - \frac{A_m}{V'^2 + 2V'B_m - B_m^2}, \tag{1.5}$$

where V' is the specific molar volume, R is the universal gas constant, and the temperature is T. The mixture parameters A_m and B_m are calculated by non-linear mixing rules found in Refs. [34, 57].

The effects of multicomponent, differential, and cross diffusion effects have been included into the equations employed for the DNS calculations. Under high pressures, these effects have the ability to be significant [65, 33, 32, 58, 26]. Harstad and Bellan derived the full form of the heat and mass flux vectors taking into account the aforementioned effects by using non-equilibrium thermodynamics and fluctuation theory (as kinetic theory is not applicable for high pressure dense fluids). The heat flux vector may be represented as a superposition of terms proportional to temperature, pressure, and mole fraction gradients:

$$Q_j = Q_j^T + Q_j^{X_1} + Q_j^{X_2} + ... + Q_j^{X_{\alpha=N-1}}, \tag{1.6}$$

The superscripts indicate the variable gradient upon which the term is proportional to. The expanded heat flux form adopted in the DNS is derived from non-equilibrium thermodynamics and fluctuation theory:

$$
\begin{aligned}
Q_j = &-\left\{\kappa + \sum_{\beta=1}^{N-1}\sum_{l>\beta}^{N} X_\beta X_\gamma \alpha_{BK}^{\beta\gamma}\alpha_{BK}^{\beta\gamma}\frac{R\rho}{M_m}D_m^{\beta\gamma}\right\}\frac{\partial T}{\partial x_j} \\
&-\sum_{\beta=1}^{N}\left\{X_\beta\sum_{\gamma\neq\beta}^{N}\left[\frac{M_\gamma}{M_m^2}X_\gamma\alpha_{BK}^{\beta\gamma}\rho D_m^{\beta\gamma}\right]V_{,\beta}\right\}\frac{\partial P}{\partial x_j} \\
&-\sum_{\eta=1}^{N-1}\sum_{\beta=1}^{N}\left\{RT\sum_{\gamma\neq\beta}^{N}\left[\frac{M_\gamma}{M_m^2}X_\gamma\alpha_{BK}^{\beta\gamma}\rho D_m^{\beta\gamma}\right]\alpha_D^{\beta\eta}\right\}\frac{\partial X_\eta}{\partial x_j},
\end{aligned}
\tag{1.7}
$$

where N is the number of species, $M_m = \sum_{\alpha=1}^{N} X_\alpha M_\alpha$ is the mixture molecular weight and X_α and M_α are the mole fraction and molecular weight of species α, respectively. In the above, $D_m^{\beta\gamma}$ represents the binary mass diffusivities, κ is the mixture thermal conductivity, and the thermal and mass diffusion factors are represented by $\alpha_{BK}^{\beta\gamma}$ and $\alpha_D^{\beta\gamma}$, respectively. The first term represents the expanded Fourier component. The remaining terms are referred to as Dufour diffusion and represent heat flux due to both mole fraction and pressure gradients.

$$
\begin{aligned}
\overline{J}_j^\beta = &-nD_m^{\beta\gamma}\sum_{\gamma\neq\beta}^{N}\left\{X_\beta X_\gamma\frac{M_\beta}{M_m}\alpha_{BK}^{\beta\gamma}\right\}\frac{\partial lnT}{\partial x_j} \\
&-\sum_{\gamma\neq\beta}^{N}\frac{nD_m^{\beta\gamma}}{RT}\left\{-\frac{M_\beta M_\gamma}{M_m M_m}X_\beta X_\gamma V'_{,\gamma}+\frac{M_\gamma M_\gamma}{M_m M_m}X_\beta X_\gamma V'_{,\beta}\right\}\frac{\partial P}{\partial x_j} \\
&-\sum_{\eta=1}^{N-1}\left\{\sum_{\gamma\neq\beta}^{N}\left[\frac{M_\beta M_\gamma}{M_m M_m}X_\beta nD_m^{\beta\gamma}\alpha_D^{\gamma\eta}+\frac{M_l\gamma M_\gamma}{M_m M_m}X_\gamma nD_m^{\gamma\beta}\alpha_D^{\beta\eta}\right]\right\}\frac{\partial X_\eta}{\partial x_j},
\end{aligned}
\tag{1.8}
$$

where n is the molar density ($n = \rho/M_m$), and $V'_{,\beta}$ is the partial molar volume of species.

The simulations were conducted on the Palmetto Cluster at Clemson University with resolutions up to $560\times720\times336 \approx 135$ million grid points and using as many as 2016 processing cores ($Re_0 = 2500$). The initial vorticity thickness, δ_0, is defined as the initial transition length from one free stream to the other. The “flame Reynolds number" is defined by $Re_F = U_0\delta_0\rho_0/\mu_0$; where U_0 is the velocity difference between the two streams, ρ_0 is the averaged density, and μ_0 is the averaged viscosity from

each stream value. For the current work, 4 cases are considered as summarized in Table 2.1; including one H_2/O_2 purely mixing case, three H_2/O_2 reacting cases with different Reynolds numbers (Re_0 = 850, 2500) all at an ambient pressure $P_0 = 100atm$, and one H_2/Air reacting case with a different initial pressures (P_0 = 35 atm) and Reynolds number (Re_0 = 2500). Compared with the H_2/O_2 flame, the H_2/Air flame is significantly diluted by N_2 which results in lower flame temperature and extensive local extinction; especially across the stoichiometric mixture fraction ($\phi \approx 0.1$) region. The mixture fraction, ϕ, is defined as ;

$$\phi = \frac{sY^{H_2} - Y^{O_2} + Y_0^{O_2}}{sY_0^{H_2} + Y_0^{O_2}}, \tag{1.9}$$

where $0 \leq \phi \leq 1$, s is the stoichiometric constant, Y^{H_2} and Y^{O_2} are the local mass fraction for H_2 and O_2, respectively, and $Y_0^{H_2}$ and $Y_0^{O_2}$ are the corresponding free stream values. In the pure fuel region $\phi = 1$, and in the pure oxidizer region $\phi = 0$. Intermediate values indicate varying degrees of mixedness. The mixture fraction and its dissipation are important quantities in many turbulent combustion models. The reason for considering each of these regions seperately is that flame dynamics such as ignition, extinction and reignition are known to be highly localized. Therefore, if a model were deemed to perform well when only globally averaged it may not necessarily perform well locally in important flame regions.

Run	Oxidizer	$P_0(atm)$	Type	$T_0(K)$	Re_0	$Re_\delta(t_f)$	$N_1 \times N_2 \times N_3$	t_f^*
1	Oxygen	100	Mixing	700	2000	15000	$384 \times 384 \times 232$	80
2	Oxygen	100	Reacting	700	850	4500	$384 \times 384 \times 232$	80
3	Oxygen	100	Reacting	700	2500	16000	$560 \times 720 \times 336$	115
4	Air	35	Reacting	700	2500	18000	$532 \times 630 \times 340$	148

Table 1.1: Summary of simulation parameters from all cases considered. P_0 is initial pressure, T_0 is the initial temperature, Re_0 the initial Reynolds number, $Re_\delta(t_f)$ the Reynolds number calculated based on the vorticity thickness at the final simulation time, N_2, N_2, N_3 are the number of grid points in the x_1, x_2, x_3 direction respectively, and t_f^* is non-dimensionlized final simulation time.

1.4 Subgrid Analysis

A subgrid analysis relevant to LES is next performed. In LES a general filtered variable, $\overline{\Phi}$, is defined by the convolution integral:

$$\overline{\Phi}(x) = \int_{\Omega} G(x_j - x'_j)\Phi(x'_j)dx'_j, \tag{1.10}$$

where $G(x_j)$ is the filter kernel defined over the domain Ω. As compressible flow is considered for this work, employing the Favre filtering concept is necessary. The Favre filter is a density-weighted filtering operation, and is equivalent to a standard filter for constant density flows.

The subgrid analysis is done in both a 'global' flame manner (i.e. conditioned on $0.01 \leq \phi \leq 0.99$) as well as by conditioning on various specific regions within each flame. The reason for considering each of these localized regions listed in Table 2.2 separately is that flame dynamics such as ignition, extinction and re-ignition are known to be highly localized. Therefore, if a model were deemed to perform well when only globally averaged it may not necessarily perform well locally in important flame regions. Local regions are therefore analyzed by conditionally filtering on subsets of the global flame defined in Table 2.2, where $E(\Phi)$ indicates the expected value (average) over the global flame region ($0.01 \leq \phi \leq 0.99$).

The current work uses a spherical top-hat filter with different diameters (Δ) listed in Table 2.3. The filter diameter $3\delta_{\omega 0}$ provides a realistic LES grid resolution as listed in Table. 2.3. For example, with $\Delta = 3\delta_{\omega 0}$, the $H_2/O_2, Re_0 = 2500$ reacting case will have grid resolution as $62 \times 80 \times 37$ in LES (with $\Delta x_{1,LES} = \Delta/2$) Therefore, most results herein are for a filter diameter of $3\delta_{\omega 0}$. However, the temporally developing shear layer can be seen as a small portion of a real combustion chamber. Larger filter diameters can be interpreted as relevant to simulations of larger domains. Figure 4 of Ref. [27] provides various spectra from the H_2/O_2 case at $Re_0 = 2500$ together with the relative filtering wavenumber (the middle of the three corresponding to $\Delta = 3\delta_{\omega 0}$). Note that the H_2/O_2 and H_2/Air

The global region	$0.01 \leq \phi \leq 0.99$
The stoichiometric condition of H_2/O_2 flame	$0.1 \leq \phi \leq 0.2$
The stoichiometric condition of H_2/Air flame	$0.01 \leq \phi \leq 0.05$
Large filtered temperature variance	$\langle\langle T''^2\rangle\rangle / E(\langle\langle T''^2\rangle\rangle) \geq 2$
Large subgrid kinetic energy	$\overline{k_{sgs}} / E(\overline{k_{sgs}}) \geq 2$
Large filtered mixture fraction variance	$\langle\langle \phi''^2\rangle\rangle / E(\langle\langle \phi''^2\rangle\rangle) \geq 2$
High OH reaction rate regions	$\overset{\bullet}{\omega}^{OH} / E(\overset{\bullet}{\omega}^{OH} \geq 2)$
High filtered scalar dissipation	$\overline{\chi^{\phi}} / E(\overline{\chi^{\phi}}) \geq 2$
Elevated temperature regions	$T/T_0 \geq 2$

Table 1.2: The local regions within which statistical analyses have been done.

flames behave quite differently. The former's chemical reaction is near equilibrium whereas the latter displays large levels of local extinction. The diluted levels of oxygen in the H_2/Air flame lead to much smaller flame temperatures in comparison the H_2/O_2 flames. See Refs. [27, 28, 25]. for details.

The exact (unclosed) filtered LES governing equations can be expressed as follows:

$$\frac{\partial \overline{\rho}}{\partial t} + \frac{\partial}{\partial x_j}[\, \overline{\rho}\, \langle\langle u_j \rangle\rangle] = 0, \tag{1.11}$$

$$\frac{\partial}{\partial t}(\overline{\rho}\, \langle\langle u_i \rangle\rangle) + \frac{\partial}{\partial x_j}[\, \overline{\rho}\, \langle\langle u_i u_j \rangle\rangle + \overline{P}\delta_{ij} - \overline{\tau_{ij}}\,] = 0, \tag{1.12}$$

$$\frac{\partial}{\partial t}\, (\overline{\rho}\, \langle\langle e_t \rangle\rangle) + \frac{\partial}{\partial x_j}\left[(\overline{\rho}\, \langle\langle e_t \rangle\rangle) u_j + \overline{P u_j}\, - \overline{u_i \tau_{ij}} + \overline{Q_j} + \overline{\sum_{\alpha=1}^{N} H'_\alpha J'_{j,\alpha}} \right] = \overline{S_e}, \tag{1.13}$$

$$\frac{\partial}{\partial t}(\, \overline{\rho}\, \langle\langle Y_\alpha \rangle\rangle) + \frac{\partial}{\partial x_j}[\, \overline{\rho}\, \langle\langle Y_\alpha u_j \rangle\rangle + \langle\langle J'_{j,\alpha} \rangle\rangle] = \overline{S_{Y_\alpha}}. \tag{1.14}$$

$$\overline{P} = \overline{\frac{RT}{V' - B_m} - \frac{A_m}{V'^2 + 2V'B_m - B_m^2}}, \tag{1.15}$$

The set of LES primitive variables is $\overline{\Psi} = \overline{\rho}, \langle\langle u_j \rangle\rangle, \langle\langle e_t \rangle\rangle, \langle\langle Y_\alpha \rangle\rangle$. Any term which cannot be directly obtained from this set of variables is unclosed and therefore requires modeling. For example, the

non-linear convective term in Eq. 2.12 is typically decomposed as:

$$\langle\langle u_i u_j \rangle\rangle = \langle\langle u_i \rangle\rangle \langle\langle u_j \rangle\rangle + \tau_{sgs,ij} \tag{1.16}$$

where $\tau_{sgs,ij} = \left[\langle\langle u_i u_j \rangle\rangle - \langle\langle u_i \rangle\rangle \langle\langle u_j \rangle\rangle\right]$ and is referred to as the subgrid stress tensor.

As DNS contains all the information about any instantaneous variable, the 'exact' subgrid information may be accessed by filtering the DNS data. This is referred to as the *a priori* approach to LES analysis (in contrast to the *a posteriori* approach in which an actual LES is performed).

Even though many unclosed terms exist in the LES filtered equations, this work focuses on the heat flux vector, Eq. (2.7). A detailed analysis and modeling for a canonical high pressure H_2/O_2 reacting shear layer is performed. The magnitude of the exact filtered heat flux, $|\overline{Q_j(\Psi)}|$, is compared with the magnitude of heat flux vector calculated using only filtered primitive variables, $|Q_j(\overline{\Psi})|$. Here, Ψ represents the set of primitive variables used in the DNS, $\Psi = \left[\rho, u_j, e_t, Y_\alpha\right]$. Other variables such as temperature and pressure are obtained from this base set; eg. $T(\Psi)$ and $P(\Psi)$. Similarly, Eq. (2.7) provides the heat flux vector, $Q_j(\Psi)$. For LES, variables other than the set $\overline{\Psi}$ can only be approximated as functions of $\overline{\Psi}$; eg. $T(\overline{\Psi})$, $P(\overline{\Psi})$, and $Q_j(\overline{\Psi})$. Therefore, terms calculated in such a manner are not necessarily either equal to, nor even approximately equal to, the terms in the exact LES equations. For example, $\overline{P(\Psi)}$ appears in the exact LES momentum equation. However, only $P(\overline{\Psi})$ can be calculated. The difference, therefore, defines an unclosed 'subgrid, or 'subgrid scale (SGS) pressure; $\overline{P(\Psi)} = P(\overline{\Psi}) + P_{sgs}$. Subgird terms such as this may, or may not, require modeling depending in part on their magnitude with respect to both the resolved term [eg. $P(\overline{\Psi})$] as well as with respect to other terms in the LES equations.

The subject of the current work is in testing whether or not the subgrid heat flux vector defined by $Q_{sgs,j} = \overline{Q_j(\Psi)} - Q_j(\overline{\Psi})$ is significant for reacting flows. *A priori* testing using the DNS data is chosen as all forms of the heat flux and subgrid heat flux vectors can be calculated 'exactly'. The 'exact' filtered heat flux vector, which cannot be calculated within an actual LES, is expressed as follows:

Run	Δx_1	$\Delta_1 = 3\delta_{\omega 0}$	$\Delta_2 = 4\delta_{\omega 0}$	$\Delta_2 = 5\delta_{\omega 0}$	$(N_1 \times N_2 \times N_3)_{LES}$
1	$0.12\delta_{\omega 0}$	$25\Delta x_1$	$33\Delta x_1$	$42\Delta x_1$	$31 \times 31 \times 19$
2	$0.12\delta_{\omega 0}$	$25\Delta x_1$	$33\Delta x_1$	$42\Delta x_1$	$31 \times 31 \times 19$
3	$0.16\delta_{\omega 0}$	$19\Delta x_1$	$25\Delta x_1$	$32\Delta x_1$	$59 \times 76 \times 35$
4	$0.17\delta_{\omega 0}$	$18\Delta x_1$	$24\Delta x_1$	$30\Delta x_1$	$62 \times 80 \times 37$

Table 1.3: Filtering diameter size used to postprocess the DNS data. 'Run' corresponds to the DNS cases presented in Table 2.1, $\Delta_1 = 3\delta_{\omega 0}$ is the spherical filter diameter this work focuses on, Δx_1 is the DNS grid spacing in the x_1 direction, $\delta_{\omega 0}$ is the DNS initial vorticity thickness, $(N_1 \times N_2 \times N_3)_{LES}$ are the equivalent LES grid resolutions in x_1, x_2, and x_3 directions, respectively, for, $\Delta_1 = 3\delta_{\omega 0}$.

$$\begin{aligned}\overline{Q_j(\Psi)} = &\overline{-\left\{\kappa + \sum_{\beta=1}^{N-1}\sum_{l>\beta}^{N} X_\beta X_\gamma \alpha_{BK}^{\beta\gamma}\alpha_{BK}^{\beta\gamma}\frac{R\rho}{M_m}D_m^{\beta\gamma}\right\}\frac{\partial T}{\partial x_j}} \\ &\overline{-\sum_{\beta=1}^{N}\left\{X_\beta \sum_{\gamma\neq\beta}^{N}\left[\frac{M_\gamma}{M_m^2}X_\gamma \alpha_{BK}^{\beta\gamma}\rho D_m^{\beta\gamma}\right]V_{,\beta}\right\}\frac{\partial P}{\partial x_j}} \\ &\overline{-\sum_{\eta=1}^{N-1}\sum_{\beta=1}^{N}\left\{RT\sum_{\gamma\neq\beta}^{N}\left[\frac{M_\gamma}{M_m^2}X_\gamma \alpha_{BK}^{\beta\gamma}\rho D_m^{\beta\gamma}\right]\alpha_D^{\beta\eta}\right\}\frac{\partial X_\eta}{\partial x_j}},\end{aligned} \tag{1.17}$$

In contrast, the 'resolved heat flux vector that can be calculated within an LES is:

$$\begin{aligned}Q_j(\overline{\Psi}) = &-\left\{\kappa(\overline{\Psi}) + \sum_{\beta=1}^{N-1}\sum_{l>\beta}^{N} X_\beta(\overline{\Psi}) X_\gamma(\overline{\Psi})\alpha_{BK}^{\beta\gamma}(\overline{\Psi})\alpha_{BK}^{\beta\gamma}(\overline{\Psi})\frac{R\bar{\rho}}{M_m}D_m^{\beta\gamma}(\overline{\Psi})\right\}\frac{\partial T(\overline{\Psi})}{\partial x_j} \\ &-\sum_{\beta=1}^{N}\left\{X_\beta(\overline{\Psi})\sum_{\gamma\neq\beta}^{N}\left[\frac{M_\gamma}{M_m^2}X_\gamma(\overline{\Psi})\alpha_{BK}^{\beta\gamma}(\overline{\Psi})\bar{\rho}D_m^{\beta\gamma}(\overline{\Psi})\right]V_{,\beta}(\overline{\Psi})\right\}\frac{\partial P(\overline{\Psi})}{\partial x_j} \\ &-\sum_{\eta=1}^{N-1}\sum_{\beta=1}^{N}\left\{RT(\overline{\Psi})\sum_{\gamma\neq\beta}^{N}\left[\frac{M_\gamma}{M_m^2}X_\gamma(\overline{\Psi})\alpha_{BK}^{\beta\gamma}(\overline{\Psi})\bar{\rho}D_m^{\beta\gamma}(\overline{\Psi})\right]\alpha_D^{\beta\eta}(\overline{\Psi})\right\}\frac{\partial X_\eta(\overline{\Psi})}{\partial x_j},\end{aligned} \tag{1.18}$$

,

where all the terms dependent on the variable set $\overline{\Psi}$ and can be calculated in an LES simulation. The

difference between Eqs. (2.17)-(2.18) gives the subgrid heat flux vector which might require modeling and is the focus of the current work. The subgrid analysis aims to analyze the possible necessity of modeling the subgrid heat flux vector by calculating the correlation coefficients and ratio distributions of $|\overline{Q_j(\Psi)}|$ to $|Q_j(\overline{\Psi})|$. Ratios relative to other subgrid terms in the filtered energy equation [Eq. (2.13)] are also considered. Note that there are a number of ways in which to interpret the proper caclulation of $Q_j(\overline{\Psi})$ within an actual LES. Equation (2.18) above can certainly be used directly. To be able to neglect the subgrid heat flux vector, the condition of $\overline{Q_j(\Psi)} \approx Q_j(\overline{\Psi})$ should at least be satisfied.

1.4.1 Subgrid Heat Flux Vector Analysis

The subgrid heat flux vector has been neglected in nearly all previous LES studies. No validation or testing of this assumption exits for reacting flows. The subgrid hear flux vector is defined by $Q_{sgs,j} = \overline{Q_j(\Psi)} - Q_j(\overline{\Psi})$, where the filtered heat flux, $\overline{Q_j(\Psi)}$, is calculated by directly filtering Eq. (2.7), and the resolved heat flux vector, $Q_j(\overline{\Psi})$, is calculated using the resolved primitive variables. The subject of this part of the current work is to analyze the subgrid heat flux vector. Four cases are focused on, including the H_2/Air reacting case with $Re_0 = 2500$, the H_2/O_2 purely mixing case with $Re_0 = 2000$, and the H_2/O_2 reacting cases with $Re_0 = 850$ and $Re_0 = 2500$ respectively. All results below use the filter diameter of $\Delta/\delta_{\omega 0} = 3$.

To compare the filtered heat flux vector to the resolved heat flux vector, Figure 2.2 presents PDFs of the ratio of $|\overline{Q_j(\Psi)}|$ to $|Q_j(\overline{\Psi})|$. The PDFs have a Gaussian like shape, with peaks located at $|\overline{Q_j(\Psi)}|/|Q_j(\overline{\Psi})| \approx 1$, indicating the resolved heat flux vector has similar magnitude as the filtered heat flux vector. Also note that the filtered pressure can be either significantly larger than, or smaller than, the resolved heat flux. Compared with the reacting cases, the resolved heat flux behaves differently in the purely mixing case, as these PDFs display a wider distribution of ratios. In addition, the resolved heat flux vector deviates more from the filtered heat flux vector in specific local regions; *e.g.*, the resolved heat flux vector magnitude can be as small as half of the filtered heat flux vector magnitude, or as large as twice the filtered heat flux vector magnitude, in the stoichiometric mixture

fraction region [Fig. 2.2(b)] and regions of large OH reaction rate [Fig. 2.2(c)]. Relatively little influence of the Reynolds number is observed although significantly different behavior is observed for the H_2/Air flame in comparison to the H_2/O_2 flames; presumably due to the high levels of extinction in the former. Note that only the reacting cases are shown in [Fig. 2.2(c)] since there is no OH reaction rate to condition on for the mixing case. Figure 2.3 further illustrates the difference between the filtered heat flux and the resolved heat flux by presenting PDFs of the ratio of $|\partial\overline{Q_j(\Psi)}/\partial x_j|/|\partial Q_j(\overline{\Psi})/\partial x_j|$ (the divergence being the actual term in the energy equation). As differentiation enhances small scale features, these PDFs have a much wider distribution compared with those in Fig. 2.2.

Based on the above results, there is significant difference between the filtered heat flux and the resolved heat flux. The influence of the subgrid heat flux (*i.e.* $Q_{sgs,j} = \overline{Q_j(\Psi)} - Q_j(\overline{\Psi})$) is next compared with that of other subgrid terms in the filtered energy equation. First, the subgrid heat flux is compared with the subgrid convective term, $(\rho e_t u_j)_{sgs}$. Figure 2.4 presents PDFs of the ratio of $|Q_{sgs,j}|/|(\rho e_t u_j)_{sgs}|$. In the global flame region [Fig. 2.4(a)] and regions of large OH reaction rate [Fig. 2.4(c)], the subgrid heat flux magnitude is typically 5% of the subgrid convective energy. However, this value can be up to as large as 25%. The subgrid heat flux vector is relatively larger in the stoichiometric surface [Fig. 2.4(b)] where it can exceed the magnitude of $(\rho e_t u_j)_{sgs}$ in the H_2/O_2 $Re_0 = 850$ flame. However, in general, the relative influence of the subgrid heat flux is significantly diminishing with respect to that of the subgrid convective term with increasing Reynolds number. A similar analysis and conclusions are drawn from Fig. 2.5 which shows PDFs of $|\partial Q_{sgs_j}/\partial x_j|/|\partial(\rho e_t u_j)_{sgs}/\partial x_j|$.

Finally, Figs. 2.6 and 2.7 provide a similar analysis of the relative effects of the subgrid heat flux in comparison to the subgrid pressure work term and its gradient, respectively. The subgrid heat flux is found to be more significant relative to these terms than to the subgrid convective terms. Again, for mixing cases the ratios are generally small. However, for reacting cases the subgrid heat flux is as important and generally larger than the corresponding pressure work terms. Nevertheless, as before, the trend is decreasing importance with increasing Reynolds number. This suggets that neglecting the subgrid heat flux in LES of high Reynolds number reacting flows is most likely reasonable.

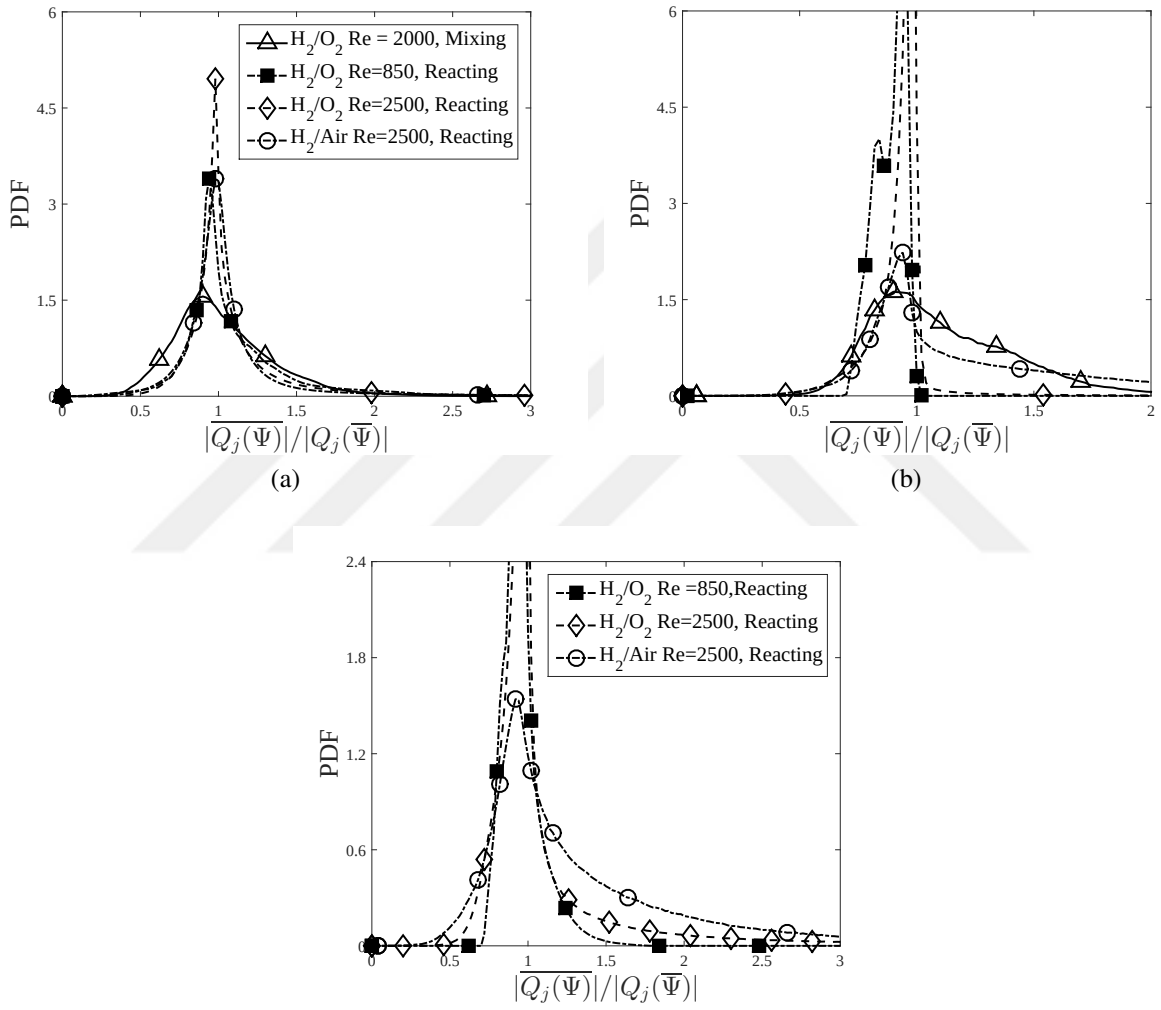


Figure 1.2: PDFs of $|\overline{Q_j(\Psi)}|/|Q_j(\overline{\Psi})|$, conditioned on: (a) $0.01 \leq \phi \leq 0.99$, (b) the stoichiometric surface, (c) $\dot{\omega}^{OH} / E(\dot{\omega}^{OH} \geq 2)$.

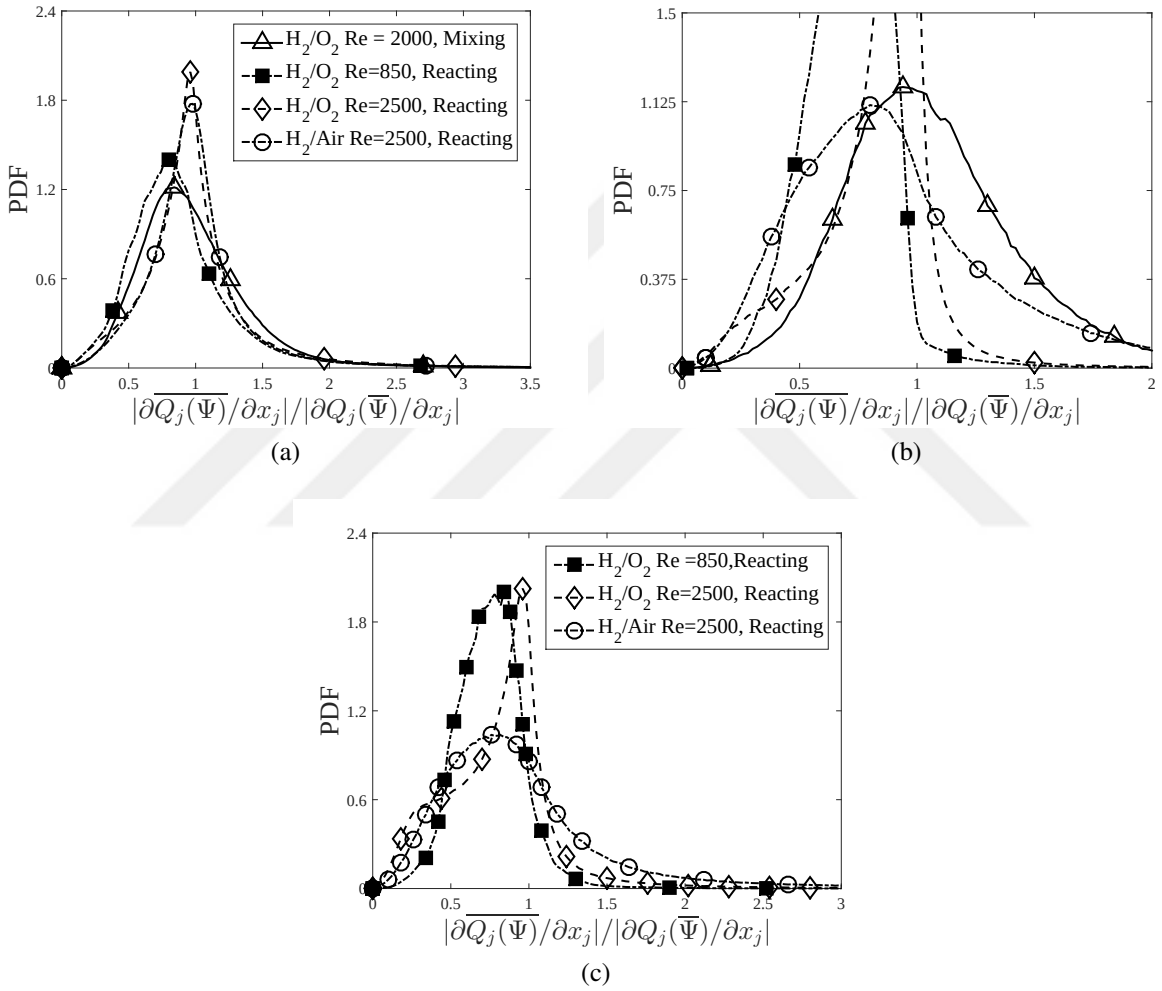


Figure 1.3: PDFs of $|\partial\overline{Q_j(\Psi)}/\partial x_j|/|\partial Q_j(\overline{\Psi})/\partial x_j|$, conditioned on: (a) $0.01 \leq \phi \leq 0.99$, (b) the stoichiometric surface, (c) $\dot{\omega}^{OH}/E(\dot{\omega}^{OH} \geq 2)$.

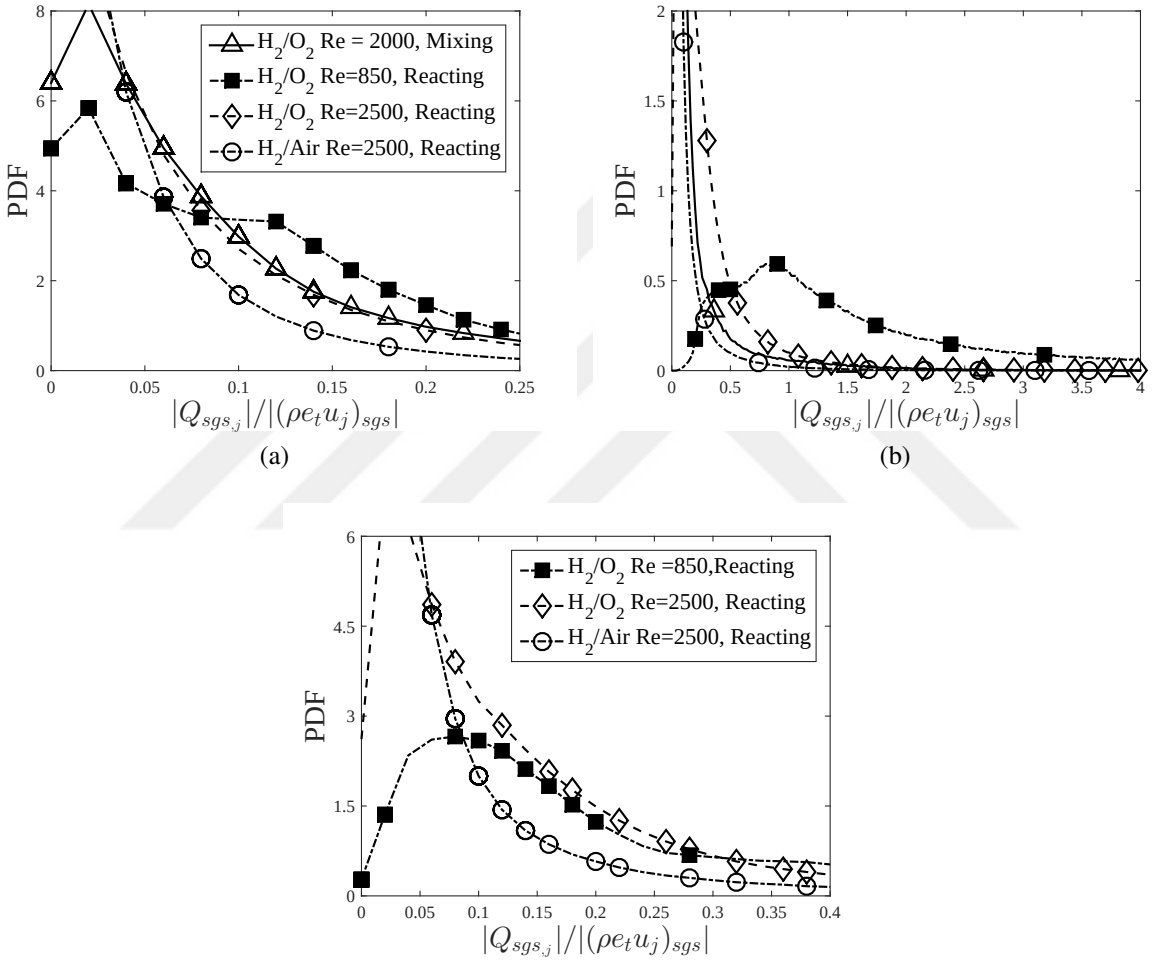


Figure 1.4: PDFs of $|Q_{sgs_j}|/|(\rho e_t u_j)_{sgs}|$, conditioned on: (a) $0.01 \leq \phi \leq 0.99$, (b) the stoichiometric surface, and (c) $\dot{\omega}^{OH} / E(\dot{\omega}^{OH} \geq 2)$.

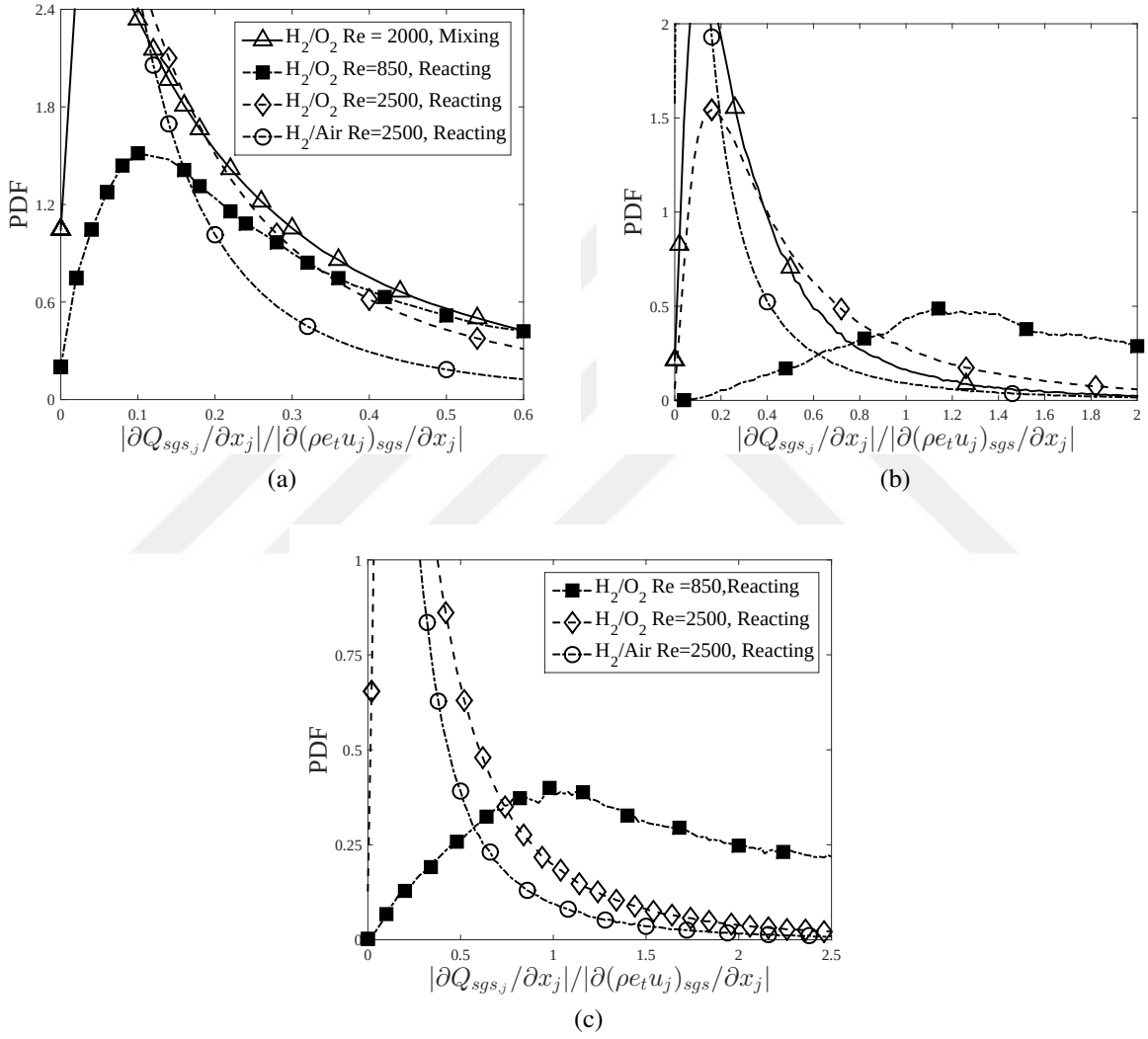


Figure 1.5: PDFs of $|\partial Q_{sgs_j}/\partial x_j|/|\partial(\rho e_t u_j)_{sgs}/\partial x_j|$, conditioned on: (a) $0.01 \leq \phi \leq 0.99$, (b) the stoichiometir surface, and (c) $\dot{\omega}^{OH}/E(\dot{\omega}^{OH} \geq 2)$.

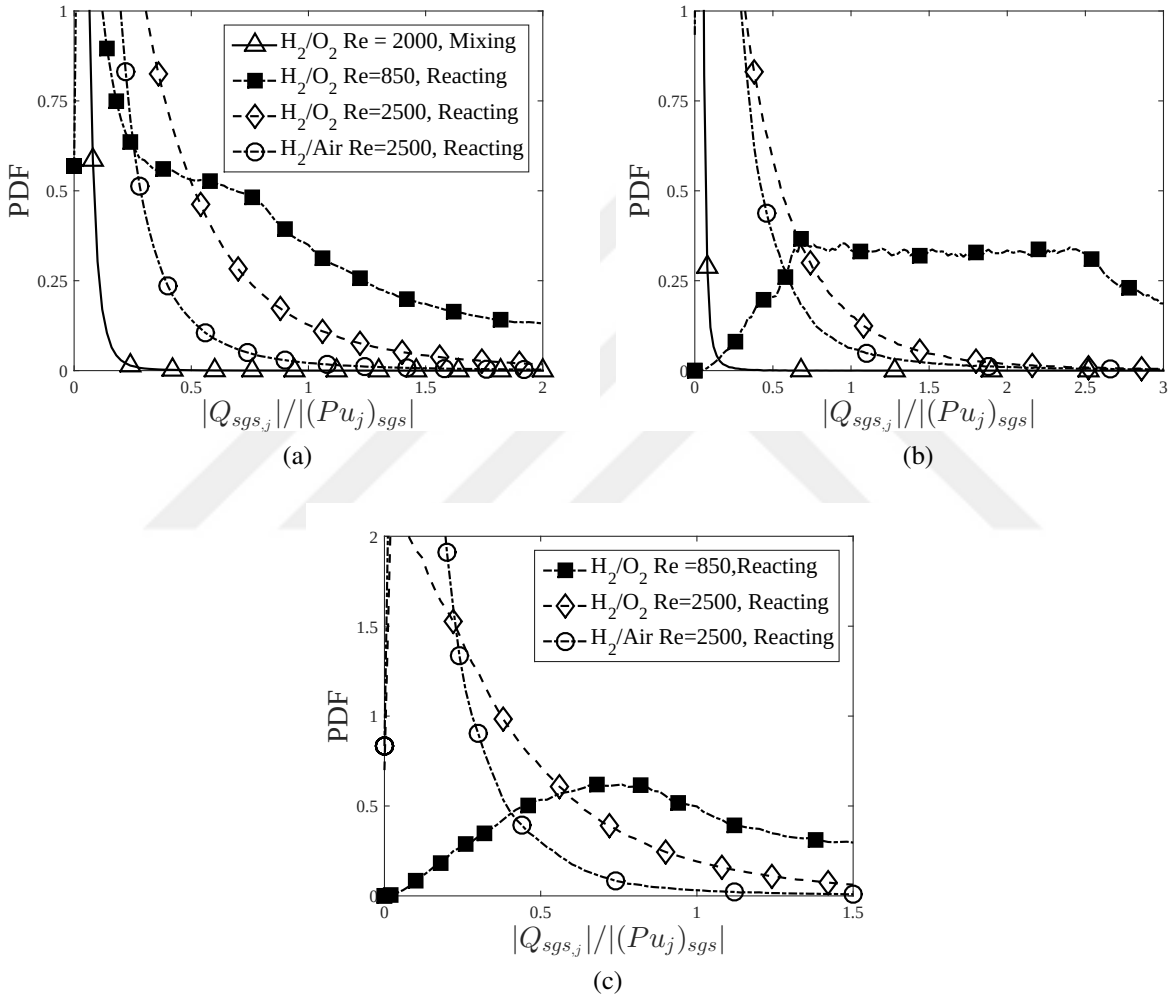


Figure 1.6: PDFs of $|Q_{sgs_j}|/|(Pu_j)_{sgs}|$, conditioned on: (a) $0.01 \leq \phi \leq 0.99$, (b) the stoichiometric surface, and (c) $\dot{\omega}^{OH}/E(\dot{\omega}^{OH} \geq 2)$.

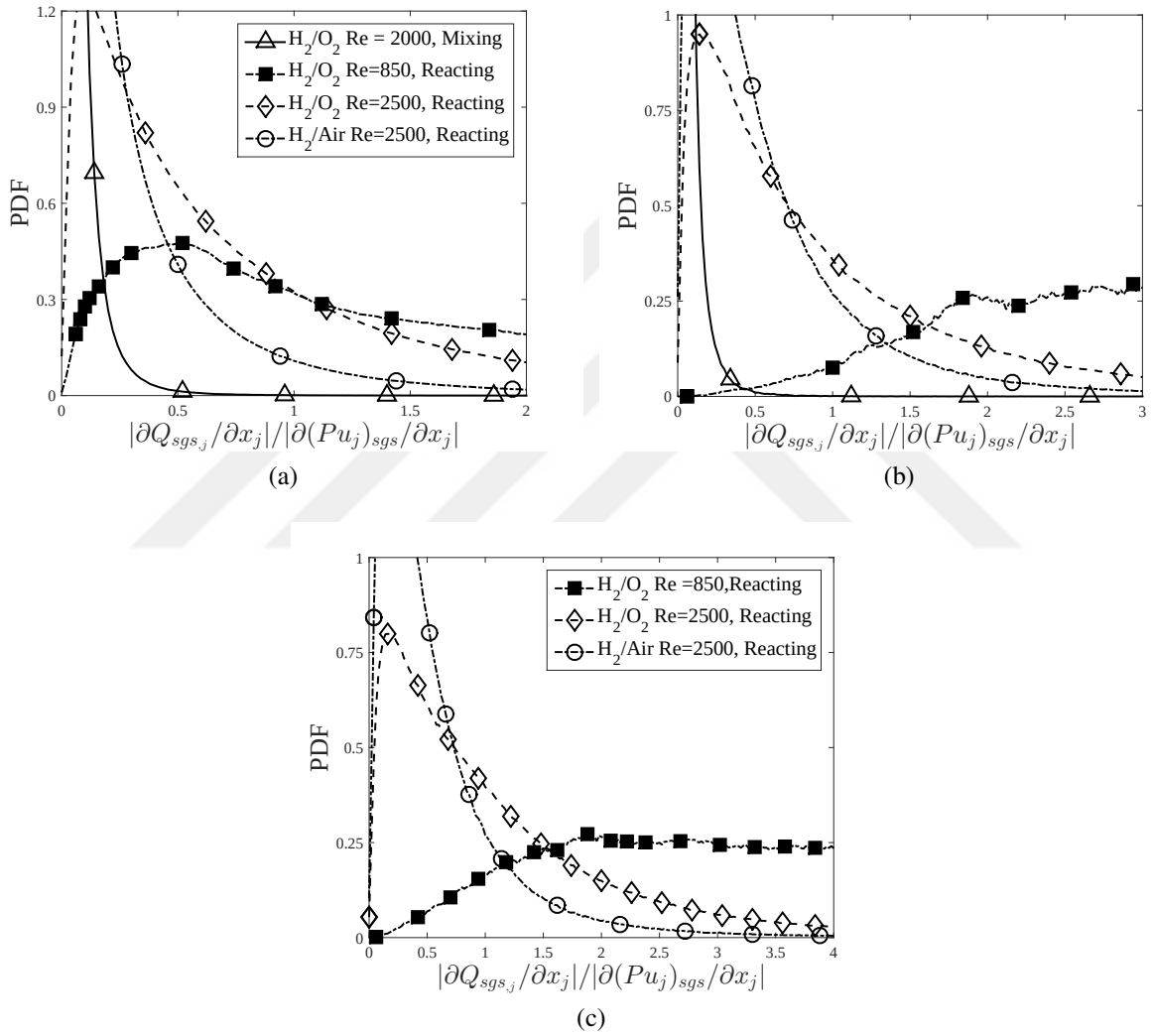


Figure 1.7: PDFs of $|\partial Q_{sgs_j}/\partial x_j|/|\partial(Pu_j)_{sgs}/\partial x_j|$, in regions described by: (a) $0.01 \leq \phi \leq 0.99$, (b) the stoichiometric surface, and (c) $\dot{\omega}^{OH}/E(\dot{\omega}^{OH} \geq 2)$.

Chapter 2

Kerosene / Air Reacting Shear Flows Including Soot Formation/Oxidation With Radiative Heat Transfer

2.1 Introduction

In combustion of hydrocarbons (i.e. fossil fuels) soot formation is an unavoidable phenomenon that has been studied by scholars for decades. Essentially, soot is formed in the fuel-rich side of the flame due to the lack of oxidizer (i.e. incomplete combustion) [59]. The gaseous hydrocarbons are transformed into soot which are basically solid state carbon [39]. In the process of soot formation and oxidation there are 4 steps that occur: I - particle inception/nucleation which are considered as the origin of soot formation, II - a) surface growth which occurs when the gas phase species stick to the surface of soot particles [10] , and b) coagulation where the small-scale soot particles unite to generate large-scale soot particles [10, 39], III - aging, and IV - surface oxidation where soot particles are oxidized by mainly O_2, O and OH molecules yielding gaseous CO and CO_2 etc. [10, 39]. Despite extensive work, the interaction between flow characteristics and soot formation/oxidation are still relativel.y poorly understood. In order to gain more insight about this phenomenon researchers have used different soot models that can be sorted in a list of three : I - fully empirical correlations,

II - semi-empirical schemes that involve using some experimental inputs to solve soot formation rate equations, and III - detailed models that attempt to solve the rate equations which are associated with soot formation [39]. Even though empirical models have been accepted and used widely, the dependency on experimental inputs reduces them to be defined and restricted by the experimental setups [39]. This has forced scholars to pursuie more generalized alternative schemes (i.e. detailed chemistry models). The detailed chemistry models aim to define the chemical kinetics of polyaromatic hydrocarbons (PAH) and surface growth of soot particle globally [39].

However, when adopting such aforementioned soot models for sooting flames is coupling with radiation heat transfer is typically required. The radiative heat transfer within both lightly and heavily sooting laminar/turbulent flames has been modeled in many ways. Due to the massive computational cost and work, relatively simpler radiation models have been adopted widely by the turbulent combustion community. These models primarily aim to couple thermal radiation and soot formation/oxidation processes under the following assumptions. Inherently, soot particles are profoundly small and possess a perfect spherical geometry [48, 59]. This assumption implicitly adopts the Rayleigh Scattering, that was proposed by Lord Rayleigh [59]. Owing to having such small sizes, soot particles' temperature is the same as the flame temperature, hence they emit radiative energy more actively than gaseous molecules (i.e. combustion products) do [59]. Assuming the participating medium is negligibly scattering and formed by a number of gray gases [59], leads scholars to the concept of the weighted-sum-of-gray-gases (WSGG) approach. WSGG helps academics to calculate the absorption coefficient of the appropriate gases (i.e. in this case they are CO_2, H_2O and CO) [59, 100]. The negligible scattering assumption with Rayleigh scattering allowed for the calculation of the absorption coefficient of soot particles as well [59]. The optical thickness of the medium is also an important parameter for the radiation models. The medium can be optically thin or thick depending on how sooty the flame is [77]. Optically thin and gray medium assumption says that emitted radiation will leave the medium due to the lack of self-absorption or scattering [2, 87] (i.e. lightly sooting flames). While the Planck mean extinction coefficient is recommended for the optically thin problems, the Rosseland-mean extinction coefficient is recommended for optically thick mediums [2, 59]. Both

optically thin and thick assumptions have been extensively used in order to analyze the interaction between soot formation/oxidation processes and radiative heat loss.

Inherently capturing soot formation/oxidation coupled with radiation heat loss is a highly challenging process. As a result of the complexity of this process researchers generally neglect real gas effects (i.e. ideal gas law is adopted), and used higly simplified forms of the mass and heat flux vectors (often with a unity Le number assumption). These simplifications may cause a failure while predicting the flames characteristics, since at high pressures many fuels exhibit real gas effects inconsistent with the ideal gas law. There is therefore a need for a better understanding of such a phenomena.

The following sections of this chapter provide an analysis of a generated DNS database of both atmospheric and high pressures $Kerosene/Air$ reacting shear flames. As before the DNS solves the fully compressible form of the continuity, momentum, total energy, and all species' partial density equations in a temporarily developing reacting shear layer geometry. The Peng-Robinson real gas state equation, real property models, and generalized heat and mass diffusion are also incorporated. The chemical reaction is calculated by a reduced pressure dependent 29-step and 10-species (including soot) mechanism [94] for the $Kerosene/O_2$ flame. N_2 assumed to be inert.

2.2 Objectives

Based on the above, the primary objectives of this chapter are to: (I) conduct a comparison between the results of the atmopsheric pressure flames with the limited literature to validate the adopted soot model in this work, (II) investigate the real gas effects on the soot formation/oxidation processes by conducting a comparison with the IGL EOS model resullts, (III) study effects of the pressure on the processess of soot formation/oxidation and effectivity of the IGL EOS model in the flames of high ambient pressures.

2.3 Chemical Kinetics and Numerical Approach

The reduced chemistry which is the basis of the DNS calculation includes a pressure dependent 29-step 10-species and soot ($C_{12}H_{24}$, O_2, H_2O, OH, H, O, CO,N_2, H_2 and CO_2) mechanism developed by Wang [94]. Table 3.1 provides the details of the mechanism. In Table 3.1, Wang [94] has suggested $C_{12}H_{24}$ as a generic formula of kerosene or RP-1. $C_{12}H_{24}$ has been modeled kinetically having 41.7% paraffin and 58.7% napthene to be matched to $\frac{41}{56}$ for paraffin/napthene as reported in the literature. The balance between paraffin and napthene is highly important in order to catch the correct soot prediction since napthene' s breakdown process to soot is quicker than paraffin's [94]. $C_{12}H_{24}$ has been modeled to be a mixture of many pure elements that have the same average thermopysical−chemical profiles of the reported keresone/RP−1 [94]. Consequently, having $C_{12}H_{24}$ as one−formula parent fuel includes the advantages of multiple fuel models while increasing the computational efficiency [94]. A summary of the comparison of the surrogate fuel' s thermophysical−chemical characterization is given in the Table 3.2 [94]. The detailed list of the data has been used for comparison, and can be found in Ref. [94].

Paraffin (straight − chain hydrocarbon) and napthene (cyclic − chain hydrocarbon) irreversible breakdown processes have been depicted with two global steps, and Wet−CO mechanism turns the intermediate species into the final products in Table 3.1 [94]. The reaction rates of global steps of paraffin and napthene have been adjusted in agreement with the ratio of two hydrocarbons, $C_{12}H_{24}$ (proposed surrogate by Ref. [94]). The forth−order polynomial temperature dependent heat capacity form is shown in Eq. (3.2) [94], and Eq. (3.1) [94] is integrated from Eq. (3.2) to calculate enthalpy [94]. The coefficients of Eq. (3.2) and (3.1) are listed in Table 3.3 [94].

$$\frac{H}{RT} = a_1 + \frac{a_2}{2}T + \frac{a_3}{3}T^2 + \frac{a_4}{4}T^3 + \frac{a_5}{5}T^4 + \frac{a_6}{T} \tag{2.1}$$

$$\frac{C_P}{R} = a_1 + a_2T + a_3T^2 + a_4T^3 + a_5T^4 \tag{2.2}$$

The DNS data is calculated by solving the governing equations for 3D, temporally developing,

Reaction[1]	A	B	E/R	Form	Ref.
		Parafin Global Step			
$C_{12E+}H_{24} + 6O_2 \rightarrow 12CO + 12H_2$	3.888E+04	1	1.220E+04	$p^{0.3}[C_{12}H_{24}]^{0.5}[O_2]$	[94]
		Naphthene Global Step			
$C_{12}H_{24} + 6O_2 \rightarrow 12CO + 12H_2$	2.132E+07	1	1.965E+04	$p^{0.3}[C_{12}H_{24}]^{0.5}[O_2]$	[94]
		Wet CO Mechanism[2]			
$H_2 + O_2 = OH + OH$	1.700E+13	0	2.407E+04	Standard	[95, 20]
$OH + H_2 = H_2O + H$	2.190E+13	0	2.590E+03	Standard	[95, 20]
$OH + OH = O + H_2O$	6.023E+12	0	5.500E+02	Standard	[95, 20]
$O + H_2 = H + OH$	1.800E+10	1	4.480E+03	Standard	[95, 20]
$H + O_2 = H + OH$	1.220E+17	-0.91	8.369E+03	Standard	[95, 20]
$M + O + H = OH + M$	1.000E+16	0	0	Standard	[95, 20]
$M + O + O = O_2 + M$	2.550E+18	-1.0	5.939E+04	Standard	[95, 20]
$M + H + H = H_2 + M$	5.000E+12	0	0	Standard	[95, 20]
$M + H + OH = H_2O + M$	8.400E+12	-2.0	0	Standard	[95, 20]
$CO + OH = H + CO_2$	4.000E+12	0	4.030E+03	Standard	[95, 20]
$CO + O_2 = CO_2 + O$	3.000E+12	0	2.500E+04	Standard	[95, 20]
$CO + O + M = CO_2 + M$	6.000E+13	0	0	Standard	[95, 20]
		Soot Formation Global Step			
$C_{12}H_{24} \rightarrow 12C_s + 12H_2$	1.11935E+16	-1.94	1.610E+04	$[C_{12}H_{24}]^{1.81}[O_2]^{-0.5}$	[94]
		Heterogeneous Soot Oxidation			
$C_s + 0.5O_2 \rightarrow CO$	1	0	0	$72R_{ox}[C_s]/(\rho_s D_s)$	[94]
$R_{ox} = K_A P_{O_2}\chi/(1 + K_Z p_{O_2}) + K_B p_{O_2}(1 - \chi)$	-	-	-	-	[61]
$\chi = 1/(1 + (K_T/K_B)pO_2$					
K_A	2.0000E+01	0	1.5098E+04	-	
K_B	4.4600E-03	0	7.6497E+03	-	
K_T	1.5100E+05	0	4.8817E+04	-	
K_Z	2.1300E+01	0	-2.063E+03	-	
		Homogeneous Soot Oxidation			
$C_s + OH = CO + H$	1.2200E+09	0.5	0	Standard	[94]

[1] $K_f AT^B e^{-E/RT}[A][B]$. M stands for third body collisions.
[2] Wet CO mechanism flames whose initial mixture contains small amounts of hydrogen and water vapor.

Table 2.1: Kerosene quasi global combustion kinetics mechanism [94].

Property	Kerosene	$RP-1$	Surrogate Fuel
Molecualr Formula	-	-	$C_{12}H_{24}$
Molecular Weight	175	172 – 175	168
Elemental Formula	-	$CH_{1.95} - C_H 2.0$ $CH_{1.9423}$, $CH_{1.953}$	$CH_{2.0}$
Formula Weight	-	13.97 – 14.03, 13.97	14.03
H_c kcal/g	−10.278 −10.321	−10.241 −10.356	−10.278
$H_{f,298K}$ kcal/mole	-	$-5.430/CH_{1.9423}$	$-92.200/C_{12}H_{24}$ $-7.683/CH_{2.0}$
$C_{p,516K,1atm}$ cal/mole.K	-	101	103
Paraffins (n and iso), %	-	41	41.7
Napthene, %	-	56	58.3
Aromatics, %	5	5	0
Olefins, %	1	0	0

Table 2.2: Comparison of thermophysical−chemical characterization of model fuel with reported data [94].

Coefficient	1000 to 5000 K	300 to 1000 K
a_1	0.36440206E+02	0.39508691E+01
a_2	0.54614801E-01	0.10207987E+00
a_3	-0.16091121E-04	0.13124466E-04
a_4	0.21478497E-08	-0.76649284E-07
a_5	-0.10131180E-12	0.34503763E-10
a_6	-0.63890109E+05	-0.52093574E+05
a_7	-0.12798973E+03	0.21980951E+02

Table 2.3: Thermodynamic coefficients for C_P of $C_{12}H_{24}$[94].

non-premixed reacting shear layers of $C_{12}H_{24}/Air$. Details of the computational domain, mesh and numerical scheme used can be found in Ref. [23]. The mixing occurs at the center of the domain. For the current work, 12 distinct reacting simulations are considered for $Re_F = 2500$ can be seen in the Table 3.4. Four of the simulations include artificially enhanced radiation heat flux due to the soot and CO_2, H_2O and CO gaseous species, in order to observe its effects on the soot production/oxidation processes and flame characteristics with generalized diffusion (i.e. non-unity Le number). The initial temperature is 700 K for all the cases and four different ambient pressure are employed for the current work to be 1, 5, 10 and 35 atm. The convective Mach number is set to be 0.35.

Run	Oxidizer	$P_0(atm)$	EOS	Le	$T_0(K)$	Re_0	$N_1 \times N_2 \times N_3$	t_f^*	Radiation
1	Air	1	RG	$\neq 1$	700	2500	$320 \times 516 \times 180$	65	No
2	Air	1	IG	$\neq 1$	700	2500	$240 \times 480 \times 144$	65	No
3	Air	5	RG	$\neq 1$	700	2500	$304 \times 564 \times 180$	80	No
4	Air	5	RG	$\neq 1$	700	2500	$304 \times 564 \times 180$	80	Yes
5	Air	5	IG	$\neq 1$	700	2500	$304 \times 564 \times 180$	80	No
6	Air	5	IG	$\neq 1$	700	2500	$304 \times 564 \times 180$	80	Yes
7	Air	10	RG	$\neq 1$	700	2500	$304 \times 480 \times 180$	80	No
8	Air	10	RG	$\neq 1$	700	2500	$304 \times 481 \times 180$	80	Yes
9	Air	10	IG	$\neq 1$	700	2500	$304 \times 564 \times 180$	80	No
10	Air	10	IG	$\neq 1$	700	2500	$304 \times 564 \times 180$	80	Yes
11	Air	35	RG	$\neq 1$	700	2500	$304 \times 630 \times 210$	80	No
12	Air	35	IG	$\neq 1$	700	2500	$304 \times 640 \times 180$	65	No

Table 2.4: Summary of simulation parameters from all cases considered. P_0 is initial pressure, T_0 is the initial temperature, Re_0 the initial Reynolds number, N_1, N_2 and N_3, are the number of grid points in the x_1, x_2, and x_3, direction respectively, and t_f^* is non-dimensionalized final simulation time.

2.4 Soot Model

As discussed earlier, soot models consist of 4 steps: nucleation, growth, aging and oxidation. Due to the extremely complex nature of soot formation many researchers aim to reduce the complexity by only treating the most significant steps of the process [48]. Studies frequently investigate the soot load and its effect on flame characteristics and temperature due to radiative heat loss [48]. Researchers have reported that pressure and additive gaseous species have significant effects on the soot formation

mechanism [13, 15, 16, 50]. With increasing ambient pressure soot formation (i.e soot volume fraction or soot mass fraction) increases dramatically due to the higher operating temperatures.

Due to the limitation of empirical and semi-empirical methods most studies incorporate detailed mechanism models. One model that has a 4-step soot model for non-premixed includes nucleation, growth, particle coagulation and oxidation has been proposed by Leung *et al.*[44]. Recently, Lignell *et al.* [46, 45] have conducted both 2-D and 3-D soot analysis in an ethylene flame. Lignell [44] has used Leung *et al.*'s [44] model that assumes monodsipersed size distribution defined by soot particle number density, n, and soot mass fraction [48]. The model has the following steps [48]:

$$\text{I- Nucleation : } C_2H_2 \rightarrow 2C_{(s)} + H_2$$
$$\text{II- Growth : } nC_{(s)} + C_2H_2 \rightarrow (n+2)C_{(s)} + H_2$$
$$\text{III- Oxidation : } C_{(s)} + \tfrac{1}{2}O_2 \rightarrow CO$$
$$\text{IV- Coagulation : } (n) \rightarrow (n-1)$$

where $C_{(s)}$ corresponding to soot implying gas−state graphite carbon [44]. In the first step Leung *et al.* [44] have assumed that C_2H_2, acetylene, begins the soot nucleation, but it is not necessarily the parent fuel of the mechanism. Acetylene is produced as a result of the fuel breakdown mechanism [44]. While napthene and aromatic hydrocarbons are instantaneously condensed to form PAH which are known to be soot ancestors, paraffins have to be decomposed into napthenes and aromatics and eventually form PAHs [94]. This work adopts a soot formation global step that soot is formed directly from the parent fuel, $C_{12}H_{24}$, instead acetylene suggested by Ref. [94]. Even though in early stages soot contains large amount of H_2 molecules, lack of generalized representation of soot leads researchers to assume pure C_s [44]. The second step of the model represents the surface growth process assuming that C_2H_2 in the gas state sticks to the surface of soot particles [44]. Surface growth of soot usually occurs in the high-temperature flame regions [5]. Leung *et al.* [44] adopted the following reaction rate source term suggested by Harris *et al.*[31];

$$R_2 = k_2(T) f(S) [C_2H_2], \tag{2.3}$$

where $[C_2H_2]$ is the molar concentration in $kmol/m^3 - mixture$ and S is the soot surface area in

$m^2/m^3 - mixture$. Leung *et al.* [44] have defined the surface area as:

$$S = \pi(d_p^2)(\rho N) = \pi\left(\frac{6}{\pi}\frac{1}{\rho_s N}\frac{Y_s}{N}\right)^{\frac{2}{3}}, \tag{2.4}$$

where d_P is the soot particle diameter (250×10^{-8} in this study [94]), ρ is the gaseous species density, ρ_s is the soot density taken here as 2000 kg/m^3 [48, 44, 94], Y_s is the soot mass fraction, N $[particles/kg - mixture]$ [44]. The third step is the soot oxidation process includes O_2, OH and O molecules. Even though OH and O aggressively attack soot in order to oxidate it, in most cases they have been excluded from models since their mass fractions are insignificant in comparison to the O_2 mass fraction [77] . The current work adopts heterogeneous (O_2) and homogeneous (OH) soot oxidation steps [94]. The three steps given above lead to the number density equation [44]. The particle number density is reduced by agglomeration that can be summarized with the forth step listed above [44]. Since the current work only study to research soot effects on flame characteristics, only soot formation and soot oxidation mechanisms are adopted. For only comparison purposes with literature Eq. (3.5) is adopted from Ref. [103] to calculate the soot particle number density which is associated to soot mass fraction:

$$N = Y_s 6\left(\frac{\rho_t}{\rho_s}\frac{1}{\pi d_p^3}\right), \tag{2.5}$$

In addition to the governing equations have been defined in the Chapter 2 [(Eq.(2.1 - 2.5)] one additional governing equation is adopted to calculate the soot mass fraction of Ref. [48]:

$$\frac{\partial(\rho Y_s)}{\partial t} = -\frac{(\rho Y_s v_i)}{\partial x_i} - \frac{\partial j_{s,i}}{\partial x_i} + S_{Y_s}\ , \tag{2.6}$$

$$\frac{1}{\rho_t} = \frac{Y_s}{\rho_s} + \frac{1 - Y_s}{\rho}, \tag{2.7}$$

where Y_s is the soot mass fraction, ρ is the gaseous species density calculated with Eq. (3.7) Ref. [103], $j_{s,i}$ is the soot diffusion calculated with Eq. (3.8) [48], and S_{Y_s} is the reaction term for soot. The

soot mass diffusion based on thermophoretic effects is calculated as:

$$j_{s,i} = -0.556\ \rho Y_s\ \frac{\nu}{T}\nabla T. \tag{2.8}$$

which is taken from Ref [48]. Since thermophoretic effects are considered insignificant in comparison to the turbulent advection, it is usually ignored [103]. However, it is included in the current study for the sake of completeness.

2.5 Radiation Model

A complete combustion model should include radiative heat transfer in order to predict the flame formation, production of solid particles (i.e. soot), localized radiative heat flux and flame temperature [92]. For decades researchers have attempted to propose radiative heat transfer models which are not only low on computational cost but also accomplish 'accurate' radiative heat loss predictions. Since chemical kinetics of soot processes are intensely temperature dependent, anticipating the flame temperature is critical in sooting flames [92].

The accuracy of combustion models can be affected by the accuracy of the radiative heat transfer model (RHTM) adopted to predict flame temperature [92]. Inaccurate prediction of flame temperature can cause combustion models to fail to estimate flame characteristics accurately. Choosing appropriate an RHTM is affected by the nature of the problem, computational costs, desired degree of accuracy, and medium of the system [92]. Optically thin and gray medium assumption has been adopted with a view of a cold surrounding leads to the following [1, 59, 92] :

$$Q_{\alpha,rad} = 4\ \sigma\ \sum p_\alpha * a_{p,\alpha} \times (T^4 - T_\infty^4) \tag{2.9}$$

where σ is the Steffan−Boltzman constant (= $5.699 \times 10^{-8}\ W/m^2K^4$), p_α is the partial pressure of species α, $a_{p,\alpha}$ is the Planck mean absorption coefficient of species α, T is the instantaneous flame temperature in Kelvins and T_∞ is the ambient temperature consisted with an assumption of emission-only medium [1].

	H_2O	CO_2
C_0	−0.23093	18.741
C_1	−1.12390	−121.310
C_2	9.41230	273.500
C_3	−2.99880	−194.050
C_4	0.51382	56.310
C_5	$-1.8684\ 10^{-5}$	−5.8169

Table 2.5: The coefficients used to calculate Planck mean absorption coefficient of H_2O and CO_2 [1].

	$T(K) \leq 750K$	$T(K) \geq 750K$
C_0	4.78690	10.0900
C_1	−0.09530	−0.01183
C_2	$2.95775\ 10^{-4}$	$4.77530\ 10^{-3}$
C_3	$-4.25732\ 10^{-7}$	$-5.816909\ 10^{-10}$
C_4	$2.02894\ 10^{-10}$	$-2.5334\ 10^{-14}$

Table 2.6: The coefficients used to calculate Planck mean absorption coefficient of CO [1].

The temperature dependent Planck mean absorption coefficient of H_2O and CO_2 are given by Eq. (3.10) [1], and the coefficients used to calculate the curve fit are listed in Table 3.5 [1].

$$a_{p,\alpha} = C_0 + C_1 \times (\frac{1000}{T}) + C_2 \times (\frac{1000}{T})^2 + C_3 \times (\frac{1000}{T})^3 + C_4 \times (\frac{1000}{T})^4 + C_5 \times (\frac{1000}{T})^5 \tag{2.10}$$

Equation (3.11) [1] gives the Planck mean absorption coefficient of CO and the coefficients for this curve fit are listed in Table 3.6 [1].

$$a_{p,CO} = C_0 + T \times (C_1 + T \times (C_2 + T \times (C_3 + T \times C_4))) \tag{2.11}$$

As mentioned earlier, soot particles are very small and Ragleigh scattering theory can be adopted at relevant wavelengths [59]. The extinction coefficient can be estimated by [59]:

$$\kappa_\lambda = \beta_\lambda = C_0 \frac{f_v}{\lambda}, C_0 = \frac{36\pi nk}{(n^2 - k^2 + 2^2) + 4n^2k^2} \tag{2.12}$$

where C_0 is a soot index refraction dependent constant [59], and fv is the soot volume fraction

($fv = \rho_t * Y_s / \rho_s$ [48]). Felske *et al.* [22] have proposed an average value for the Planck−mean and the Rosseland−mean extinction coefficient:

$$\kappa_m = \beta_m = 3.72 f_v C_0 \frac{T}{C_2} \tag{2.13}$$

where $C_2 = 1.4388 cm.K$ is the second Planck function constant Equation (3.13) can only be adopted while working with very small particles for both optically thin and thick mediums [59]. The radiative heat transfer can now be calculated by Eq. (3.9) coupled with the energy equation Eq. (2.3).

2.6 Real Gas and Pressure Effects on Soot Formation Including Radiative Heat Transfer

Practical devices such as gas turbines, internal combustion engines and diesel engines often operate at supercritical pressures [101]. In such systems adopting the IGL EOS has been known to be potentially invalid due to real gas effects [101]. Even though adopting more realistic mathematical models are required to eliminate the errors from the IGL EOS simplifications, researchers tend to employ the IGL EOS based models for atmospheric and elevated pressures [13] for both laminar [13, 14, 15, 16, 42, 49, 51, 50, 83, 84, 86] and turbulent [103, 5, 17, 77, 97, 6, 77, 100, 3, 99, 9, 29, 69, 87, 98, 80, 48] radiating non-premixed reacting flows. The literature suffers from nonavailability of turbulent non-premixed flame studies with high pressure real gas effects, and generalized diffusion phenomena.

Liu *et al.* [49] have conducted an atmospheric (with the IGL EOS) laminar ethylene-air co-flow jet diffusion flame calculations employing the modified semi-empirical soot model of Ref. [44] and the optically thin (OTM) and the discrete ordinates radiation model (DOM) considering spectral absorption coefficients of H_2O, CO_2 and CO . Ref. [49] has employed a different soot oxidation model based on the results of Refs. [8, 62, 61, 60]. They have adopted the Nagle-Strickland-Constable O_2 soot oxidation model [61] with the rate constants of Ref. [60] and Bradley *et al.*'s [8] O radical soot oxidation rate constants. Neoh *et al.* [62] have shown the importance of O_2 and OH soot oxidations

depending on these two species concentration, and Bradley *et al.* [8] have stated that O radical also oxidizes the soot particles. Ref. [49] has reported that there is only a 5 K difference between the DOM and the OTM' s peak temperature predictions. The soot volume faction, nucleation, growth and OH soot oxidation predictions have been noted to be better predicted with the OTM radiation model even though it slighlty under-predicts the mentioned soot quantities [49].

Ref. [14] has employed an acetylene based semi-empirical soot model proposed by Ref. [44] and the DOM of Ref. [49] under atmospheric pressure for lightly sooting methane/air and heavily-sooting ethylene-air flames. The calculated temperature profile of the methane-air flame by Ref. [14] has been reported to be under-predicted by 100-200 K in the centerline and over-predicted at the outer surface of the flame in comparison to experimental data. The methane mole fraction is over-predicted in some regions of the flame by a factor of 4 relative to experimental results by Ref. [14]. While their model cannot exceed Ref. [84]'s predictions in accuracy for both temperature and the methane profiles, the peak soot volume fraction predictions have been reported be better than Ref. [84]'s predictions. The peak soot volume fraction has been over-predicted in both Refs [14, 84] . The numerical results of the ethylene-air flame have been reported to be quite similar to those of Liu *et al.* [49]. Both Ref. [14] and [49] under-predict the peak temperature by $\approx$ 120 K. The peak soot volume fraction prediction is slightly over-predicted by $\approx$7 % in comparison to the experimental data by Ref. [14], while Ref. [49] has reported excellent agreement. Soot distribution predictions have been reported to be lower than the measured data in the centerline by Refs [14] and [49].

Charest [13] studied pressure and gravity effects on soot formation in two different laminar diffusion flames I - pure ethylene-air (0.5 to 5 atm) and II- pure methane-air (1 to 60 atm) by employing the IGL EOS, the semi-empirical soot model of Ref. [44] and the DOM for radiative heat flux calculations. Even though overall soot predictions are not in agreement with from the experimental data, the effects of pressure and prediction of the trends has been captured adequately in Ref. [13]. The predicted flame heights have been observed to be shorter, especially for the high pressures, due to the under-predicted near wall temperatures for the ethylene-air flames, whereas flame heights have been over-predicted in the methane-air flames (i.e. over-predicted near wall temperatures) for all pressures [13]. Charest

Ref. [13] has addressed the differences between zero and normal-gravity flames at the same operation pressures in the methane-air flames. In their work, zero-gravity flames tend to have higher soot, lower temperature and wider soot regions than normal-gravity flames when the pressure is higher than 10 atm [13].

Liu *et al.* [50] have studied axisymmetric co-flow laminar pure methane-air diffusion flames both numerically and experimentally to examine the pressure effect on the flame structure and soot production at pressures varying from 5 to 40 atm by adopting the IGL EOS and a semi-empirical soot model of Ref. [44] including O_2, OH and O soot oxidation and the DOM [50]. The experimental results they have obtained (for pressures 1 to 80 atm) showed that flame height increases between 1 to 5 atm, and remains almost constant between 5 to 20 atm and then begins to lower with linear dependency on the pressure [50]. Their numerical model has slightly over-predicted the flame heights for 5 to 20 atm, and poorly catches the shrinkage of the flame for the higher pressures [50]. Liu et *al.* [50] have adopted two different surface growth rate models (linear and non-linear dependency on soot surface area) to examine the pressure dependency of soot load. They refer to the non-linear model as Model I while referring the linear model Model II [50]. Model I has been reported to anticipate the soot volume dispersions better than Model II, while it is unable to march the accuracy of Model II' s peak soot volume fractions for 5, 20 and 40 atm [50]. Furthermore, they have investigated the soot oxidation effect on soot volume fraction at the same pressures [50]. They have concluded that soot oxidation effect on soot volume fraction decreases with increasing pressure due to the reduction of C_2H_2 concentration while soot production increases which implies the importance of soot oxidation on soot volume fraction predictions [50].

Refs. [15] and [16] adopt the same numerical framework that has been employed by Ref. [13] for laminar flames at elevated pressures (1 to 20 atm) to compare the results with experimental data. Both works have adopted the non-linear soot surface growth rate model (Model I of Ref. [50]), OH and O soot oxidation steps are also added based on Ref. [50]. Charest *et al.* [15] do not only inspect the pressure effect but also look for the effect of CO_2 addition to the fuel (methane) both experimentally and numerically. They have investigated one pure methane, one 80% methane -%20

CO_2, and one % 60 methane-%40 CO_2 flame and they refer to them as F0, F20 and F40, respectively [15]. The experiments have been done at 5 atm and above for F20, and 10 atm and above for F40 flames [15]. While the soot volume fraction predictions have been reported to be significantly lower than the experimental results [15], the experimental trends have been well predicted by the model [15]. The ethylene-air flame in Ref. [16] has been diluted by N_2 to reduce the soot formation with ambient pressures varying from 10 to 35 atm. The model of Ref. [16] generally over-predicts the soot volume fractions while it captures the soot transportation in the flame that have been observed in their experiments.

Lautenberger *et al.* [42] have conducted a study for developing a new soot formation/oxidation model of non-premixed hydrocarbon flames and introduce a primal calibration to the new model. Soot formation and oxidation have been suggested to be temperature and mixture fraction dependent [42]. They have suggested an O_2 soot oxidation step that is independent of soot surface area, as the proposed O_2 oxidation is restrained by O_2 transport into the soot oxidation region (i.e. OH soot oxidation is a surface area dependent process) [42]. Later, by using the relationship between laminar smoke point height and the peak soot formation, the model has been universalized for multiple fuels (i.e. ethylene, propylene and propane) [42]. Their model differs in three ways from the general modeling approach by eliminating the soot number density conservation equation, soot formation is taken to be an explicit function of mixture fraction (i.e. independent of parent fuel and no precursor species, C_2H_2) and independent of fuel laminar smoke point height calculations [42]. The radiation heat flux has been calculated by employing the narrow band radiation model [42]. While their first attempt to globalize the model for the fuels mentioned above captures the trends of the experimental data, quantitatively it is in need to be improved [42]. The simulations were conducted at atmospheric pressure with the IGL EOS [42].

Said *et al.* [77] have studied an atmospheric ethylene-air laminar flame (a laminar version of GENMIX [1] has been used), and a turbulent flame (by employing an Eulerian-Lagrangian approach)

[1]GENMIX handles two-dimensional, parabolic flows, i.e. those of high Reynolds and Peclet numbers, from which recirculation is absent. "Parabolic" flows are those which are:-steady (ie independent of time), predominantly in one direction, defined as that in which the velocity vector nowhere has a negative component; and without recirculation or diffusion effects in that direction. from `http://www.cham.co.uk/phoenics/d_polis/d_enc/parab.htm`

with the OTM for radiative heat flux for both flames [77]. First, they have tested their semi-global soot model on an atmospheric laminar ethylene-air flame [77]. Soot number density has been ignored due to its insignificant effect on atmospheric diffusion flames. Instead of soot number density a mean particle diameter of soot is adopted [77]. They have reported a fairly good agreement with experimental results of Ref. [79], and pointed out the radiation effect on sooting flames [77]. The existence of strong effect of temperature and oxidizer fluctuations' effects on soot formation and destruction process have been emphasized (the observed deviation has been reported to be 200%) [77].

Bai *et al.* [3] have coupled a 2D Favre-averaged k-ϵ and the Boussinesq gradient-diffusion hypothesis for Reynolds stress and transport fluxes with a detailed laminar flamelet modeling for detailed soot model and the OTM has been used for radiative heat flux. Bai *et al.* [3] have not introduced a soot number density transport equation like Ref. [77]. The predicted mean mixture fraction, temperature and soot volume fraction has been reported to be in good agreement with measured data [3]. Radiation has been observed to be effective on soot formation/destruction at low scalar dissipation rates [3].

Yoo and Im [97] have modeled a steady 2D turbulent ethylene-air counterflow non-premixed flame using DNS with a semi-empirical soot model and the DOM for radiative heat flux using the S3D [2] code that solves the fully compressible, 3D reacting Navier-Stokes (N-S) equations with the IGL EOS [46, 45]. They have unveiled the interaction between soot formation/destruction and turbulence of the dependency of soot formation to local flow characteristics, temperature, and fuel load, and the soot number density dependency of the high temperature flame regions [97]. They have observed that turbulence causes an increase in soot load by creating additional flame volume, and a decrease soot load by depleting soot pockets out of the high-temperature flame regions (spending less time in the high-temperature flame regions) [97].

Lignell *et al.* [46, 45] have done two sets of DNS (2D and 3D) atmospheric ethylene-air flame to investigate soot-flame interactions and transport in an unsteady flame structure. The S3D code wtih the OTM has been used for radiative heat flux calculations. They have observed the flame curvature causes transportation of soot either into or away from the flame that leads to widely scattered soot

[2]S3D is a DNS code developed by Sandia National Laboratories that uses finite difference approximations to solve fully compressible N-S equations on Cartesian grids [46].

in the mixture fraction coordinate [46, 45]. They have concluded the importance of considering unsteady and multidimensional effects on soot formation and transport in turbulent flames [46, 45]. Furthermore, they have emphasized the importance of radiative heat loss by running a 2D simulation for 50 ms [46], however, for 3D simulations radiative heat loss has been reported to be insignificant due to large domain size, short simulation run time and low soot concentration of the simulation [45].

Recently Bisetti *et al.* [5] have conducted a 2D DNS of soot formation in a detailed chemical mechanism of an atmospheric n-hephane/air non-premixed flame to examine the unsteady strain effects on soot growth and transport ignoring dissipation, body forces, and Soret and Dufor effects . They have reported that in high scalar dissipation regions soot formation and growth from PAH occurs and related it to the reduction of soot load at high mixing in turbulent sooting flames [5].

In the current work, a semi-global soot production/oxidation of $Kerosene/Air$ turbulent flames have been investigated for atmospheric and elevated pressures using the OTM radiative heat flux assumption for non-unity Le numbers by employing a RGL and the IGL EOS. The results of atmospheric pressure flames have been compared with the limited literature [97, 46, 45]. However, since our research is more complex than the available literature, the results are the first attempt to study soot formation/destruction processes in turbulent hydrocarbon flames with real gas effects at high pressure. The results are represented in Section 3.7. We start by comparing the RGL and the IGL EOS results for atmospheric flames and continue with the results of 5, 10 and 35 atm falmes with Re=2500 and Ma Number (=0.35).

2.7 Results

The general tendency in the literature is using the IGL EOS for hydrocarbon flames due to the complexity of mathematical models of real gas effects. While Figures 3.1 through 3.6 include the mean, rms and raw data (scatter) of normalized T(K), soot volume fraction (fv), number of density (N), soot mass fraction (Y_s), scalar dissipation (χ^{ϕ}) that are conditioned on mixture fraction at time of t_f = 65, Figures 3.7 - 3.9 represent the contour plot of T(K), fv and Y_s of the RGL and the IGL EOS model predictions of 1 atm flames at time of t_f = 65 . Since the gaseous species obey the IGL

EOS at low pressure and high temperatures, it is safe to say employing the IGL EOS for the flames operating at atmospheric pressure is probably a reasonable approach. The atmospheric turbulent flame investigation has significant importance to validate the current work since the literature only exist for atmospheric hydrocarbon flames of soot production/destruction processes. In this manner, the results of atmospheric pressure for different cases have been compared with the literature.

Yoo *et al.* [97] have stated that the high values of the fv do not necessarily exist in high temperature regions. The Figures 3.2, and 3.8 support this by showing the high values of fv exist in a wide portion of the flame volume whose temperature is varies from $\approx$ 1300 K to 1800 K. Furthermore, they have stated that N has been observed to be highly dependent on temperature, while fv is dependent on local flow characteristics [97]. Figures 3.1 and 3.3 support their conclusion on N. The high values of N occupies the high temperature flame region and is scattered widely where the temperature is scattered. Ref. [97] pointed out that effects of transport and turbulence mixing must be taken into account in sooting turbulent flames. In addition, in Ref. [97], in the limited soot production regions, fv has relatively high values which has been explained by a large volume of soot transportation. Similar behavior has also been observed in the current work (Fig. 3.2 and 3.8). These results have been explained by the interaction between soot chemistry and transport [97]. Yoo *et al.* [97] have stated the peak of fv to be 2.4 times larger than the reported value in the literature of steady flames.

Refs [46, 45] have reported that the temperature is not scattered by implying the levels of mixing of their flame is low. In the current work higher levels of mixing have been achieved (Figs. 3.1 and 3.7). This difference could be explained by comparing the scalar dissipations which have been calculated to be an order of magnitude larger than the Refs [46, 45]. (since Ref. [97] and [5] have not provided any scatter plots of temperature, we are unable to compare the temperature scatter plots) Lignell *et al.* [46] have observed two distinct behaviors in Ys plots; I - slow soot nucleation rates force the Ys to have a wide variation on the mixture fraction axes, and II - soot has been carried into the fuel rich side of the flow. As a result of the first behavior, Ys scatter plot represents a dense band of Ys load below its higher range, and second behavior emphasizes the importance of the soot transportation in turbulent flames [46]. A similar trend has been shown in Fig. 3.4. The scatter plots of soot nucleation and

growth rate have been highly effected by the temperature profile in Refs. [46, 45], while in the current work w_{soot} have been shown to be similar to Ys scatter plots (Fig. 3.6). This could be explained with the different levels of mixing. In Ref. [45] the significant difference between the soot and gaseous species and how it affects the soot modeling in turbulent flames have been pointed out (i.e. difficulty of the soot modeling). They have stated that the conditonal standard deviation (rms) of Ys are of the same order of magnitude with the conditional mean, whereas the gaseous species have an order of magnitude smaller rms values than their conditional means [45]. In contrast, the soot nucleation has relatively small rms values since this process is only dependent on the gaseous species [45]. However, in the current work, while their first observation has been observed, the w_{soot} has a higher rms than its conditional means. Figures 3.6 and 3.4 represent the w_{soot} and Ys conditional scatter, mean and rms of these soot quantities. Figure 3.4 is in good agreement with the first observation of Lignell *et al.* [46] while Fig. 3.6 shows a distinct trend for w_{soot} than the one in Ref. [46]. Since, in Ref. [46] the nucleation of soot (w_{soot}) has been shown to be extremely depended on the temperature profile, having a smaller rms of the w_{soot} is an expected behavior. However, in the current work temperature is highly scattered (i.e. higher levels of mixing, Fig. 3.5) and the fuel breaks directly into to the soot a conflicting trend has been observed for the w_{soot}. In the current work, the rms of w_{soot} have been noted to be higher than the conditional means of the w_{soot}.

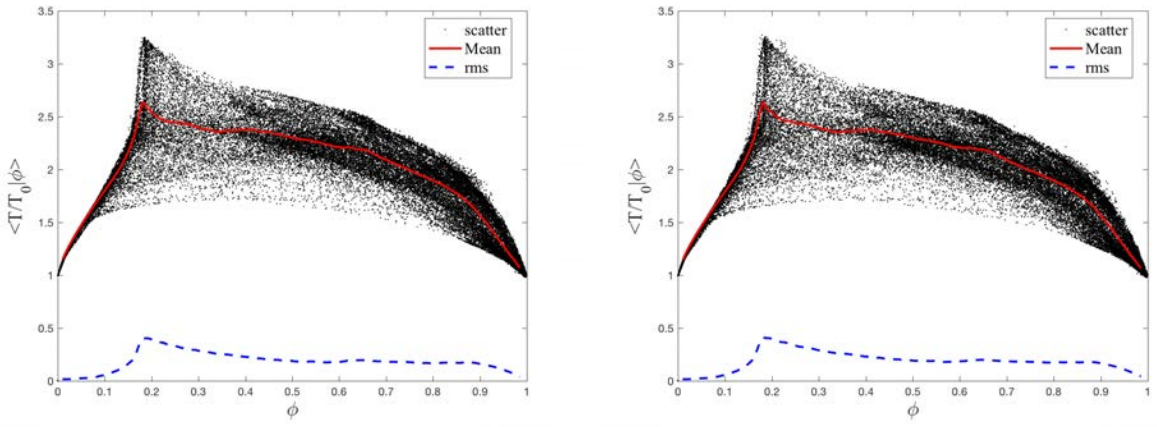


Figure 2.1: On the left the RGL EOS model and on the right the IGL EOS model predictions of $< T/T_0|\phi >$ for Re= 2500, Le $\neq$ 1, and 1 atm ambient pressure at time of 65.

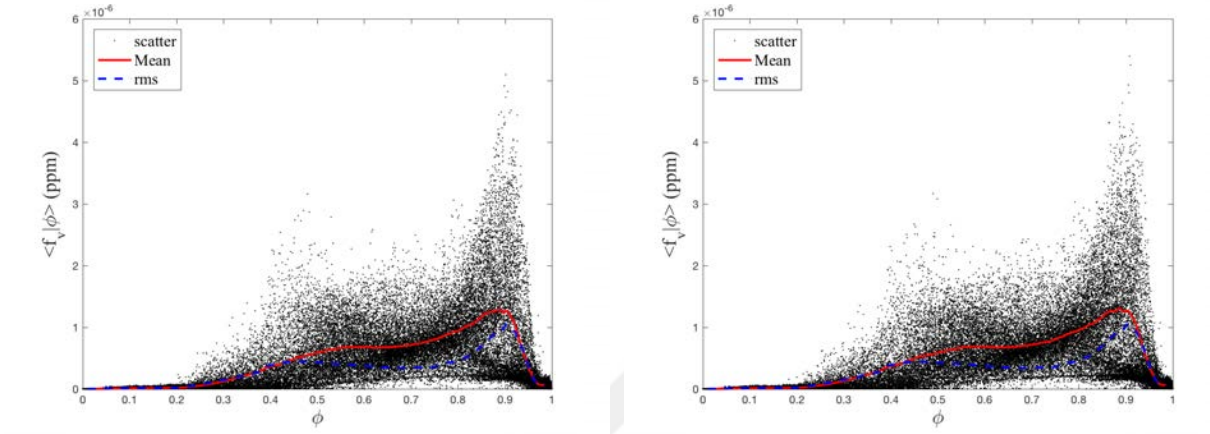


Figure 2.2: On the left the RGL EOS model and on the right the IGL EOS model predictions of $< fv|\phi >$ for Re= 2500, Le $\neq$ 1, and 1 atm ambient pressure at time of 65.

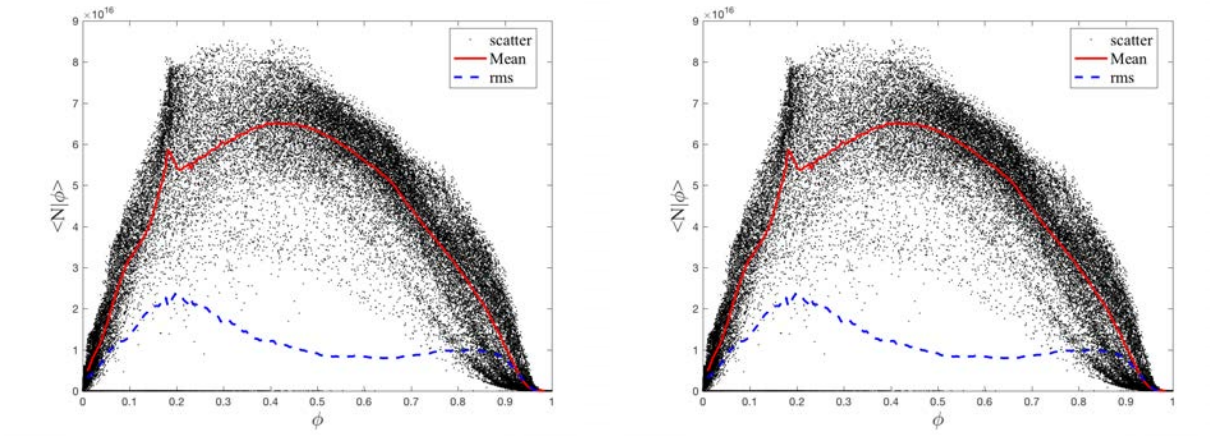


Figure 2.3: On the left the RGL EOS model and on the right the IGL EOS model predictions of $< N|\phi >$ for Re= 2500, Le $\neq$ 1, and 1 atm ambient pressure at time of 65.

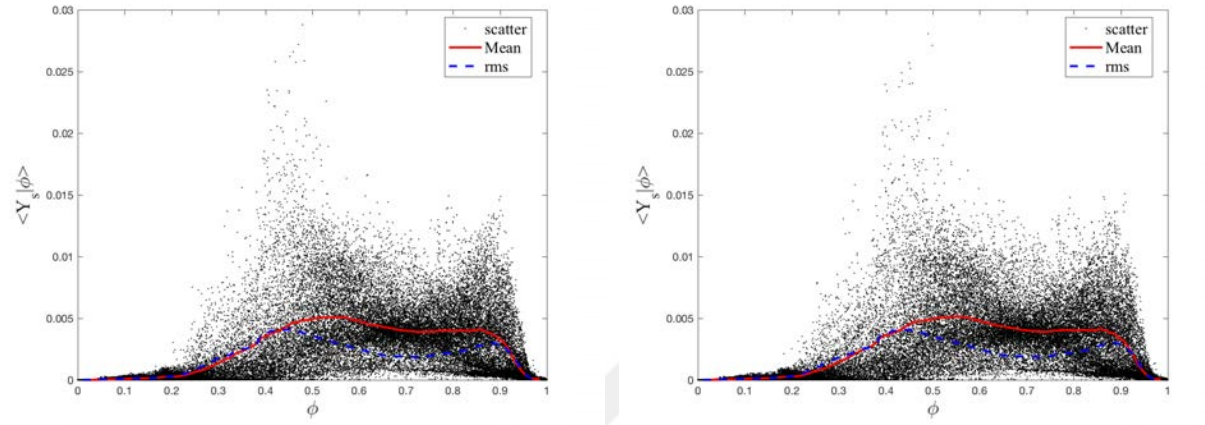


Figure 2.4: On the left the RGL EOS model and on the right the IGL EOS model predictions of $< Ys|\phi >$ for Re= 2500, Le $\neq$ 1, and 1 atm ambient pressure at time of 65.

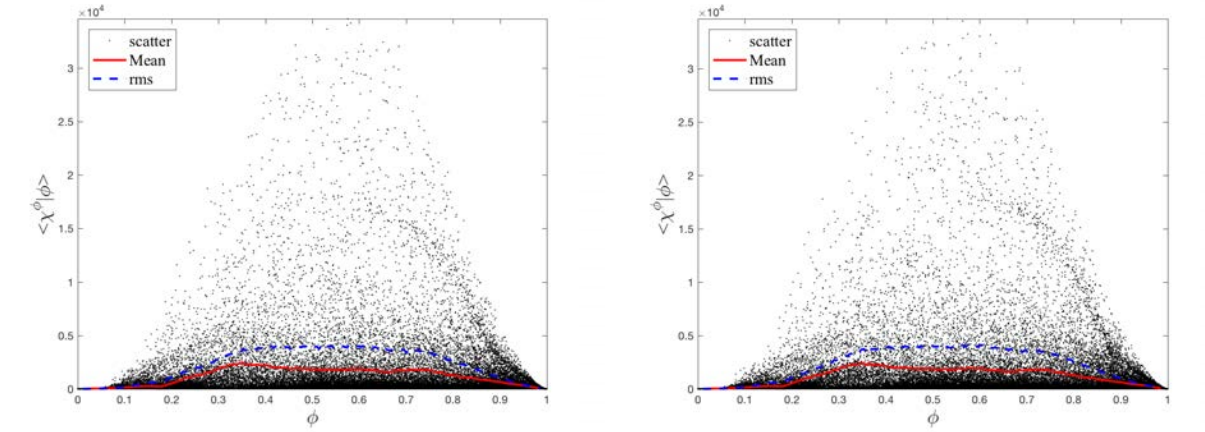


Figure 2.5: On the left the RGL EOS model and on the right the IGL EOS model predictions of $< \chi|\phi >$ for Re= 2500, Le $\neq$ 1, and 1 atm ambient pressure at time of 65.

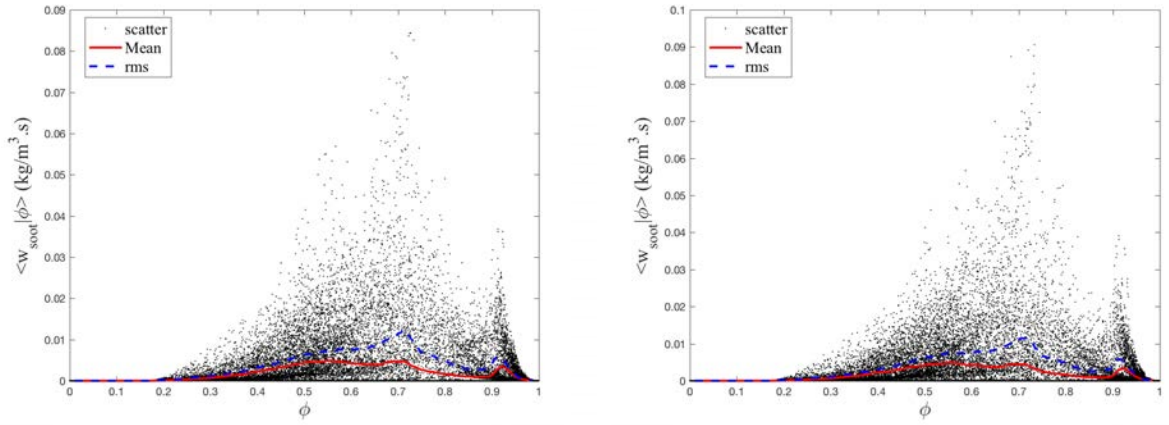


Figure 2.6: On the left the RGL EOS model and on the right the IGL EOS model predictions of $< w_{soot}|\phi >$ for Re= 2500, Le $\neq$ 1, and 1 atm ambient pressure at time of 65.

Figures 3.10 through 3.15 depict the soot and flame characteristics of adiabatic the RGL and the IGL model 5 atm flames. The high levels of mixing still present in both the RGL and the IGL EOS 5 atm flames indicating these two flames should possess the similar flame characteristics of atmospheric flames of the RGL and the IGL EOS have been shown above. As it is expected that increasing pressure enhances the maximum flame temperature which has direct effects on the soot production/oxidation processes. Even though for the RGL and the IGL model flames' temperatures we observe similar behavior in Fig 3.10, when the artificial radiation has taken into account IGL model under-predicts the flame temperature which is 55 K lower than the RGL flame temperature (i.e. 3% difference between the RGL and the IGL models). The artificially enhanced radiation heat loss results the RGL flames to be 172 K, and IGL flames to be 224 K lower than adiabatic flame temperature [Fig. 3.16]. Figures 3.11 and 3.17 reveals the direct effect of temperature on soot production processes. For adiabatic flames of the RGL and the IGL models fv is $\approx 5 \times 10^{-5}$ ppm, while it is reduced by 10% for RGL and 20% for IGL model which emphasizes the significance of the temperature on soot characteristics. Furthermore, fv is still dominated by local flame characteristics [3.10 3.16 3.11 3.17]. However the peak values of N occupy the region where the high flame temperatures are observed once again, N has started to immigrate to the fuel rich side of the flame. In contrast of the atmospheric flames ([3.3]), the standard deviation of N and $< N|\phi >$ conditioned one the mixture fraction are at the same order of

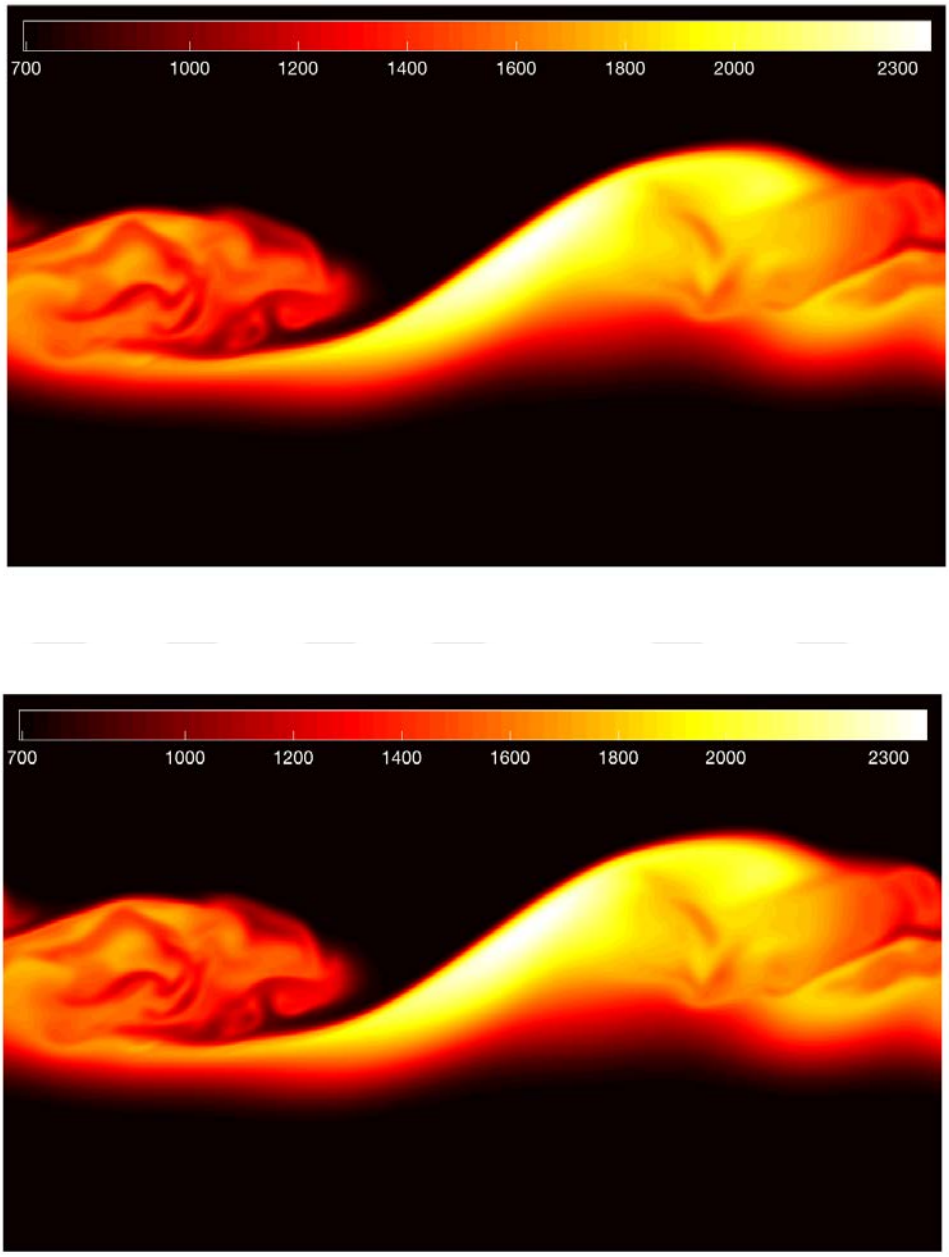


Figure 2.7: Contour plots of T(K) for pressure 1 atm, Le≠1 and Re=2500, top is the RGL model and bottom is the IGL EOS model predictions time of 65, 3D data.

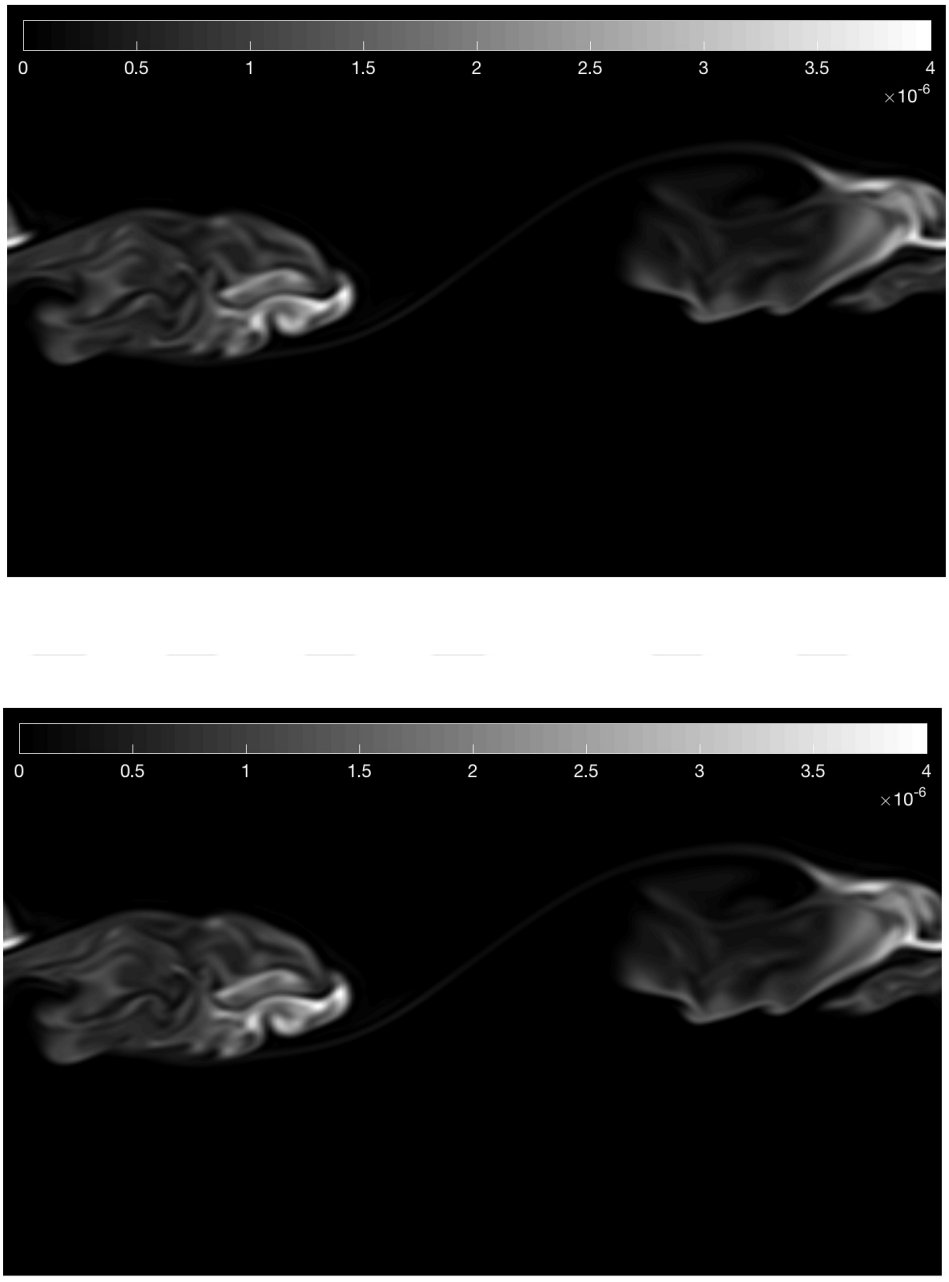


Figure 2.8: Contour plots of fv for pressure 1 atm, Le≠1 and Re=2500, top is the RGL model and bottom is the IGL EOS model predictions time of 65, 3D data.

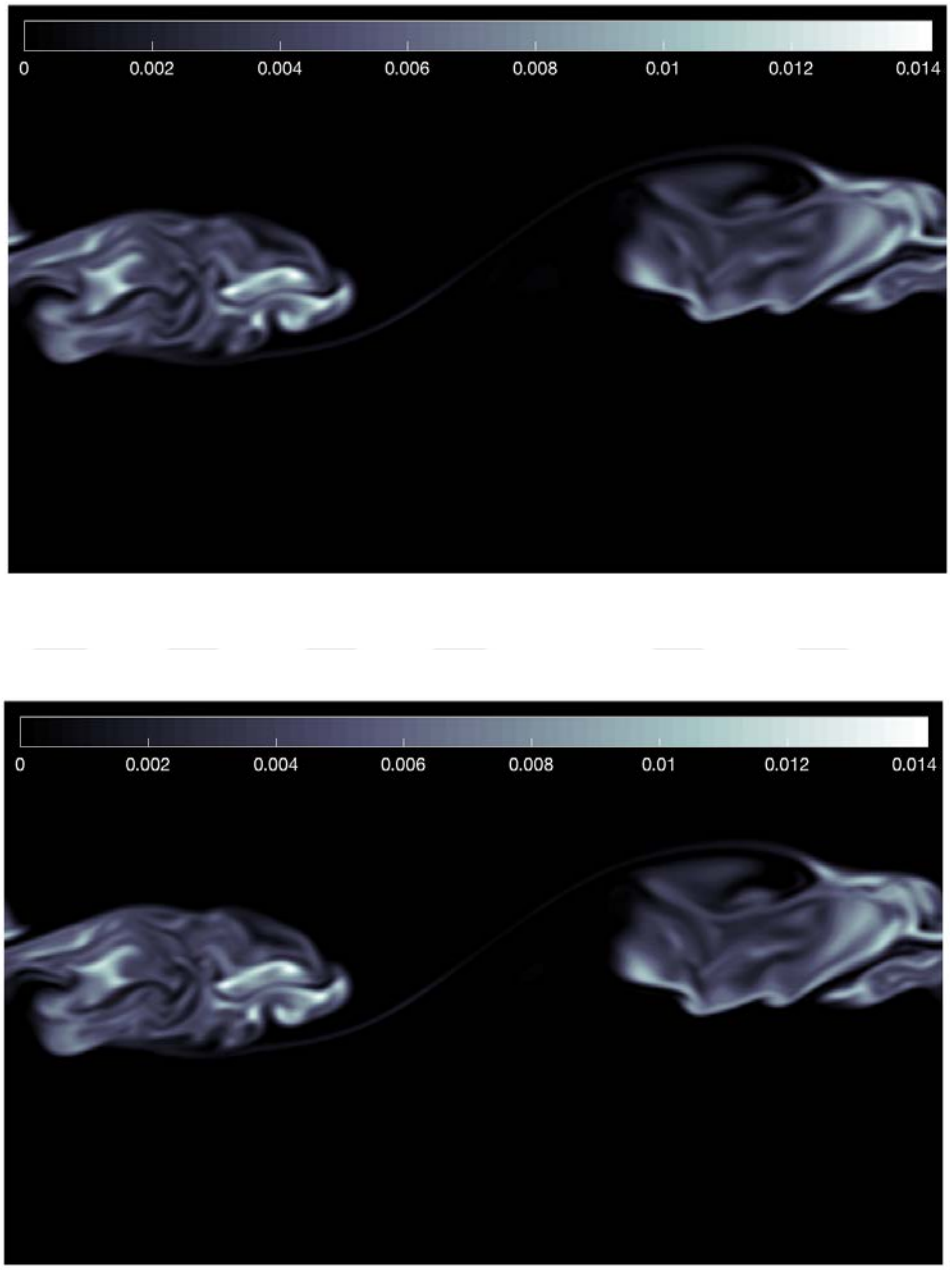


Figure 2.9: Contour plots of Ys for pressure 1 atm, Le≠1 and Re=2500, top is the RGL model and bottom is the IGL EOS model predictions time of 65, 3D data.

magnitude. These two behaviors tell us that N is no longer affected by the flame temperature and like fv and Y_s it will be dominated by local flame characteristics. fv and Y_s of the RGL and the IGL EOS flames at 5 atm ([3.11, 3.17, 3.12 and 3.18]) have very similar behavior with fv and Y_s of atmospheric pressure flames of the RGL and the IGL EOS ([3.2 and 3.4). Figure 3.13 and 3.19 indicate that slow soot formation rates still existed for both the RGL and the IGL EOS flames and soot load is transferred to the fuel rich side. In addition to this, the peak value of Y_s is shifted toward to the fuel rich side of the flame ([3.13 and 3.19]).

While the addition of radiative heat loss causes a reduction on temperature, it has a very insignificant effect on distribution of the flame temperature throughput the domain (3.10 and 3.16]). Figures 3.18 and 3.19 reveal the dramatic reduction on N and Y_s for both the RGL and the IGL EOS flames by 10% and 25% for N, and 30% and 29% for Y_s (i.e. radiative heat loss effect on soot properties). Figures 3.14 and 3.20 show the radiative heat loss on the scalar dissipation rate which turns out to be the most effected flow characteristics for both the RGL and the IGL EOS flames at 5 atm. While the scalar dissipation prediction of IGL is $\approx$ 16 times smaller than RGL model prediction for adiabatic flames of 5 atm [Fig. 3.14], with radiative heat loss the IGL model prediction of χ becomes 15% larger than RGL model prediction. [Fig. 3.20]. Lastly, w_{soot} predictions are about to same for the adiabatic flames of the RGL and the IGL models (w_{soot} of IGL is 4% smaller than RGL) [Fig. 3.15], and it is reduced by $\approx$ 45% for both the RGL and the IGL EOS flames when radiation heat loss added to the calculations [Fig. 3.21]. Overall for the flame and soot characteristics of adiabatic flame of 5 atm is well predicted by the IGL EOS model.

Figures 3.22 through 3.27 depict the soot and flame characteristics of adiabatic10 atm flame, while Figures 3.28 to 3.33 represent the ones of 10 atm with radiation heat loss. However the increasing ambient pressure effect on temperature increment appear in both the RGL and the IGL EOS adiabatic flames ([3.22]), the IGL EOS model flame temperature displays a more scattered behavior than the RGL EOS model' s. The clear effect of temperature on soot properties is observed once again in the 10 atm flames. Figure 3.23 expose that fv is still under local flow characteristics in both the RGL and the IGL EOS adiabatic flames. Even though flame temperatures increase by increasing pressure there is a

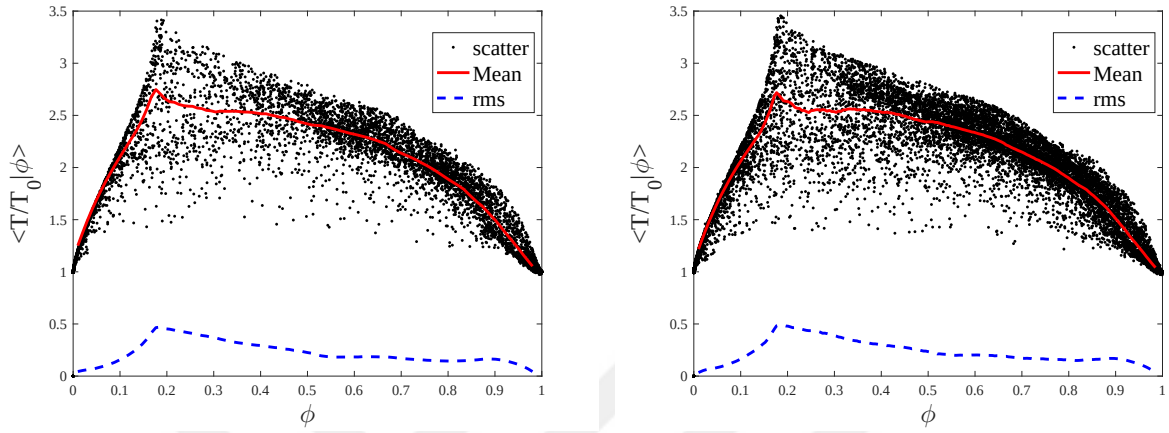


Figure 2.10: On the left the RGL EOS model and on the right the IGL EOS model predictions of $< T/T_0|\phi >$ for Re= 2500, Le $\neq$ 1, and 5 atm ambient pressure at time of 80.

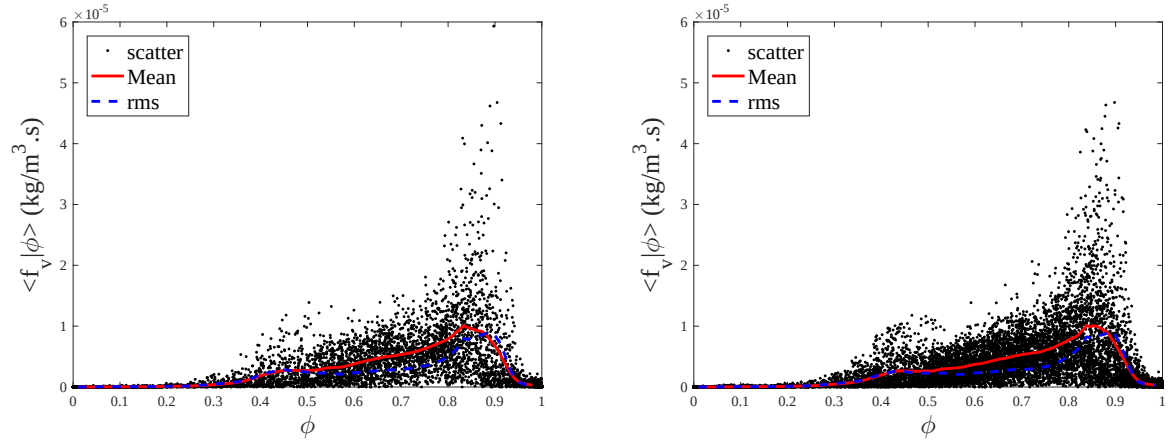


Figure 2.11: On the left the RGL EOS model and on the right the IGL EOS model predictions of$< fv|\phi >$ for Re= 2500, Le $\neq$ 1, and 5 atm ambient pressure at time of 80.

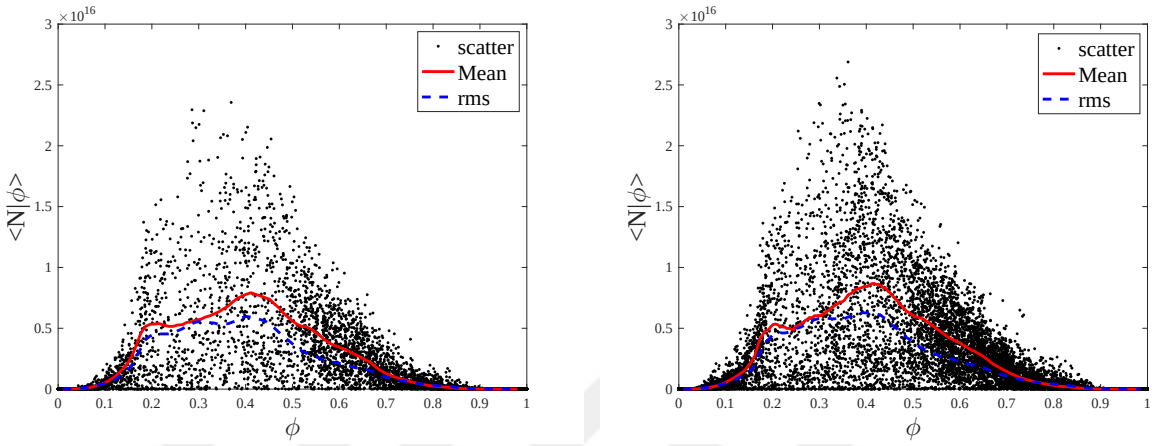


Figure 2.12: On the left the RGL EOS model and on the right the IGL EOS model predictions of $< N|\phi >$ for Re= 2500, Le $\neq$ 1, and 5 atm ambient pressure at time of 80.

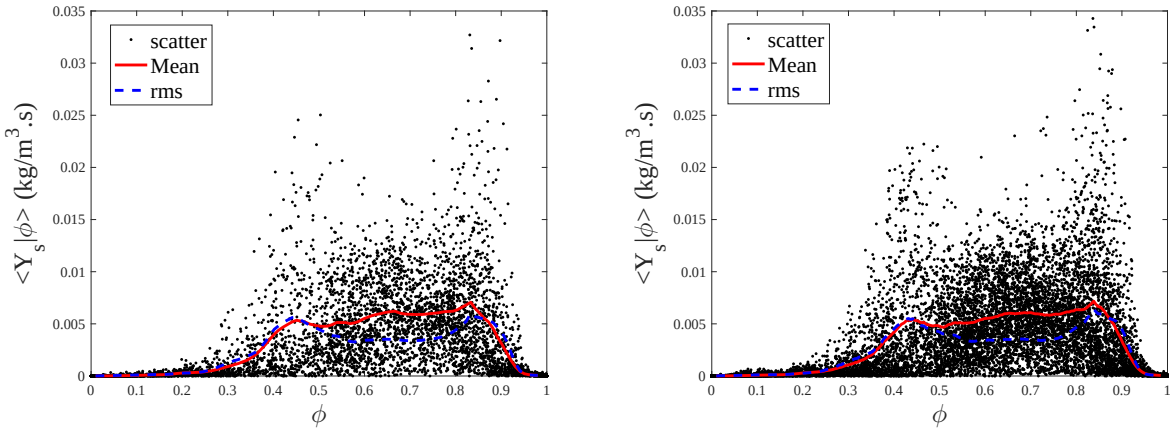


Figure 2.13: On the left the RGL EOS model and on the right the IGL EOS model predictions of $< Ys|\phi >$ for Re= 2500, Le $\neq$ 1, and 5 atm ambient pressure at time of 80.

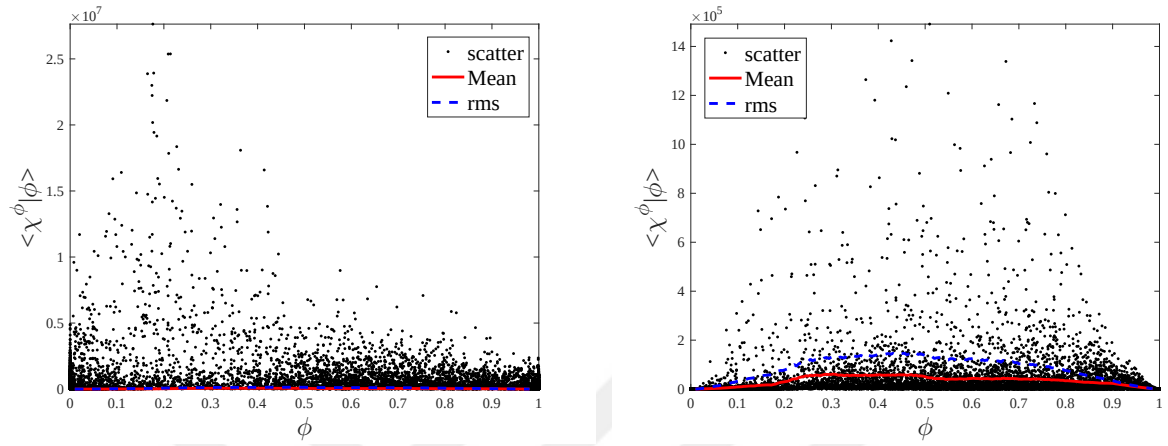


Figure 2.14: On the left the RGL EOS model and on the right the IGL EOS model predictions of $< \chi^{\phi} | \phi >$ for Re= 2500, Le $\neq$ 1, and 5 atm ambient pressure at time of 80.

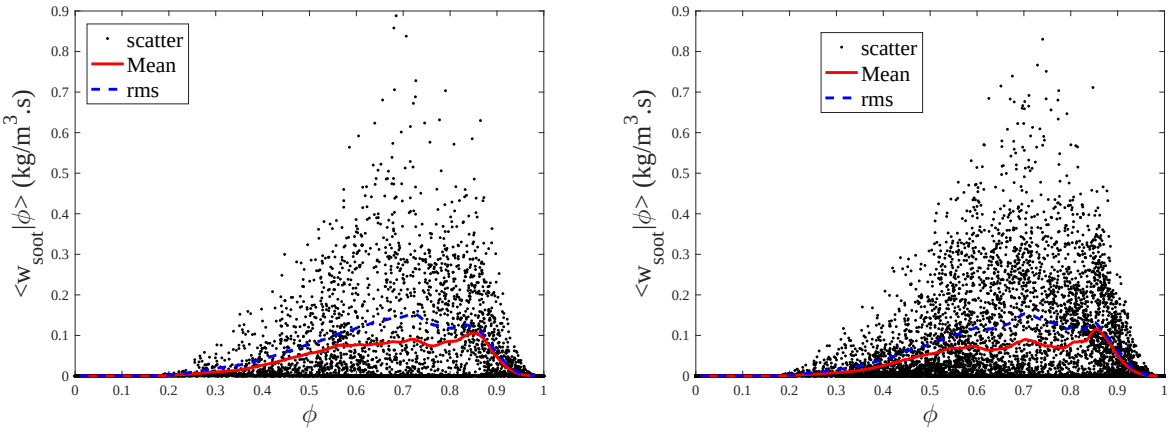


Figure 2.15: On the left the RGL EOS model and on the right the IGL EOS model predictions of $< w_{soot} | \phi >$ for Re= 2500, Le $\neq$ 1, and 5 atm ambient pressure at time of 80.

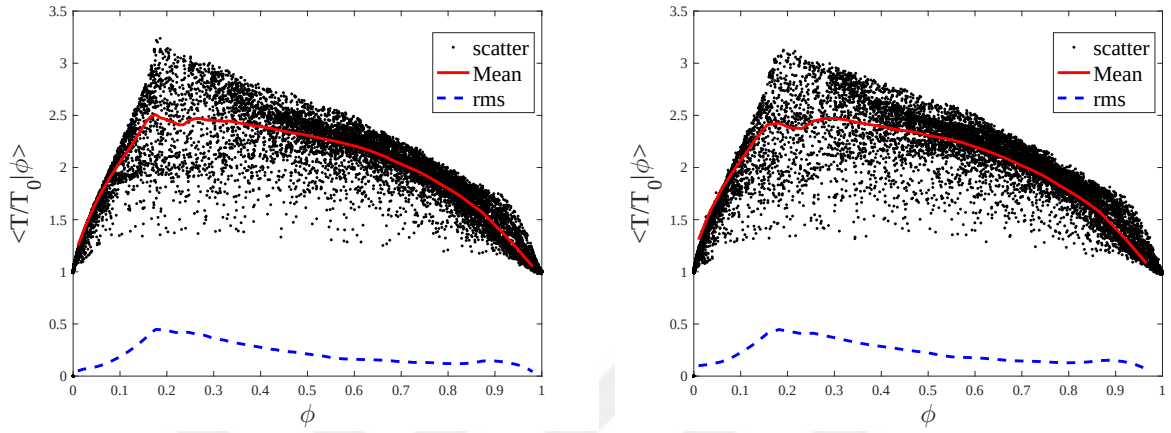


Figure 2.16: On the left the RGL EOS model and on the right the IGL EOS model predictions of $< T/T_0|\phi >$ for Re= 2500, Le $\neq$ 1, and 5 atm ambient pressure at time of 80 radiation included.

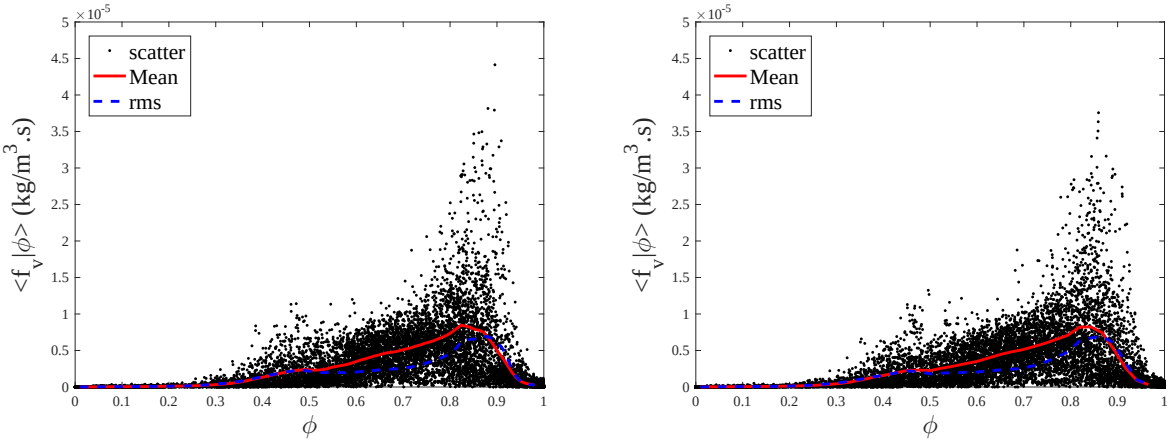


Figure 2.17: On the left the RGL EOS model and on the right the IGL EOS model predictions of$< fv|\phi >$ for Re= 2500, Le $\neq$ 1,and 5 atm ambient pressure at time of 80 radiation included.

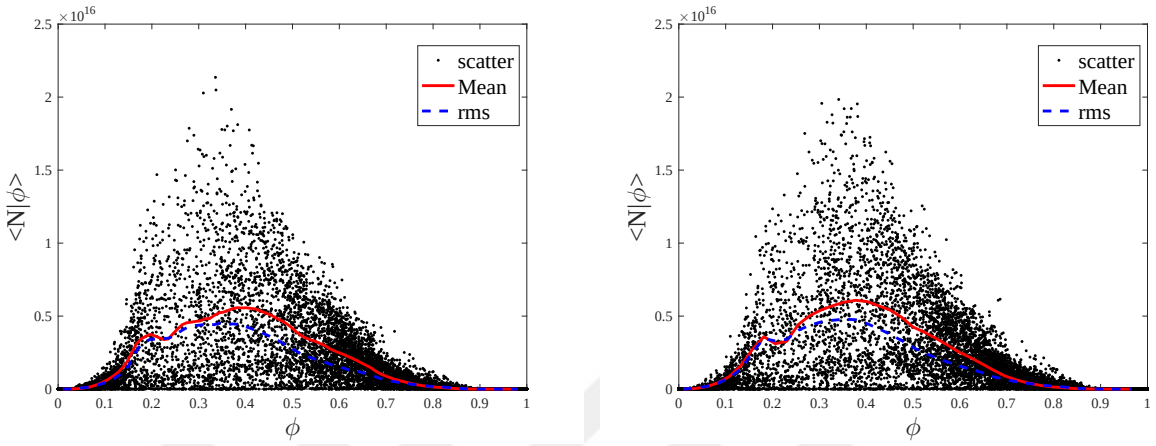


Figure 2.18: On the left the RGL EOS model and on the right the IGL EOS model predictions of $< N|\phi >$ for Re= 2500, Le $\neq$ 1, and 5 atm ambient pressure at time of 80 radiation included.

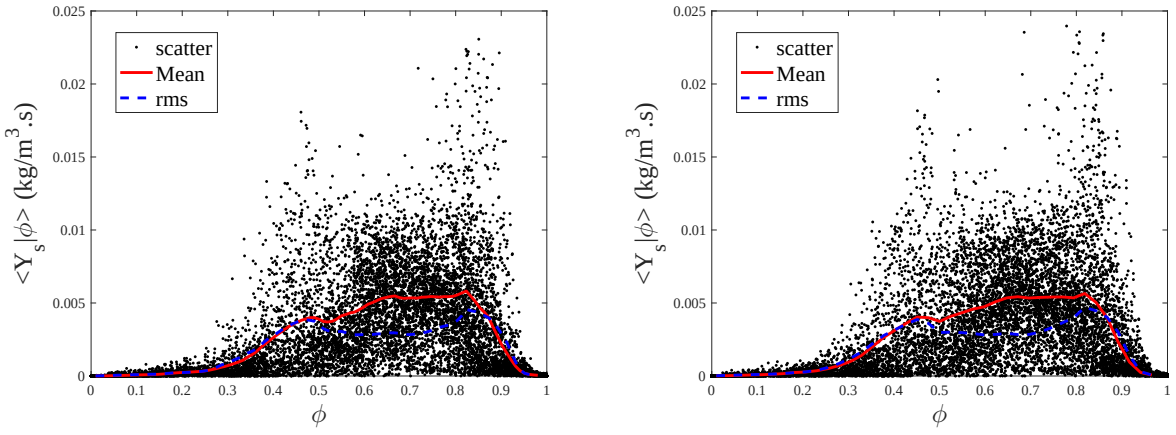


Figure 2.19: On the left the RGL EOS model and on the right the IGL EOS model predictions of $< Ys|\phi >$ for Re= 2500, Le $\neq$ 1, and 5 atm ambient pressure at time of 80 radiation included.

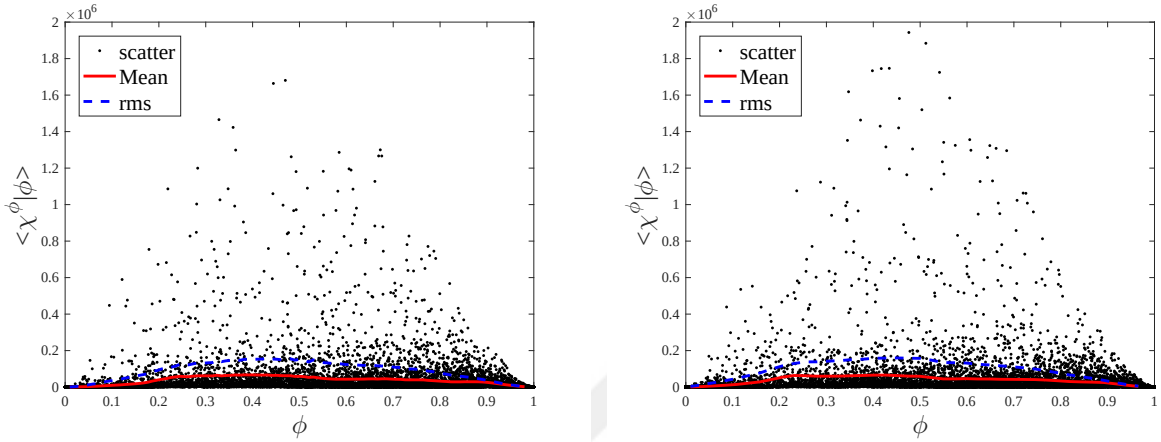


Figure 2.20: On the left the RGL EOS model and on the right the IGL EOS model predictions of $< \chi|\phi >$ for Re= 2500, Le $\neq$ 1, and 5 atm ambient pressure at time of 80 radiation included.

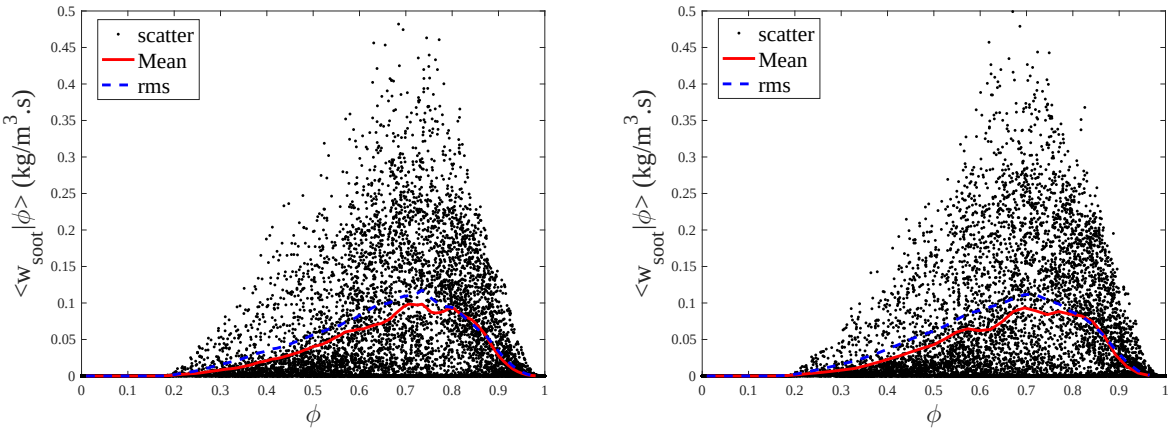


Figure 2.21: On the left the RGL EOS model and on the right the IGL EOS model predictions of$< w_{soot}|\phi >$ for Re= 2500, Le $\neq$ 1, and 5 atm ambient pressure at time of 80 radiation included.

slight increment has been observed in soot load for 10 atm flames indicating soot destruction process becomes more dominant for these flames. Figure 3.24 shows that for adiabatic flames the RGL EOS fails to predict the N profile, the addition of radiative heat loss to calculations prediction of N gets better and capture the expected behavior (i.e. temperature dominated behavior). The profiles of Y_s of adiabatic flames are shown to be well predicted by both the RGL and the IGL EOS models ([3.25]). The quantity of Y_s are seemed to be over-predicted by both models for adiabatic flames. The addition of radiative heat loss the peak value of Y_s of the RGL model is reduced by $\approx$ 30%, while there is no significant change occurs in the IGL EOS model flame ([3.31)]. In both the RGL and the IGL EOS the high levels of mixing still exist in 10 atm adiabatic flames, while the RGL EOS models fails to predicts the capture the correct trend of χ (i.e. χ is highly affected by the temperature profile), the IGL EOS model successfully capture the trend ([3.26]). By the addition of the radiation the prediction of χ of the RGL EOS model is reduced to be 22 times smaller than the adiabatic flame prediction and to adopt a gaussian-like distribution, while there is no significant change in the IGL model prediction ([3.32]). Lastly, the sot production rate prediction slightly reduced by radiative heat loss in the RGL EOS model and has an insignificant effect in the IGL EOS model ([3.27 and 3.33]).

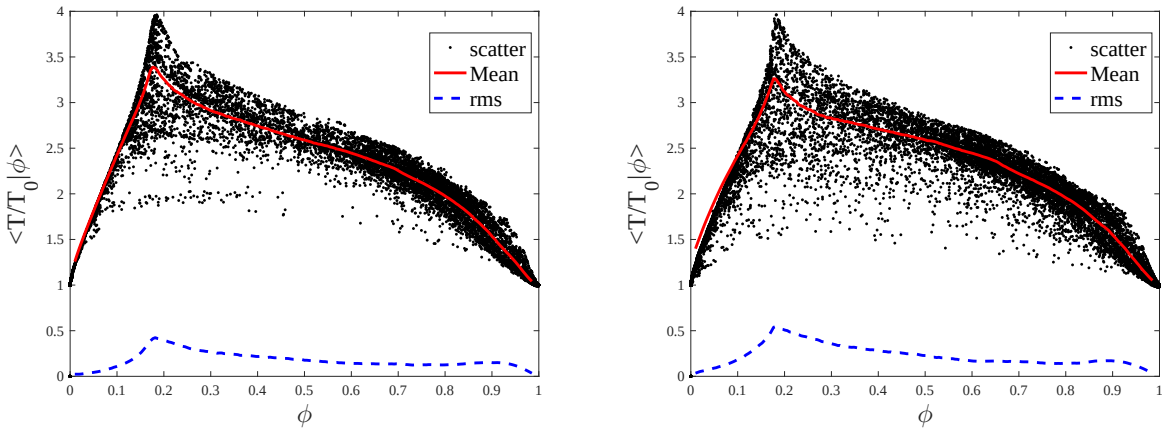


Figure 2.22: On the left the RGL EOS model and on the right the IGL EOS model predictions of $< T/T_0|\phi >$ for Re= 2500, Le $\neq$ 1, and 10 atm ambient pressure at time of 80.

Figures 3.36 through 3.42 examine the RGL and the IGL EOS effects on the soot formation/oxidation process at elevated pressure, 35 atm. As discussed earlier, with increasing pressure (i.e. increasing

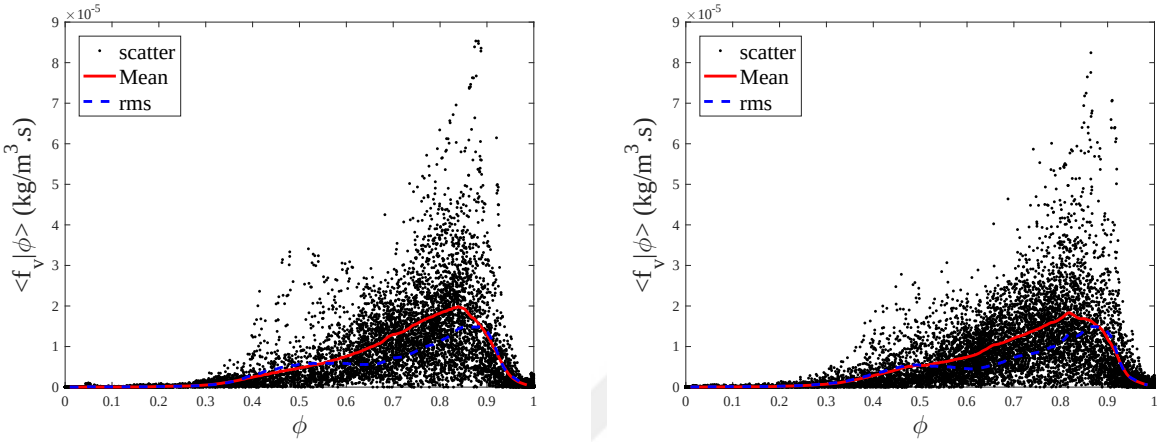


Figure 2.23: On the left the RGL EOS model and on the right the IGL EOS model predictions of$< fv|\phi >$ for Re= 2500, Le $\neq$ 1, and 10 atm ambient pressure at time of 80.

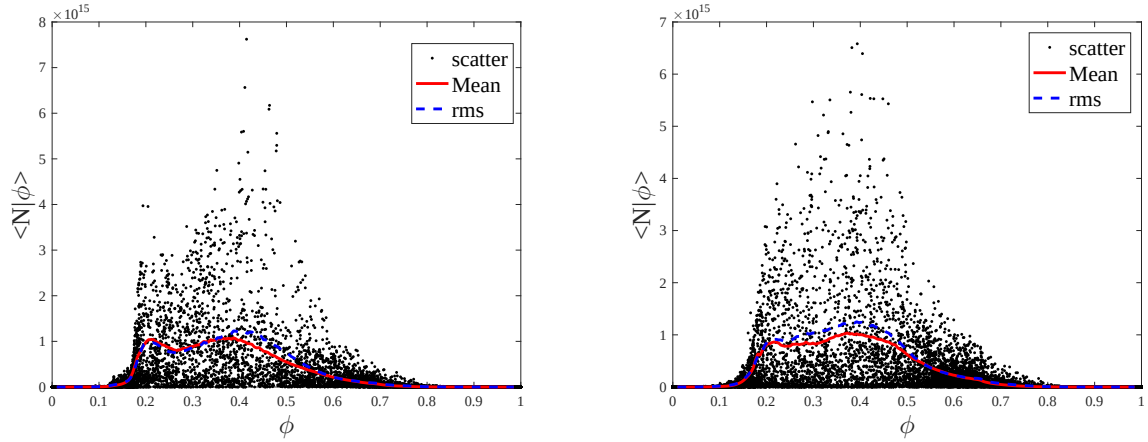


Figure 2.24: On the left the RGL EOS model and on the right the IGL EOS model predictions of $< N|\phi >$ for Re= 2500, Le $\neq$ 1, and 10 atm ambient pressure at time of 80.

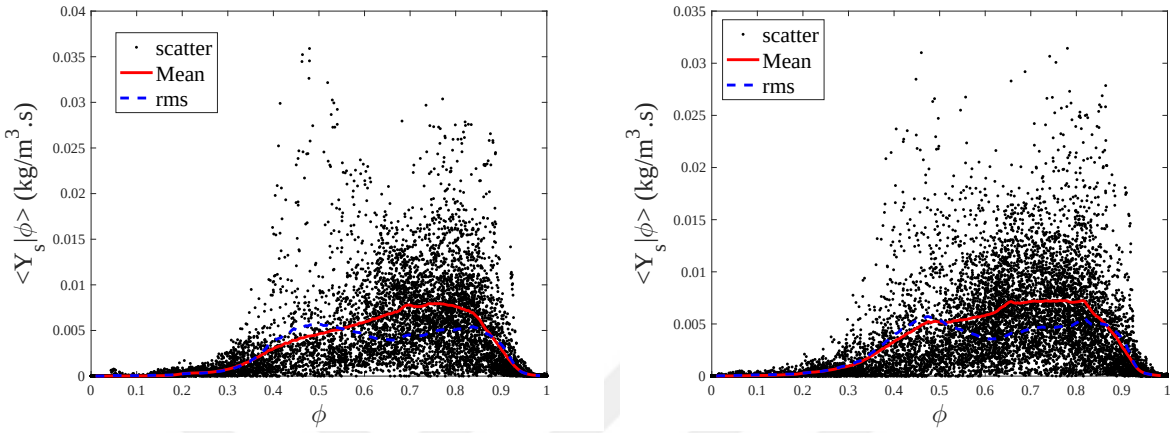


Figure 2.25: On the left the RGL EOS model and on the right the IGL EOS model predictions of $< Ys|\phi >$ for Re= 2500, Le $\neq$ 1, and 10 atm ambient pressure at time of 80.

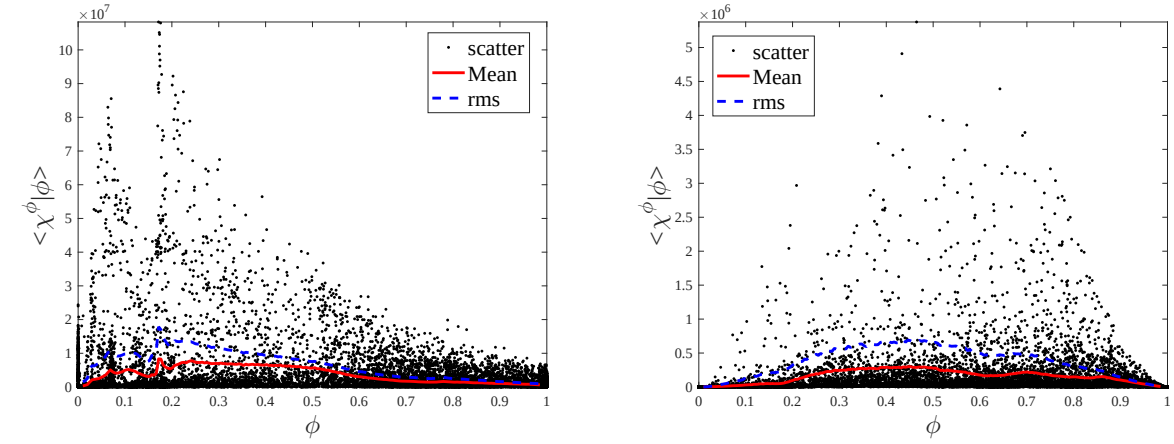


Figure 2.26: On the left the RGL EOS model and on the right the IGL EOS model predictions of $< \chi|\phi >$ for Re= 2500, Le $\neq$ 1, and 10 atm ambient pressure at time of 80.

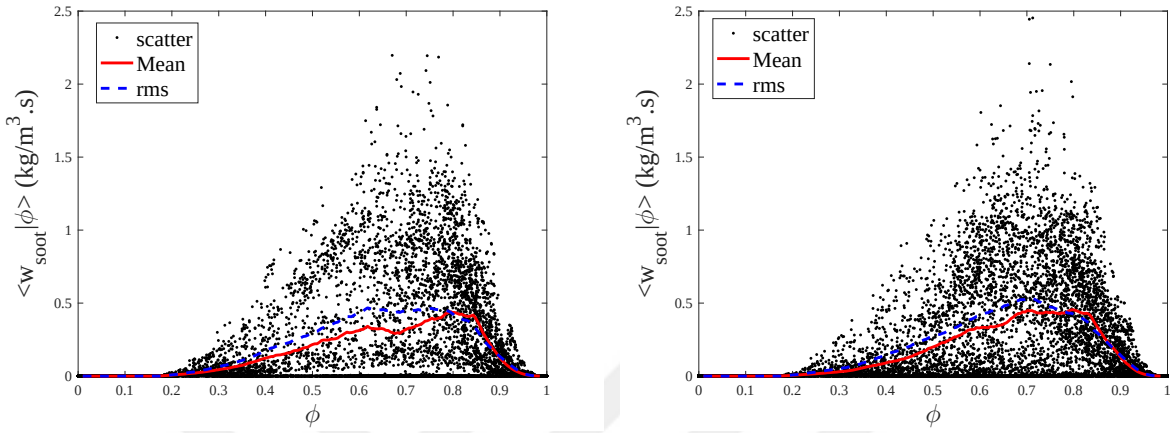


Figure 2.27: On the left the RGL EOS model and on the right the IGL EOS model predictions of $< w_{soot}|\phi >$ for Re= 2500, Le $\neq$ 1, and 10 atm ambient pressure at time of 80.

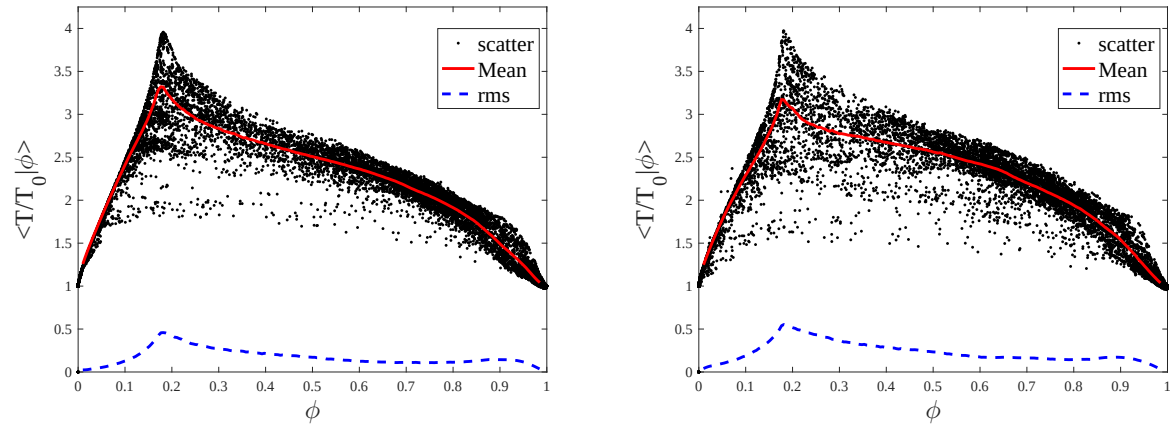


Figure 2.28: On the left the RGL EOS model and on the right the IGL EOS model predictions of $< T/T_0|\phi >$ for Re= 2500, Le $\neq$ 1, and 10 atm ambient pressure at time of 80 radiation included.

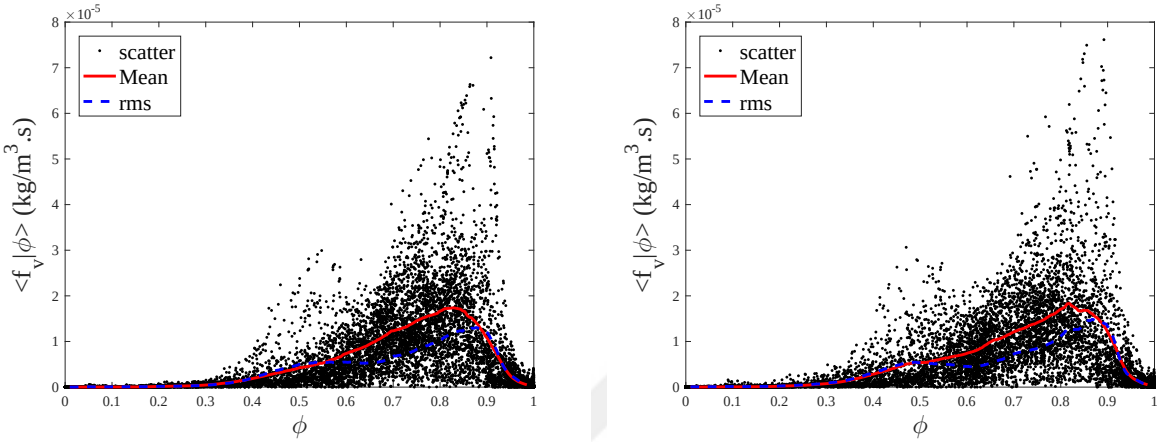


Figure 2.29: On the left the RGL EOS model and on the right the IGL EOS model predictions of$< fv|\phi >$ for Re= 2500, Le $\neq$ 1,and 10 atm ambient pressure at time of 80 radiation included.

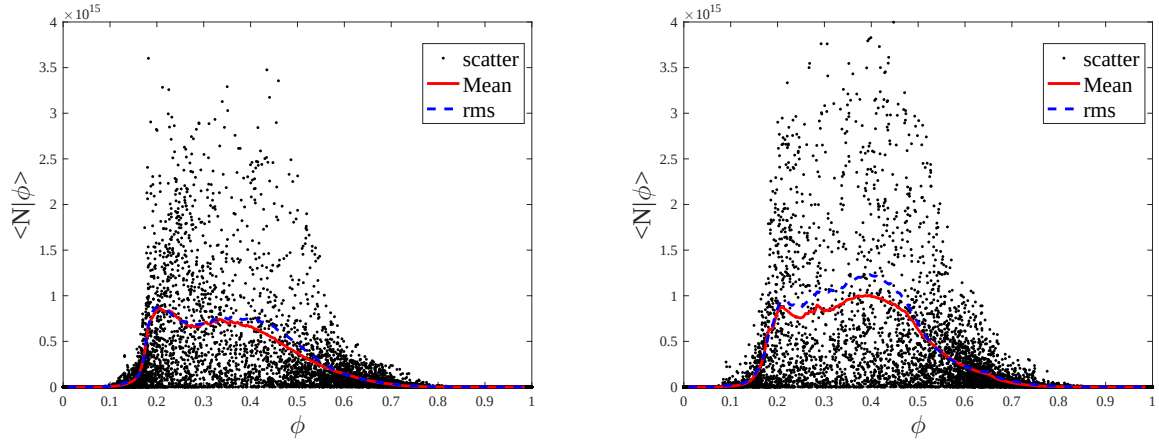


Figure 2.30: On the left the RGL EOS model and on the right the IGL EOS model predictions of $< N|\phi >$ for Re= 2500, Le $\neq$ 1, and 10 atm ambient pressure at time of 80 radiation included.

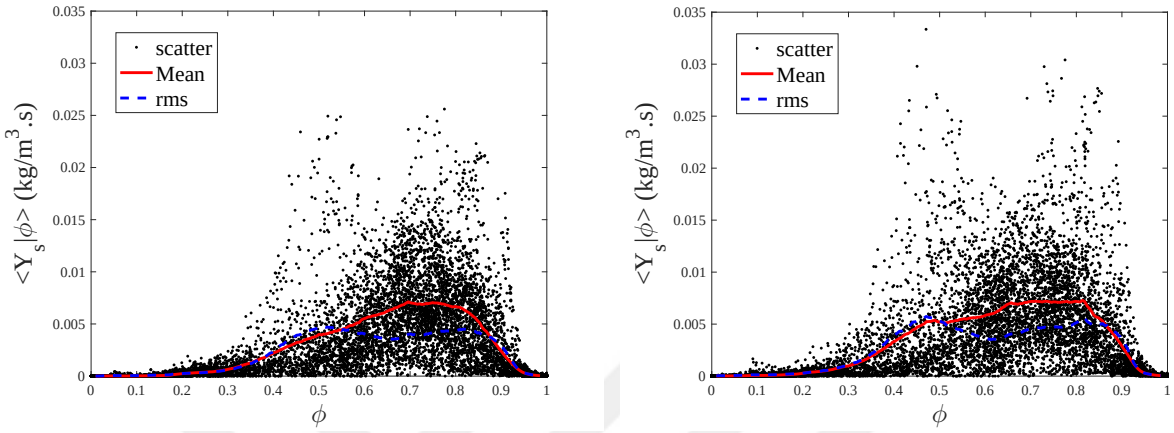


Figure 2.31: On the left the RGL EOS model and on the right the IGL EOS model predictions of $< Ys|\phi >$ for Re= 2500, Le $\neq$ 1, and 10atm ambient pressure at time of 80 radiation included.

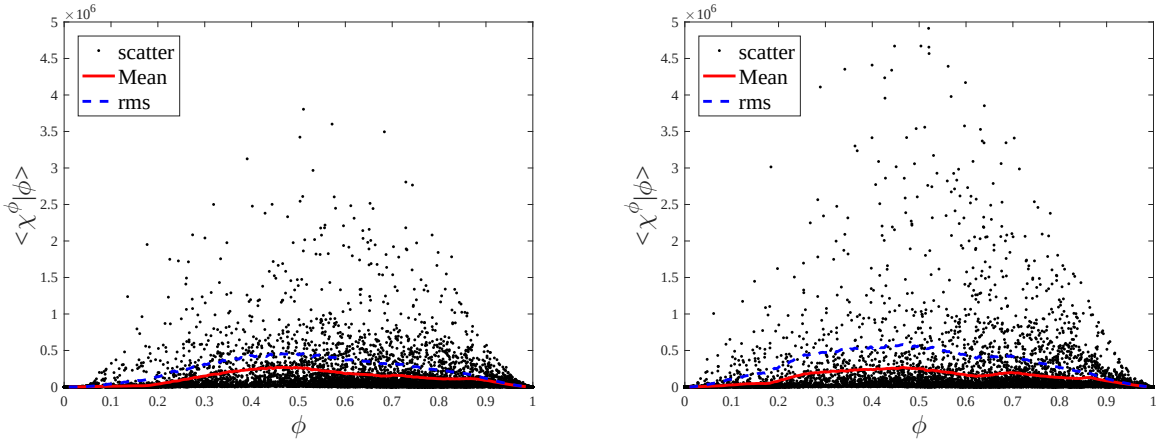


Figure 2.32: On the left the RGL EOS model and on the right the IGL EOS model predictions of $< \chi|\phi >$ for Re= 2500, Le $\neq$ 1, and 10 atm ambient pressure at time of 80 radiation included.

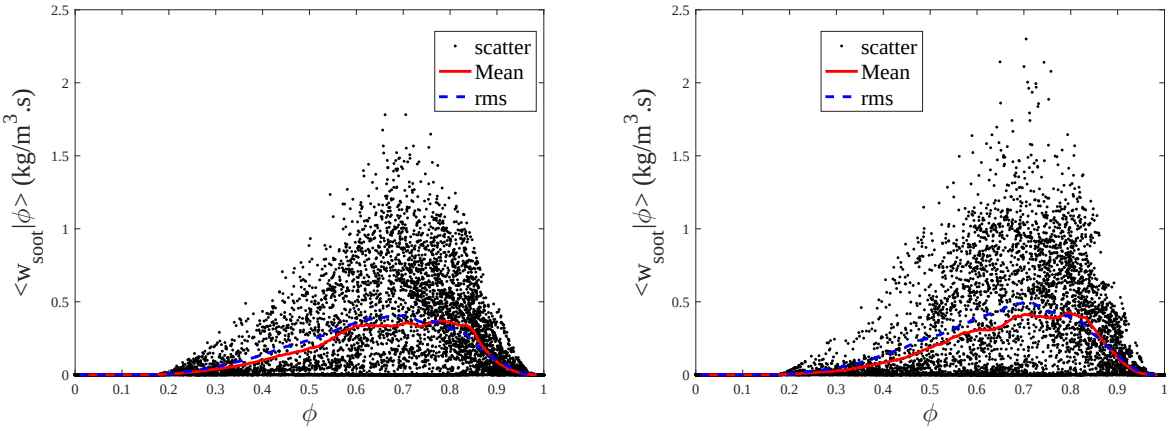


Figure 2.33: On the left the RGL EOS model and on the right the IGL EOS model predictions of $< w_{soot}|\phi >$ for Re= 2500, Le $\neq$ 1, and 10 atm ambient pressure at time of 80 radiation included.

density) fv increases. The fv quantity differences between two pressures have been observe to two order of magnitude for both the RGL and the IGL EOS cases. Furthermore, at atmospheric pressure, fv scatter plots show a denser band under the higher range of fv, while a conflict trend has been monitored for the high pressure flame (Figs. 3.2 and 3.36). As seen in Fig. 3.36 the conditioned rms and means of fv are at the same order of magnitude, while peak fv has been shifted toward to the leaner flame regions. The higher quantities of conditioned mean fv of the RGL EOS have been calculated to be in a wider part of the mixture fraction (i.e. between $\phi\approx$ 0.55 to 0.78), while in the IGL EOS case it has a narrower conditioned mean fv profile (i.e. χ ≈0.6 to 0.8). Furthermore, the IGL EOS model over-predicts fv 70% larger than the RGL EOS model. This could be related to the higher temperature prediction of the IGL EOS model (Figs. 3.34 and 3.35). The temperature difference between two cases is ≈ 530 K, which means there is a 25% of variation between two peak mean temperatures. The IGL EOS model has been predicted Ys to be 50% larger than the RGL EOS model. Similar trend of scatter plots of fv has been obtained for Ys scatter plots of elevated pressures. The IGL EOS model predicts the peak of conditioned χ to be 3 times larger than the RGL EOS model (Fig. 3.41). This difference can explain the large difference for larger fv and Ys quantities of the IGL EOS model. At elevated pressure for both cases temperature has less scattered profile in comparison with atmospheric flames even though χ^{ϕ} has been increased by the 2 and 3 order of magnitude for both the RGL and

P(atm)	EOS	$\rho(kg/m^3)$	Z (compressibility)
1	RGL	≈2.97	0.98
5	RGL	≈16.1	0.91
10	RGL	≈35.7	0.82
35	RGL	≈255	0.4
1	IGL	≈2.92	1
5	IGL	≈14.6	1
10	IGL	≈29.3	1
35	IGL	≈102	1

Table 2.7: The density and compressibility of $C_{12}H_{24}$ at 1, 5, 10 and 35 atm flames.

the IGL EOS models, respectively. This difference may be risen by the extreme density increment in the flame (the RGL EOS model has 86 times denser fuel, and, IGL EOS model 35 times denser fuel than atmospheric pressure flames Table 3.7).

The larger temperature, fv and Ys predictions lead us to over-prediction of N (i.e. the IGL EOS model calculates N 20 times larger than the RGL EOS model.). The low level of mixing in the IGL EOS case may help us to explain the higher temperature profile. The low mixing level implies a longer residence time for both the gaseous species and soot particles, and gives efficient time to increase the chemical reaction and the heat release. The large differences in temperature, Ys and fv suggest an over-prediction of w_{soot} for the IGL EOS model (Fig. 3.42). However, the suggested lower rms value of the w_{soot} by Lignell *et al.* [45] may be seen for the RGL EOS model predictions of the w_{soot}, while it is still is extremely close to the mean of the w_{soot} for the IGL EOS model. Furthermore, the w_{soot} has a narrower profile than the atmospheric pressure flame for both elevated pressure flames. Such a behavior explains the trends of fv and Ys observed in the previous figures.

Figures 3.43 - 3.48 are significant to show the evaluation of the RGL EOS flame at 35 atm. At time of 80, the flame temperature exhibit a slight reduction while becoming more scattered through mixture fraction axis ([3.43]) (i.e. more turbulent flow). Figure 3.44 show a 25% increment in fv, while it has been carried to the fuel rich region by the flow. N, at time of 80, now has two more distinct peaks located at $\phi \approx 0.25- \approx 0.45$ ([3.45]). As the time evalutes, Y_s becomes more scattered in agreement with the more scattered temperature profile ([3.46]). Figure 3.47 and 3.48 also support more turbulent

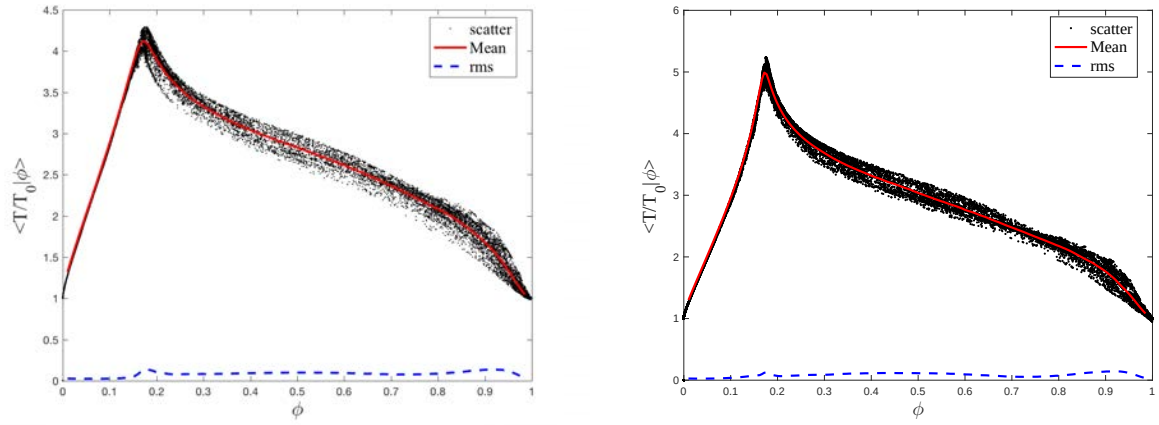


Figure 2.34: On the left the RGL EOS model and on the right the IGL EOS model predictions of $< T/T_0|\phi >$ for Re= 2500, Le $\neq$ 1, and 35 atm ambient pressure at time of 70.

flame and has a larger standard deviation for χ and Y_s at the region where we observe more scattered temperature profile.

Lastly, in this chapter we have investigated pressure effects on the soot formation/destruction processes in adiabatic flames in Figs. 3.50 - 3.54 only for 2D data at the non-dimensional time of 80. Increasing ambient pressure results with increasing flame temperature for both the RGL and the IGL EOS model flames. For first three flames the IGL EOS model well predicts the flame temperature while it highly over predicts the flame temperature. It deviates by $\approx$ 25% fror the peak flame temperature as stated before which will cause the over-prediction of the soot properties. Figure 3.50 represents the log-normal of fv for four different pressures of the RGL and the IGL EOS models. This figure has two important trends to be considered. Firstly, it clearly shows that increasing the ambient pressure of flame has a positive effect on fv in all the flames. Secondly, the IGL EOS model under-predicts the fv in the first 3 flames of 1, 5 and 10 atm, while it over-predicts the fv of 35 atm flame. The difference of atmospheric and 35 atm fv predictions for the IGL EOS models is an order of magnitude larger than the RGL EOS model predictions' s difference. Figure 3.51 shows the pressure and the RGL and the IGL EOS assumption effects on Ys predictions. This figure exhibits similar behavior with fv and N predictions, and it clearly states that the IGL EOS model over-predicts the Ys by $\approx$ 40 % in the flame at 35 atm. The destruction of the soot particles produces species of CO and H (i.e. from Table 3.1

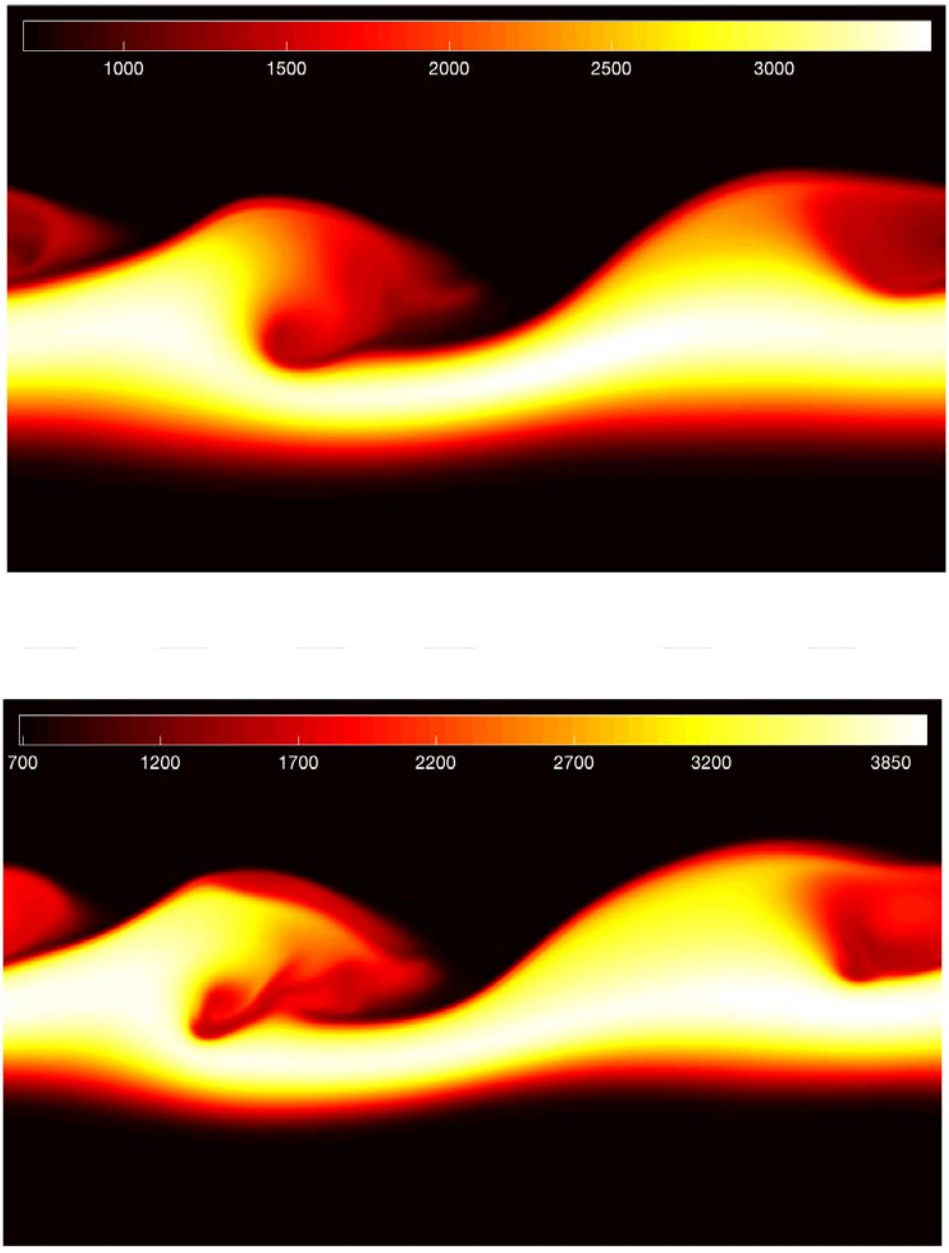


Figure 2.35: Contour plots of T(K) for pressure 35 atm, Le≠1 and Re=2500, top is the RGL model and bottom is the IGL EOS model predictions time of 65, 3D data.

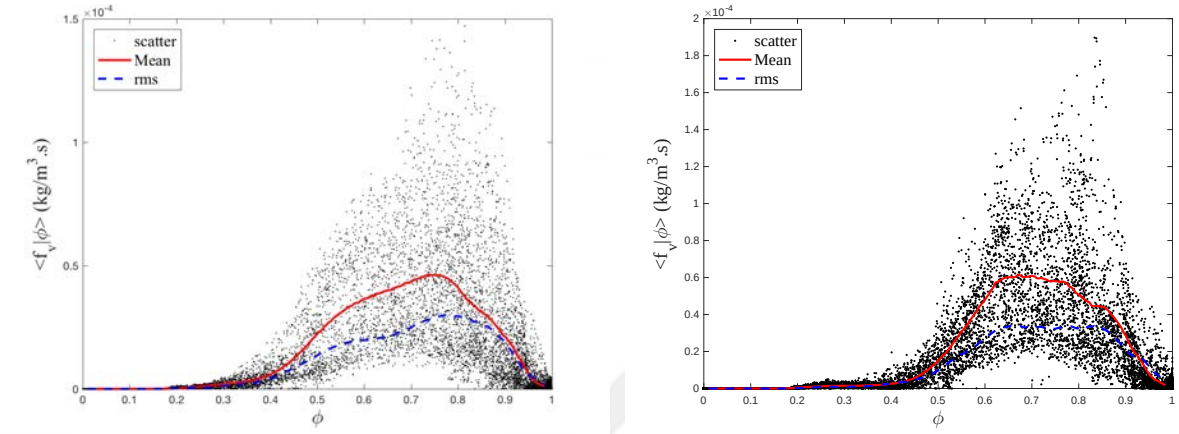


Figure 2.36: On the left the RGL EOS model and on the right the IGL EOS model predictions of $< fv|\phi >$ for Re= 2500, Le $\neq$ 1, and 35 atm ambient pressure at time of 65.

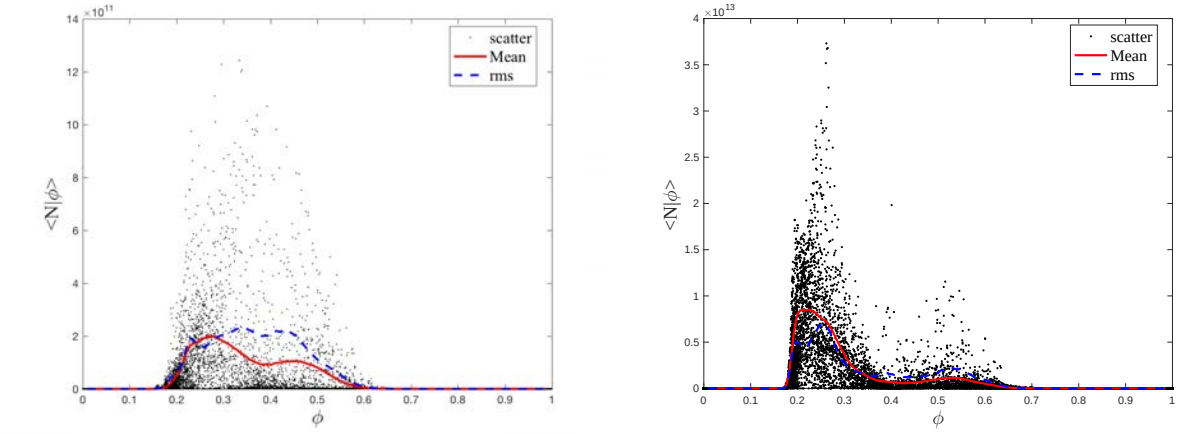


Figure 2.37: On the left the RGL EOS model and on the right the IGL EOS model predictions of $< N|\phi >$ for Re= 2500, Le $\neq$ 1, and 35 atm ambient pressure at time of 65.

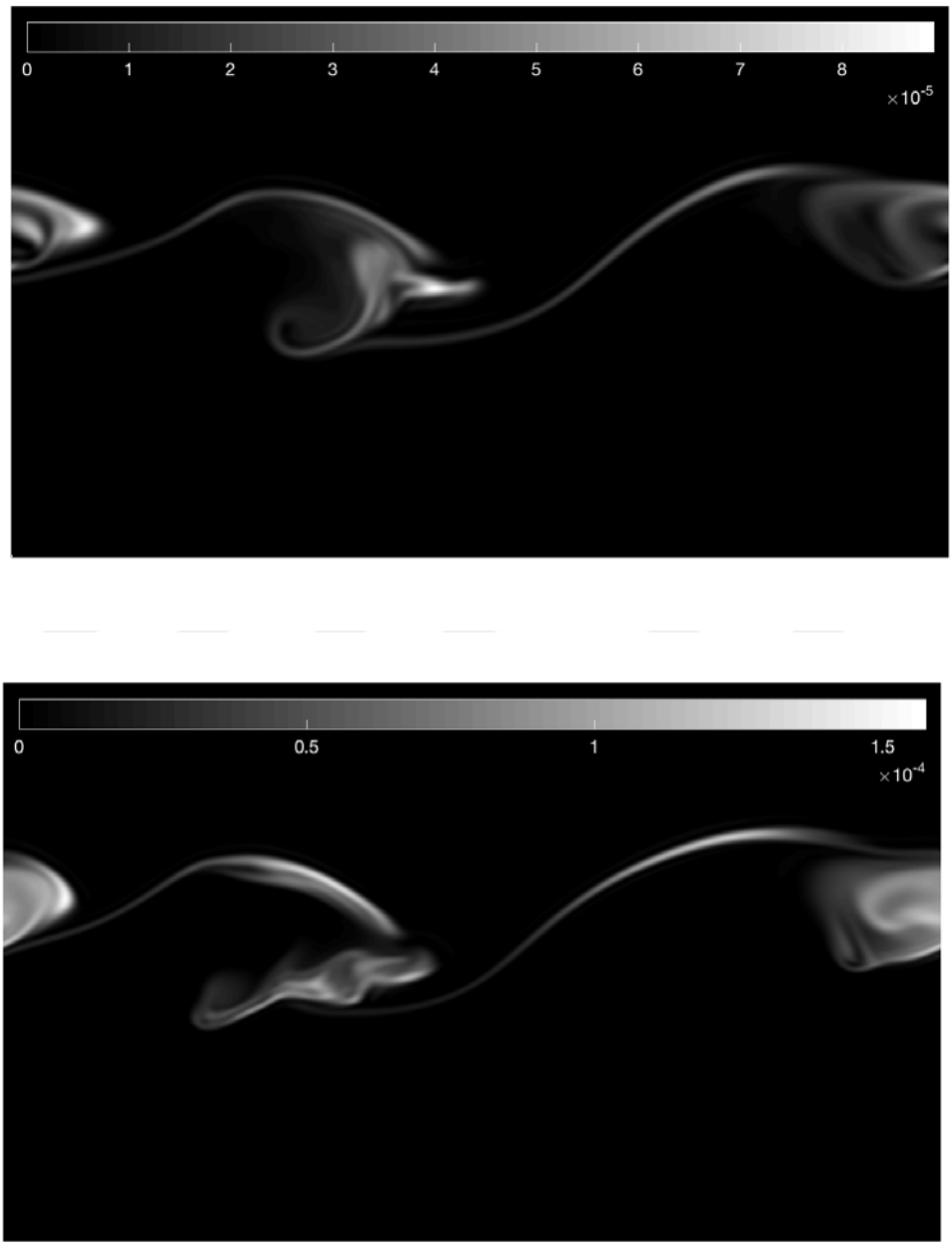


Figure 2.38: Contour plots of fv for pressure 35 atm, Le≠1 and Re=2500, top is the RGL model and bottom is the IGL EOS model predictions time of 65, 3D data.

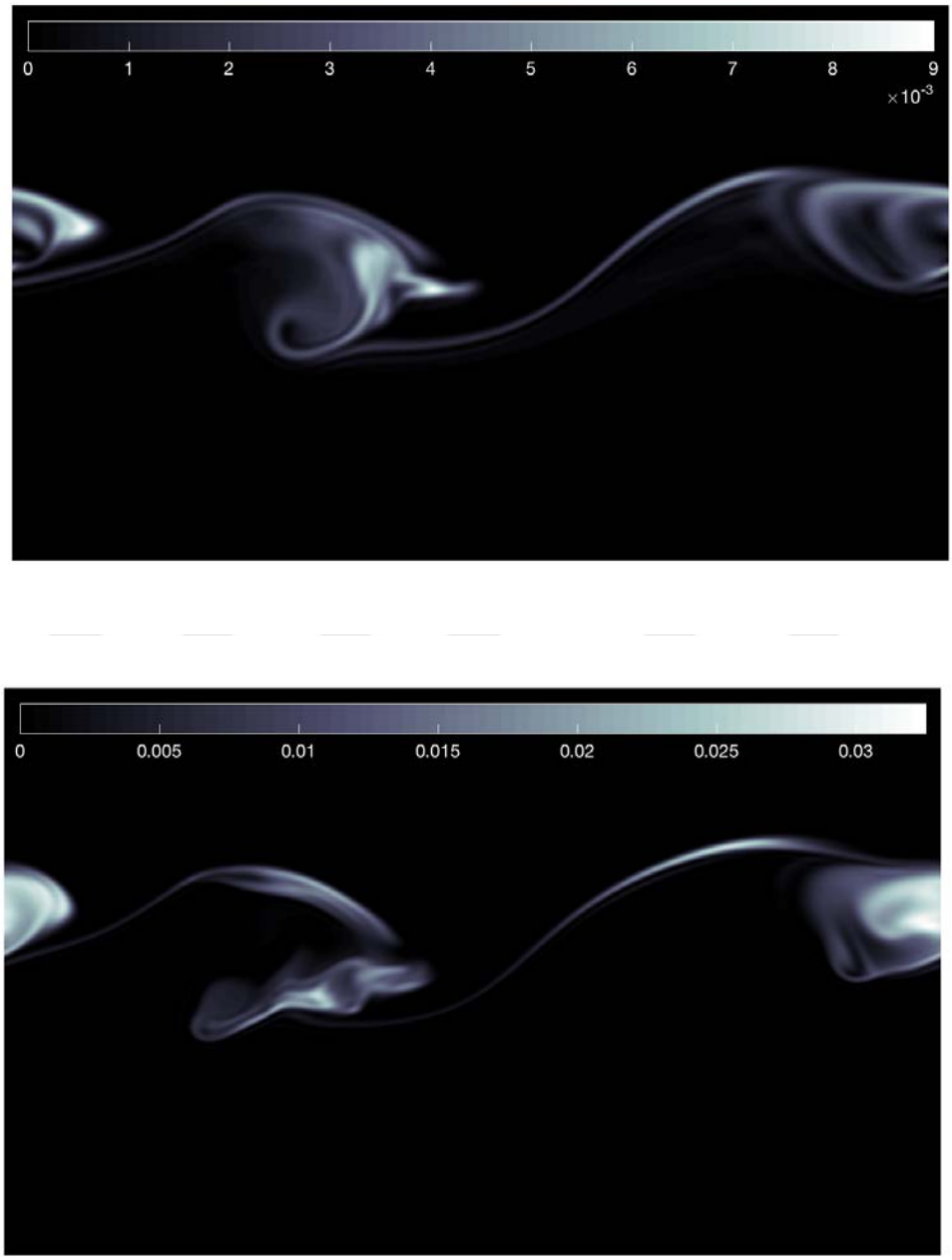


Figure 2.39: Contour plots of Ys for pressure 35 atm, Le≠1 and Re=2500, top is the RGL model and bottom is the IGL EOS model predictions time of 65, 3D data.

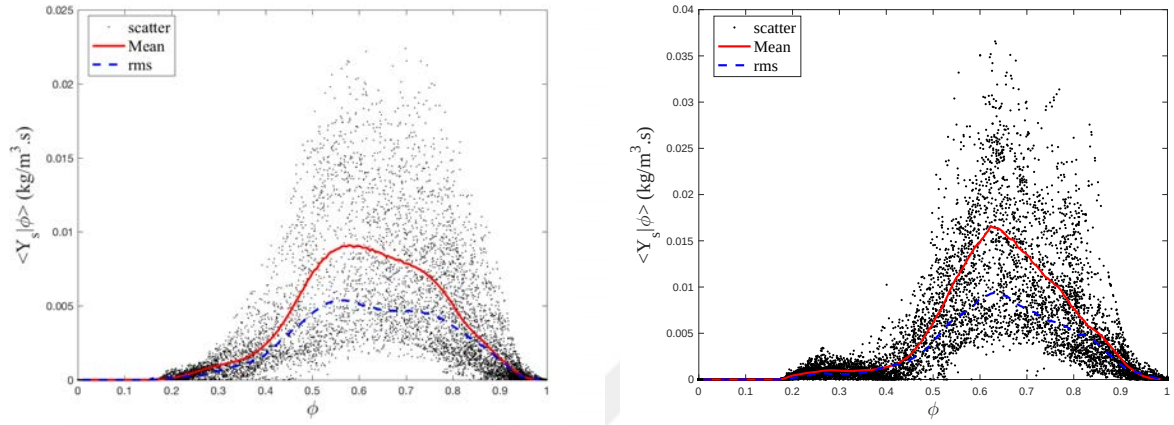


Figure 2.40: On the left the RGL EOS model and on the right the IGL EOS model predictions of $< Ys|\phi >$ for Re= 2500, Le $\neq$ 1, and 35 atm ambient pressure at time of 65.

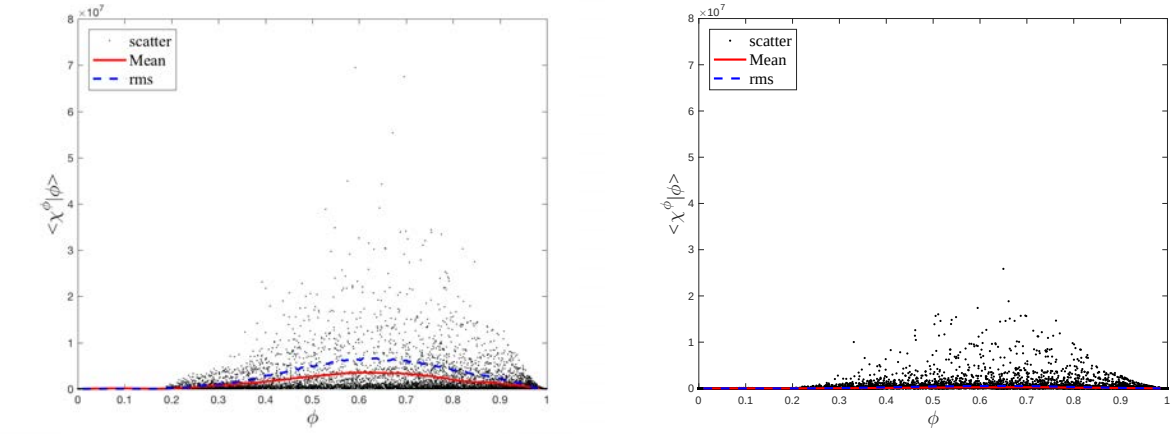


Figure 2.41: On the left the RGL EOS model and on the right the IGL EOS model predictions of $< \chi|\phi >$ for Re= 2500, Le $\neq$ 1, and 35 atm ambient pressure at time of 65.

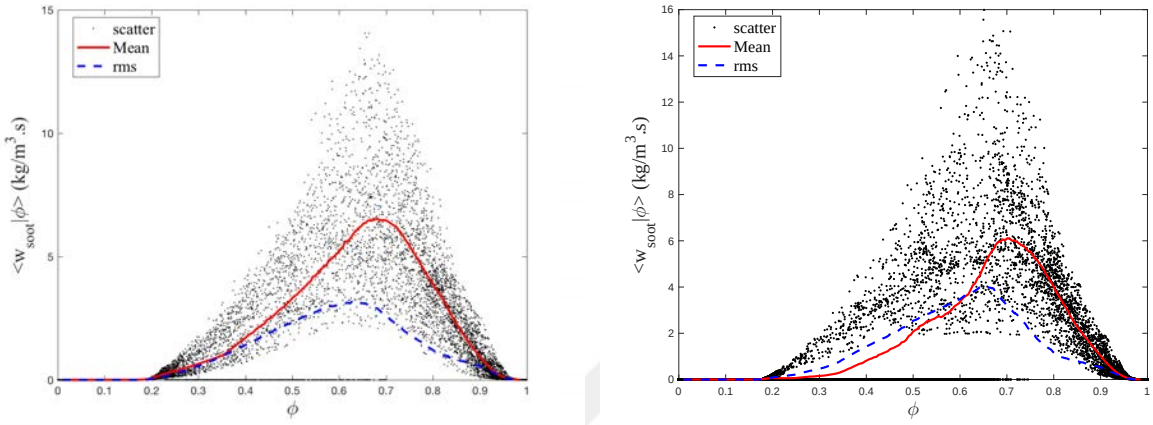


Figure 2.42: On the left the RGL EOS model and on the right the IGL EOS model predictions of $< w_{soot}|\phi >$ for Re= 2500, Le $\neq$ 1, and 35 atm ambient pressure at time of 65.

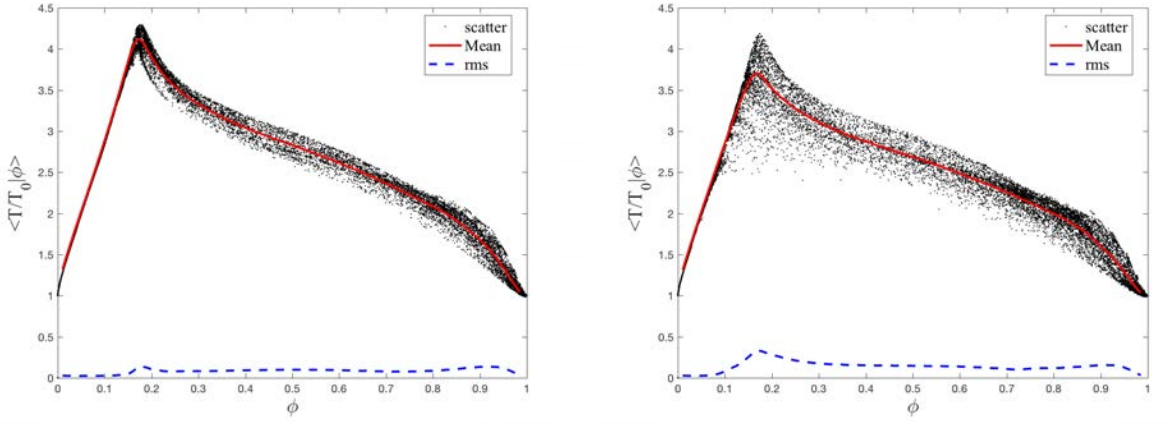


Figure 2.43: The comparison of RGL EOS model of $< T/T_0|\phi >$ for Re= 2500, Le $\neq$ 1, and 35 atm ambient pressure at time of 65 and 80.

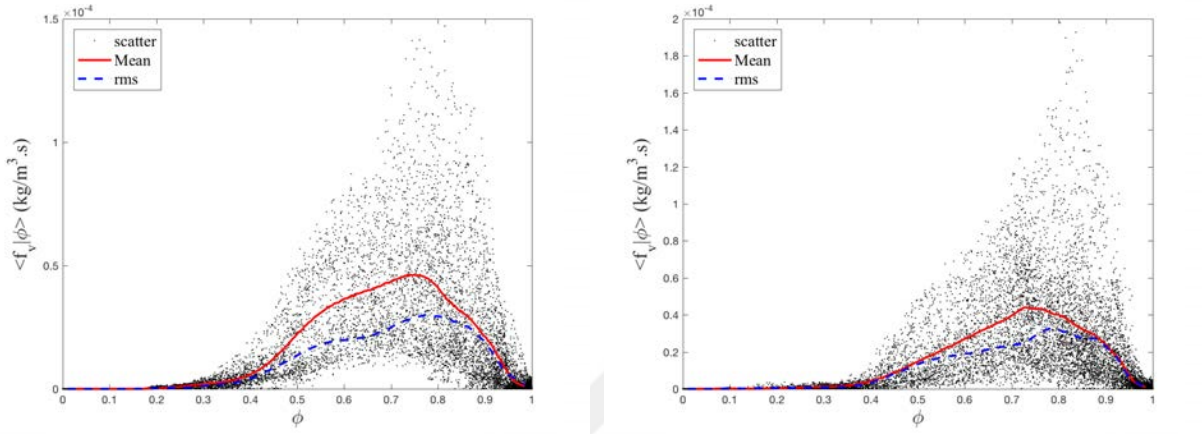


Figure 2.44: The comparison the RGL EOS model predictions of $< fv|\phi >$ for Re= 2500, Le $\neq$ 1, and 35 atm ambient pressure at time of 65 and 80.

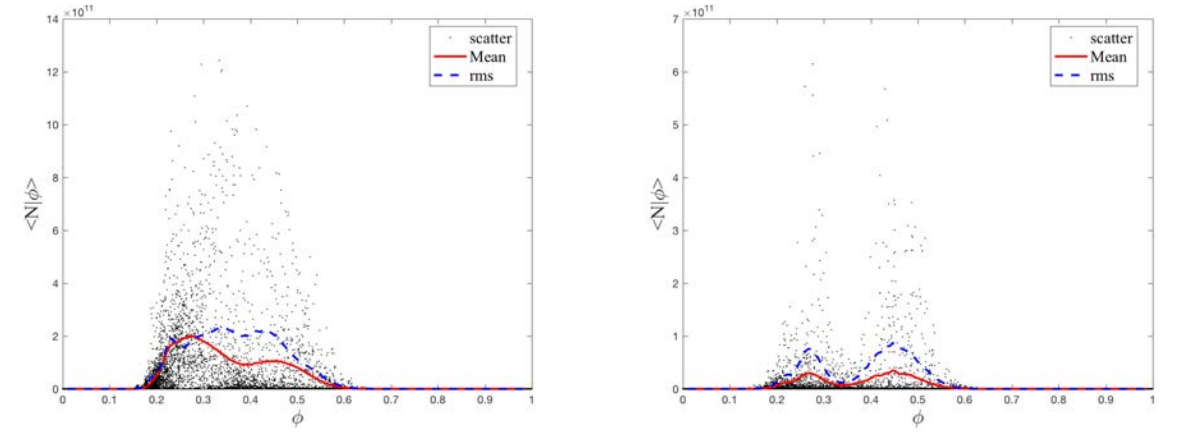


Figure 2.45: The comparison the RGL EOS model predictions of $< N|\phi >$ for Re= 2500, Le $\neq$ 1, and 35 atm ambient pressure at time of 65 and 80.

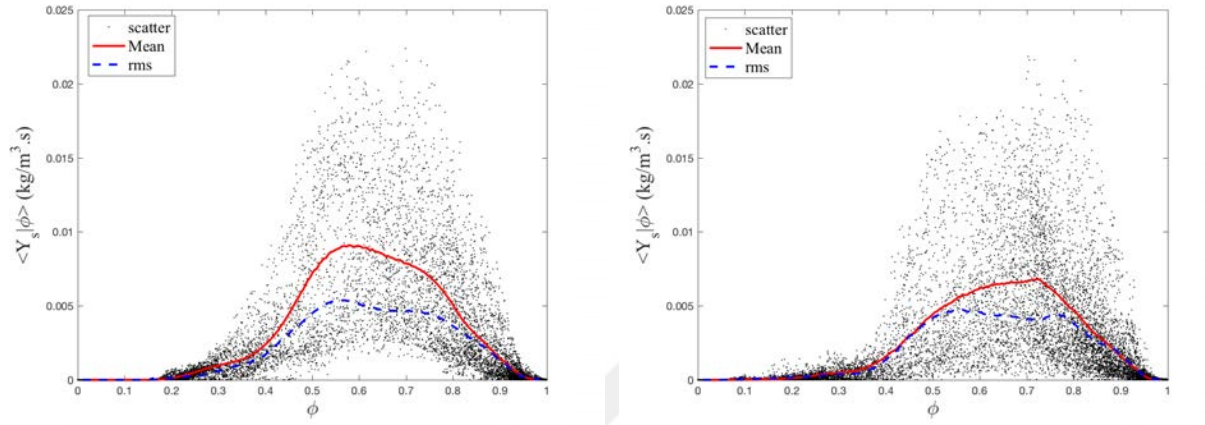


Figure 2.46: The comparison the RGL EOS model predictions of $< Ys|\phi >$ for Re= 2500, Le $\neq$ 1, and 35 atm ambient pressure at time of 65 and 80.

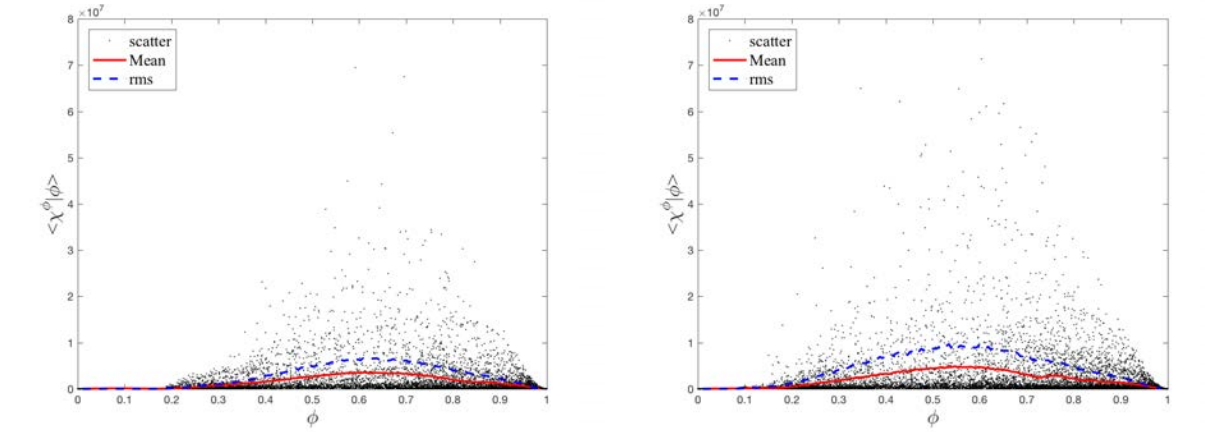


Figure 2.47: The comparison the RGL EOS model predictions of $< \chi|\phi >$ for Re= 2500, Le $\neq$ 1, and 35 atm ambient pressure at time of 65 and 80.

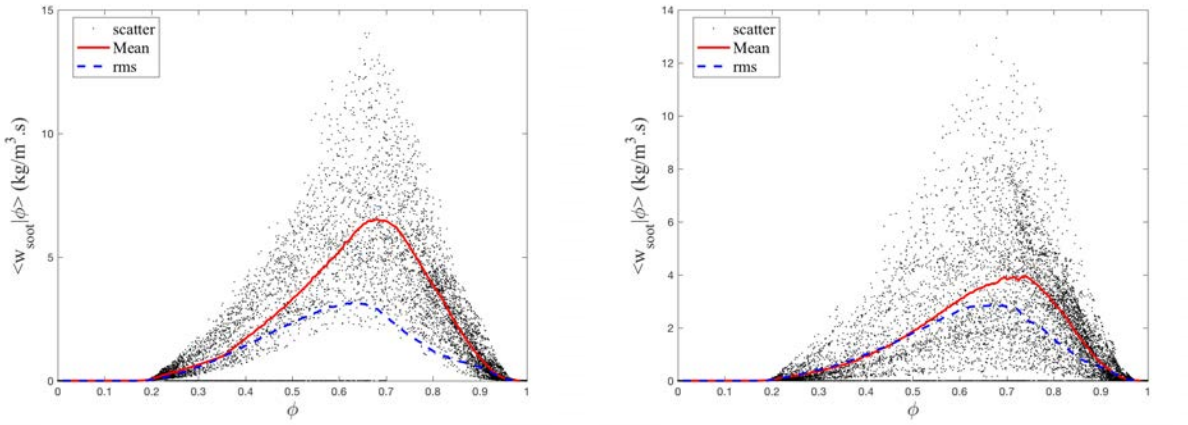


Figure 2.48: The comparison the RGL EOS model predictions of $< w_{soot}|\phi >$ for Re= 2500, Le $\neq$ 1, and 35 atm ambient pressure at time of 65 and 80.

$C_s + 0.5O_2 \rightarrow CO$ and $C_s + OH = CO + H$). CO and H mass fractions **??** and **??** mass fractions are over-predicted for the elevated pressure (i.e. 35 atm) flame. While the peak mass fraction of CO is over-predicted by $\approx$ 28% and for species H it is $\approx$ 35%. Finally, Fig. 3.54 presents the mass fractions of OH radical in the flames. This figure has importance to explain the flame characteristics since OH mass fraction is considered to be highly effective on flame temperatures. As mentioned earlier, the temperature profile of 35 atm for the IGL EOS model has a more scattered behavior than the RGL EOS model's temperature profile. The OH mass fraction is $\approx$ 45 % under-predicted in the region we observe extinction in the IGL EOS model temperature profile. Furthermore, for 5 and 10 atm flames the IGL EOS model predict the OH mass fractions profiles to be very similar to each other, which can explain why the Ys, fv and N predictions have similar quantities in the IGL EOS model. Even though the IGL EOS model is capable of catching the profile of the soot properties for low operating pressures and high pressure flames, it fails when the pressure reaches the critical point. The employment of the RGL EOS model is crucial to predict the soot properties and transportation as well as the flame characteristics in adiabatic $Kerosene/Air$ flame simulations approriately.

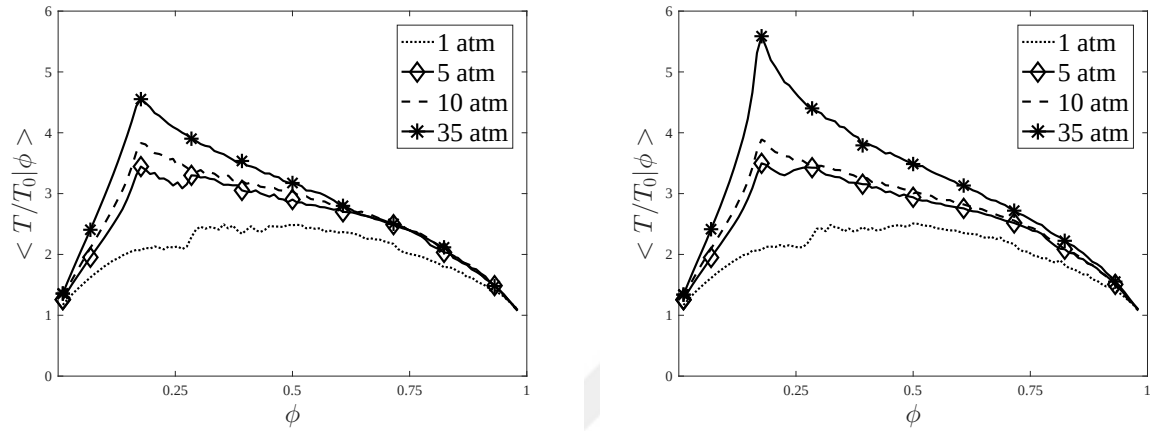


Figure 2.49: The RGL and the IGL EOS pressure effects on mean variables Re=2500, left is RGL and right is IGL time of 80 2D data

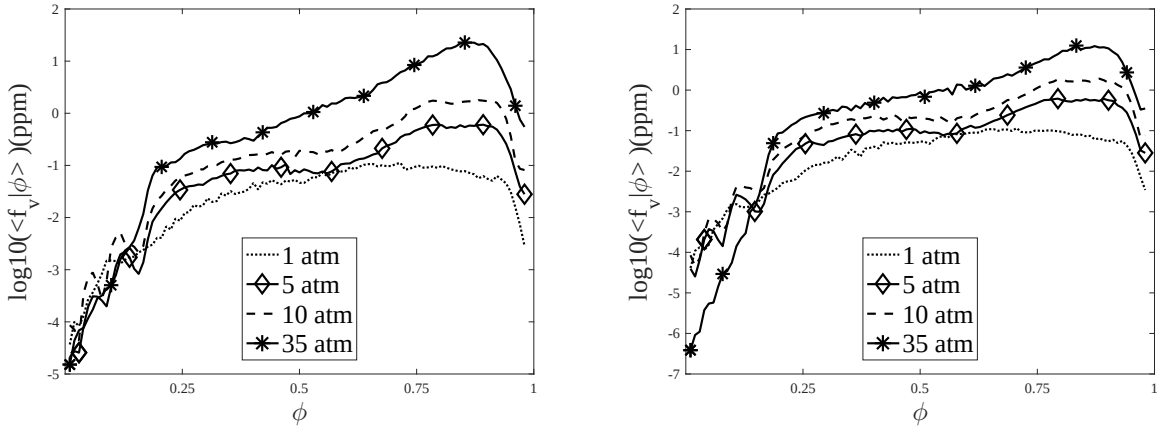


Figure 2.50: Pressure effects on means of $< fv|\phi >$ for Re=2500, Le≠1 and 1 atm on the left the RGL model predictions and on the right the IGL model predictions time of 80 2D data

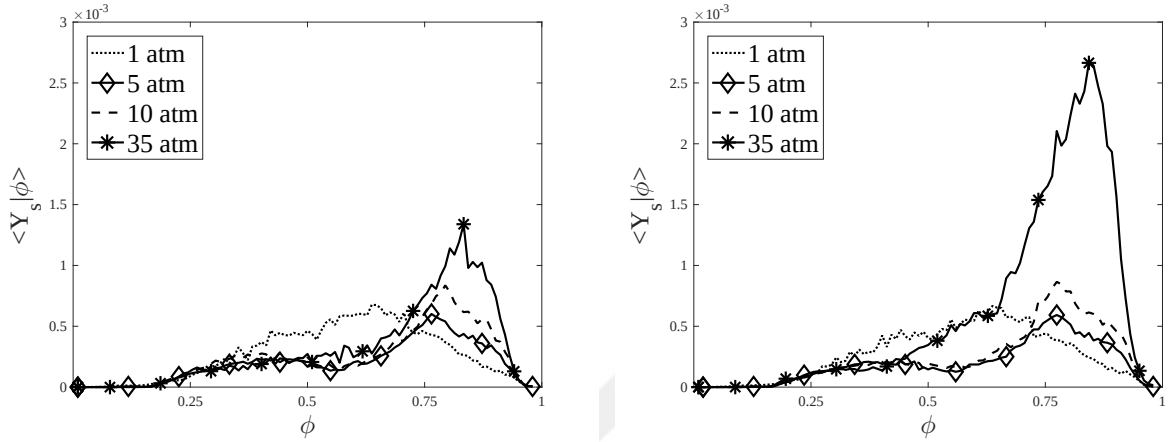


Figure 2.51: Pressure effects on means of $< Ys|\phi >$ for Re=2500, Le≠1 and 1 atm, on the left the RGL model predictions and on the right the IGL model predictions time of 80 2D data

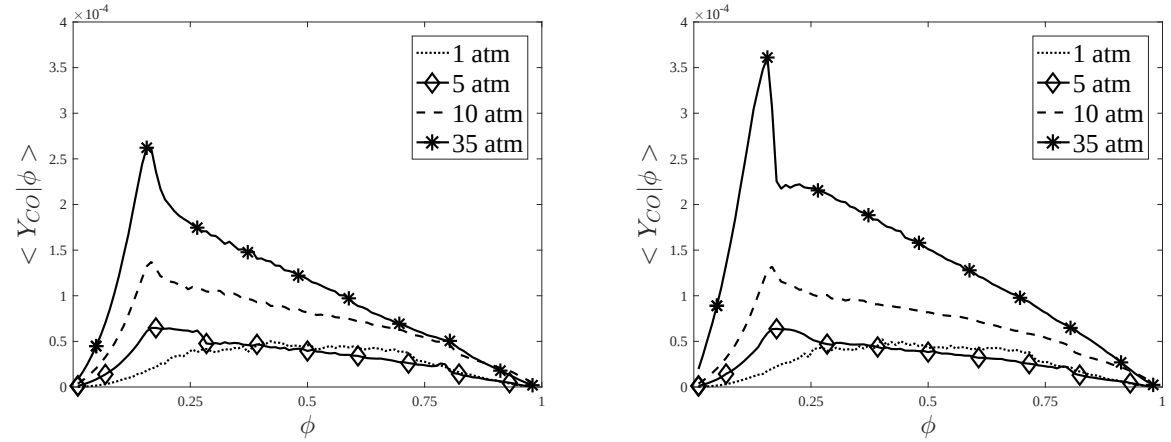


Figure 2.52: The RGL and the IGL EOS pressure effects on mean variables Re=2500, left is RGL and right is IGL time of 80 2D data

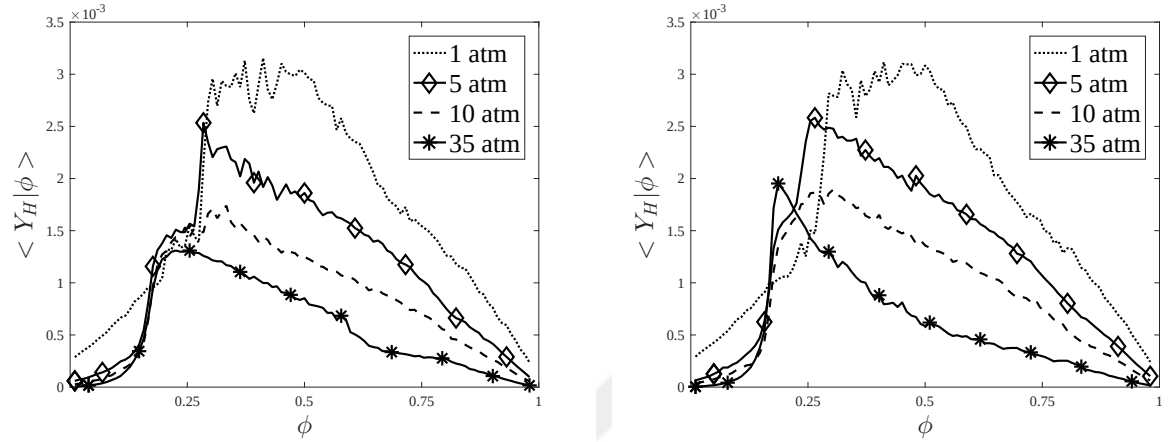


Figure 2.53: The RGL and the IGL EOS pressure effects on mean variables Re=2500, left is RGL and right is IGL time of 80 2D data

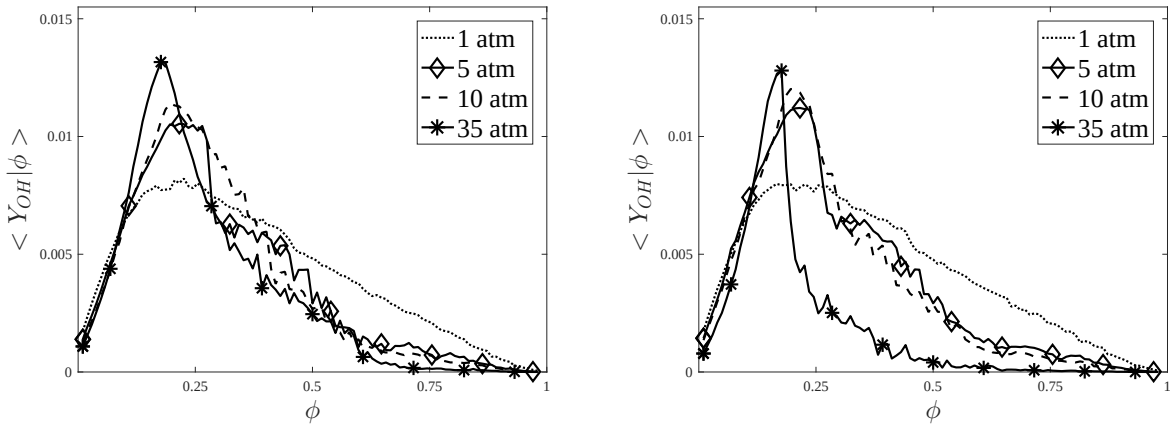


Figure 2.54: Pressure effects on mean of $< Y_{OH}|\phi >$ for Re=2500, Le≠1 and 1 atm, on the left the RGL model predictions and on the right the IGL model predictions time of 80 2D data

Chapter 3

Differential Diffusion and Equation of State Effects on Soot Production/Oxidation Process in Kerosene/Air Shear Flames

3.1 Introduction

Despite of intensive ongoing researches on developing new methods to predict soot formation, oxidation and transportation processes in turbulent flames, the literature suffers from lack of an adequate approach to this phenomenon. This usually emanates from assumptions of equal molecular diffusion of gaseous species (i.e. equal Schmidt #s) and simply equating thermal diffusivity to mass diffusivity (i.e. unity Lewis #) [63]. The large and small scales of turbulence become detached with increasing Re # (i.e. intense turbulence) leading insignificant effects of differential diffusion which is associated with small scales (i.e. large Peclet # and heat release) [40, 63]. In turbulent flames with extreme heat release, the effect of turbulent mixing becomes ineffective even in large scales [40, 54, 56, 63, 82].

The effects of differential diffusion in turbulent flames have been investigated in experiments by Refs. [4, 19, 54, 56, 82]. Bergmann *et al.* have pointed out the significance of differential diffusion effects in turbulent $CH_4/H_2/N_2$ jet diffusion flames with Re= $15,200$. Drake *et al.* [19] have shown

that differential diffusion due to the preferential diffusion of H_2 becomes insignificant in H_2/Air flames by increasing Re #.Effects of differential diffusion on large scales have been observed by Smith *et al.* [82] in a CO_2 diluted H_2 flames at Re= $30,000$. In a similar CO_2 diluted H_2 flame Masri *et al.* [54] have reported that differential diffusion becomes insignificant at Re$\approx 60,000$. For different $H_2/N_2 - Air$ jet flames for the range Re= $6,200$ and 8,800 Meier *et al.* [56] have noted that differential diffusion to be extremely important on temperature. The reader should note that based on aforementioned studies for the flames at low and intermediate Re #s differential diffusion must be taken into account for proper prediction of the flame.

Typically soot particles' diffusion time scale is considerable larger than the gas species resulting the soot particles to be governed by varied turbulent scales which causes soot particles to be transported throughout the flame diverting the local flame characteristics [52]. It is known that lighter species (i.e. H and H_2) are remarkably effected by the differential diffusion [47, 52, 55, 73]. The diffusion of H and H_2 reshape the soot particle bundles where the soot formation and soot surface growth occur in the presence of H and soot precursors [52]. The differential diffusion has a role to draw H toward to C_2H_2 and causing soot formation and growth processes to happen [52].

For the conditional moment closure (CMC) and Reynolds Average Navier-Stokes (RANS) models, scalar dissipation rate has an eminent role to define relation between scalar mixing and combustion modeling [52, 74]. It is also affected by Le # since it is the ratio of the thermal diffusivity to the mass diffusivity [52]. As stated in earlier paragraphs it is generally assumed that the turbulent mixing is the dominant power which governs species mass diffusivity eliminating the differential diffusion effects. This statement generally leads researchers to make the unity Le # assumption [52]. The transportation of radicals, such as O, OH and H, from flame kernel to the soot formation area is a very important phenomenon in the soot formation and growth processes [52].

The following section of this chapter an analysis of a generated DNS database of both atmospheric and high pressure $Kerosene/Air$ reacting shear flames. The same reduced chemical mechanism including soot formation and oxidation processes has been coupled with ideal gas law and the unit Le # assumption to test the validity of these assumptions under realistic thermodynamic combustion

regime.

The DNS data is calculated by solving the governing equations for 3D, temporally developing, non-premixed reacting shear layers of $C_{12}H_{24}/Air$. Details of the computational domain, mesh and numerical scheme used can be found in Ref. [23]. The mixing occurs at the center of the domain. For the current work, 10 distinct reacting simulations are considered for $Re_F = 2500$. The convective Mach # is set to be 0.35. 8 of the simulations have been conducted for 2D DNS (Table 4.1), and 2 of the 10 simulations have been conducted for 3D DNS (Table 4.3). The heat and mass flux equations have been used with the non-unity Le # assumption [Eqs. (2.7) and (2.8)] are reduced to the simplest forms to be used with the unity Le # assumption. While Eqs. (4.1) and (4.2) are the heat flux of Fourier's law, and mass flux of Fickian' s law, respectively, Eq. (4.3) is the IGL EOS:

$$Q_j = -\kappa \frac{\partial T}{\partial x_j}, \qquad (3.1) \qquad J'_{j,k} = -D \frac{\partial X_\alpha}{\partial x_j}, \qquad (3.2) \qquad P = \rho \frac{R_m}{M_m} T, \qquad (3.3)$$

where κ is the thermal conductivity, D is the diffusion coefficient, X_α is the mol fraction of the species α, R_m is the gas constant of the mixture, and M_m is the molecular weight of the mixture. For all cases the initial temperature is $T_0 = 700K$, and the ambient pressure varies between 1 and 35 atm (i.e. 1, 5, 10, and 35 atm).

3.2 Objectives

Based on the above, the primary objective of this chapter is to examine the effects of the unity Le # assumption on the processes in both atmospheric and elevated pressure flames for both a RGL and the IGL EOS models.

In the current work, a semi-global soot production/oxidation of $Kerosene/Air$ turbulent flames have been investigated for atmospheric and elevated pressures for unity Le # assumption by employing a RGL and the IGL EOS model. The results of atmospheric pressure flames have been compared with the data obtained in the current work with non-unity Le # assumption of the RGL and the IGL EOS

Run	Oxidizer	P_0(atm)	EOS	Le	$T_0(K)$	Re_0	$N_1 \times N_2$	t_f^*	Radiation
1	Air	1	RG	1	700	2500	400×608	80	No
2	Air	1	IG	1	700	2500	304×698	80	No
3	Air	5	RG	1	700	2500	304×544	80	No
4	Air	5	IG	1	700	2500	304×544	80	No
5	Air	10	RG	1	700	2500	280×480	80	No
6	Air	10	IG	1	700	2500	280×480	80	No
7	Air	35	RG	1	700	2500	240×640	80	No
8	Air	35	IG	1	700	2500	240×640	80	No

Table 3.1: Summary of simulation parameters from all cases considered. P_0 is initial pressure, T_0 is the initial temperature, Re_0 the initial Reynolds #, N_1, N_2, are the # of grid points in the x_1, x_2 direction, respectively, and t_f^* is non-dimensionalized final simulation time.

Run	Oxidizer	$P_0(atm)$	EOS	Le	$T_0(K)$	Re_0	$N_1 \times N_2 \times N_3$	t_f^*	Radiation
1	Air	1	IG	1	700	2500	$400 \times 672 \times 280$	80	No
2	Air	1	IG	1	700	2500	$400 \times 640 \times 300$	80	No

Table 3.2: Summary of simulation parameters from all cases considered. P_0 is initial pressure, T_0 is the initial temperature, Re_0 the initial Reynolds #, N_1, N_2 and N_3, are the # of grid points in the x_1, x_2, and x_3, direction respectively, and t_f^* is non-dimensionalized final simulation time.

models. The results are represented in Section 4.3. We start by comparing the unity Le # assumption of the RGL and the IGL EOS models' results of time of 65 with the RGL and the IGL EOS results of time of 65 for atmospheric and 1 atm ambient pressures with Re=2500 and Ma # (=0.35). Continued with comparing the unity Le # assumption results of the RGL and the IGL EOS models. Later, Le #s are calculated for 1, 5 ,10 and 35 atm flames at time of 65 for both the RGL and the IGL EOS models. Lastly, the effect of the widely used unity Le # assumption and pressure effects on soot production/oxidation processes are examined.

3.3 Results

Only 1 atm flames results of the RGL and the IGL EOS models of this chapter have been obtained with 3D DNS calculations; the rest of the results were obtained with 2D DNS calculations due to the computational limitations. Much deeper investigation is need to be done for future investigation of

pressure and Le # effects associated with both a RGL and the IGL EOS for high pressure flames.

We start with comparing the non-unity Le # assumption results of adiabatic 1 atm flames that have been analyzed in the previous chapter with the unity Le # assumption predictions of the RGL and the IGL EOS model flames. For both non-unity and unity Le # prediction comparisons are made for the time of 65. Figures 4.1 - 4.9 compare the predictions of the RGL EOS model coupled with non-unity and unity Le # assumptions. Figure 4.1 exposes how the temperature distribution is effected by unity Le # assumption. The peak flame temperature is reduced by 25% by switching from the non-unity Le # assumptions to unity Le assumption. The flame packets extinct in the region of $\phi \approx 0.1$ to $\phi \approx 0.3$ resulting having low mean flame temperature profile. The top sub-figure of the Fig. 4.2 represents the contour plot of the RGL EOS model with non-unity Le # assumption and bottom one has been created with the same EOS model coupled with Le=1. It is clearly seen that a continuous hot flame packet existed in the top bottom affirming the left sub-figure of Fig. 4.1. The other point we should pay attention is the how the flame structure has been modified by the unity Le # assumption. Now the flame possesses an intensified turbulent profile signifying that high levels of mixing is existed in this flame.

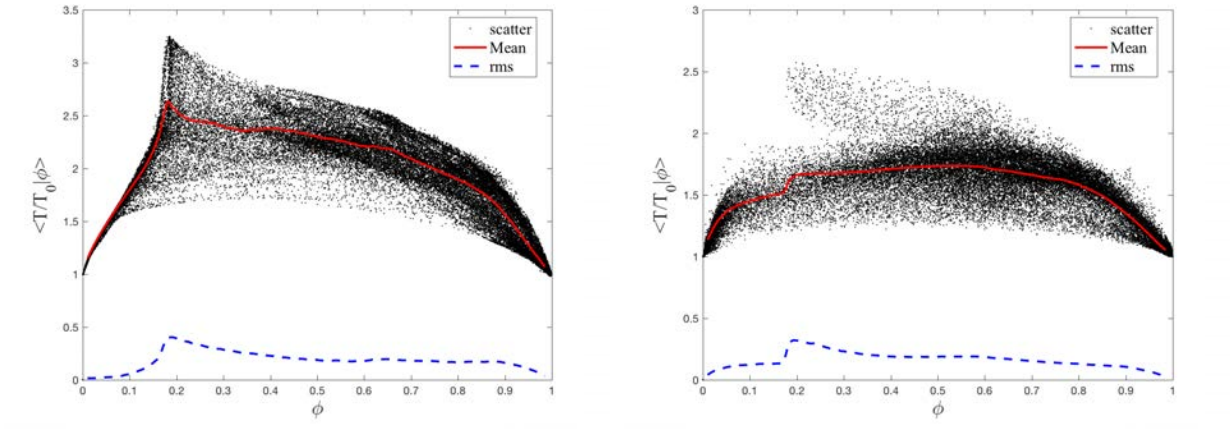


Figure 3.1: On the left the RGL EOS model Le≠1 and on the right the RGL EOS model Le=1 predictions of $< T/T_0|\phi >$ for Re=2500, and 1 atm ambient pressure at time of 65.

As we move on investigating the soot properties expected significant reductions are pexhibited. Figure 4.3 affirm the reduction in the fv predictions (i.e. fv is under-predicted by $\approx$ 90% with

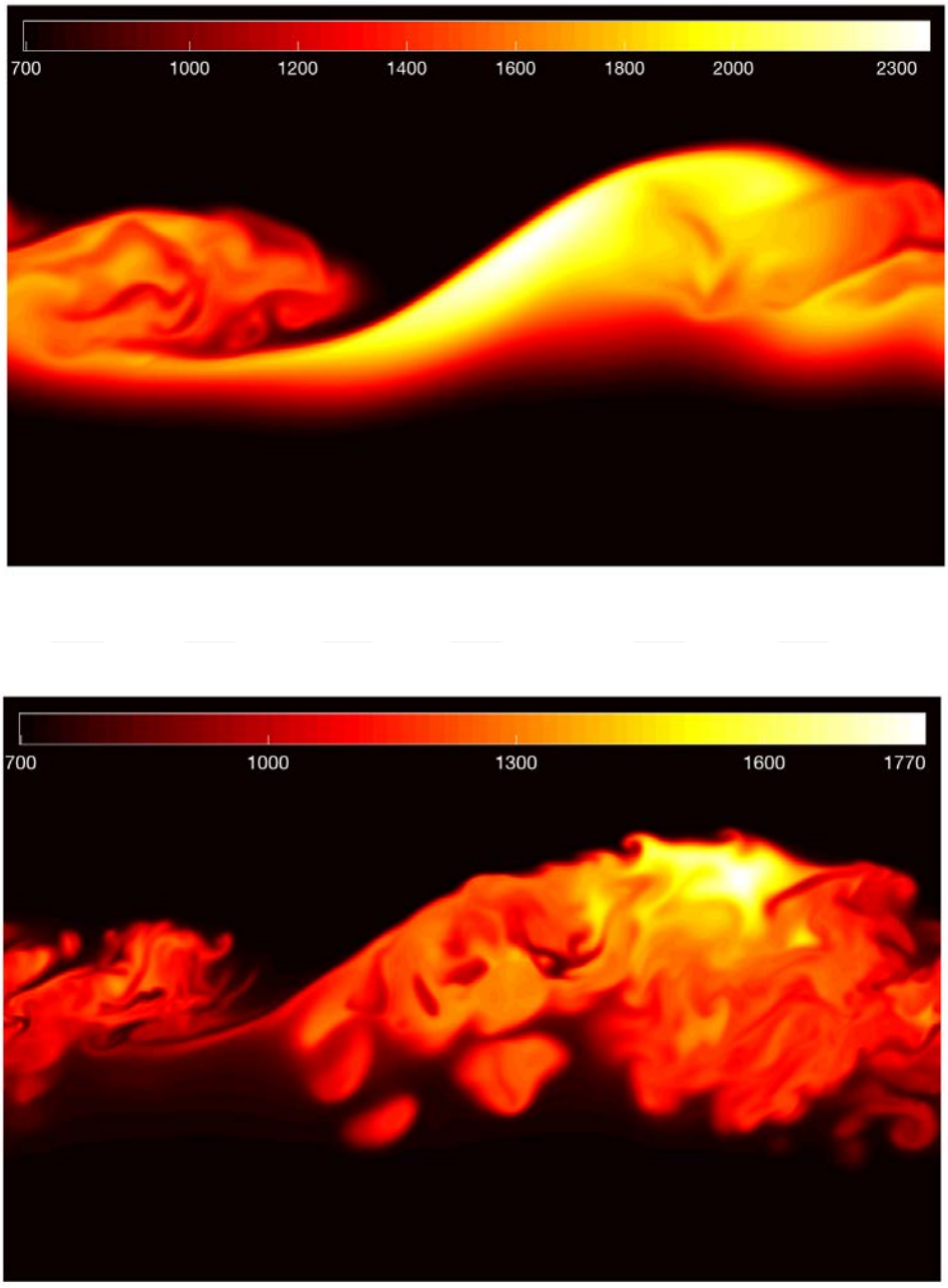


Figure 3.2: The comparison of contour plots of T(K) top is Le≠1 and bottom is Le=1 both coupled with the RGL EOS model for pressure 1 atm and Re=2500 at time of 65 predictions of 3D data.

unity Le # assumption). Even though the local flow effects on fv are still present, fv presents more scattered behavior in contrast to the non-unity Le # assumption predictions. Figure 4.4 reveals that an order of magnitude lower fv predictions of unity Le # assumption. Now, fv presents in the region where it is not monitored in the non-unity Le # assumption predictions. Another soot property, N is dominated by temperature while it is highly under-predicted by $\approx$ 54% which confirms the effect of the under-predicted flame temperature on soot load. The under-prediction of the flame temperature leads under-predictions of Y_s by $\approx$ 90% as well ([Fig. 4.6]). Comparison of the Fig.s 4.2, 4.4 and 4.7 shows us how equating the thermal and mass diffusivity effects the soot load distribution in the flame kernel. The scalar dissipation rate is over-predicted by $\approx$ 400% implying high levels of mixing which helps us to explain why flame temperature, fv, N and Y_s exhibit more scattered behavior than non-unity Le # predictions. Figure 4.8 displays how the scalar dissipation differs by adoption of the unity Le # assumption. Lastly, we focus on the soot generation rate which seems to be under-predicted by 56% ([Fig. 4.9]) which is one of the direct results of the under-prediction of the flame temperature.

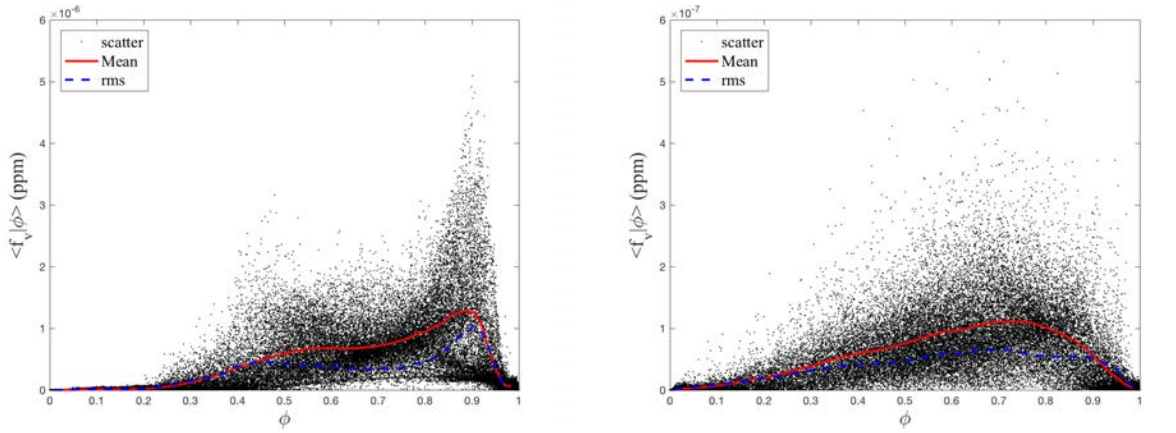


Figure 3.3: On the left the RGL EOS model Le≠1 and on the right the RGL EOS model Le=1 predictions of $< fv|\phi >$ for Re= 2500, and 1 atm ambient pressure at time of 65.

Figures 4.10 - 4.15 examine the effect of the unity Le # assumption effects coupled with the IGL EOS model. As it has been stated in the previous chapter the IGL EOS model well predicts the flame and soot properties with the non-unity Le # assumption which suggests that the IGL EOS model coupled with the unity Le # assumption predictions might posses the similar behavior observed the

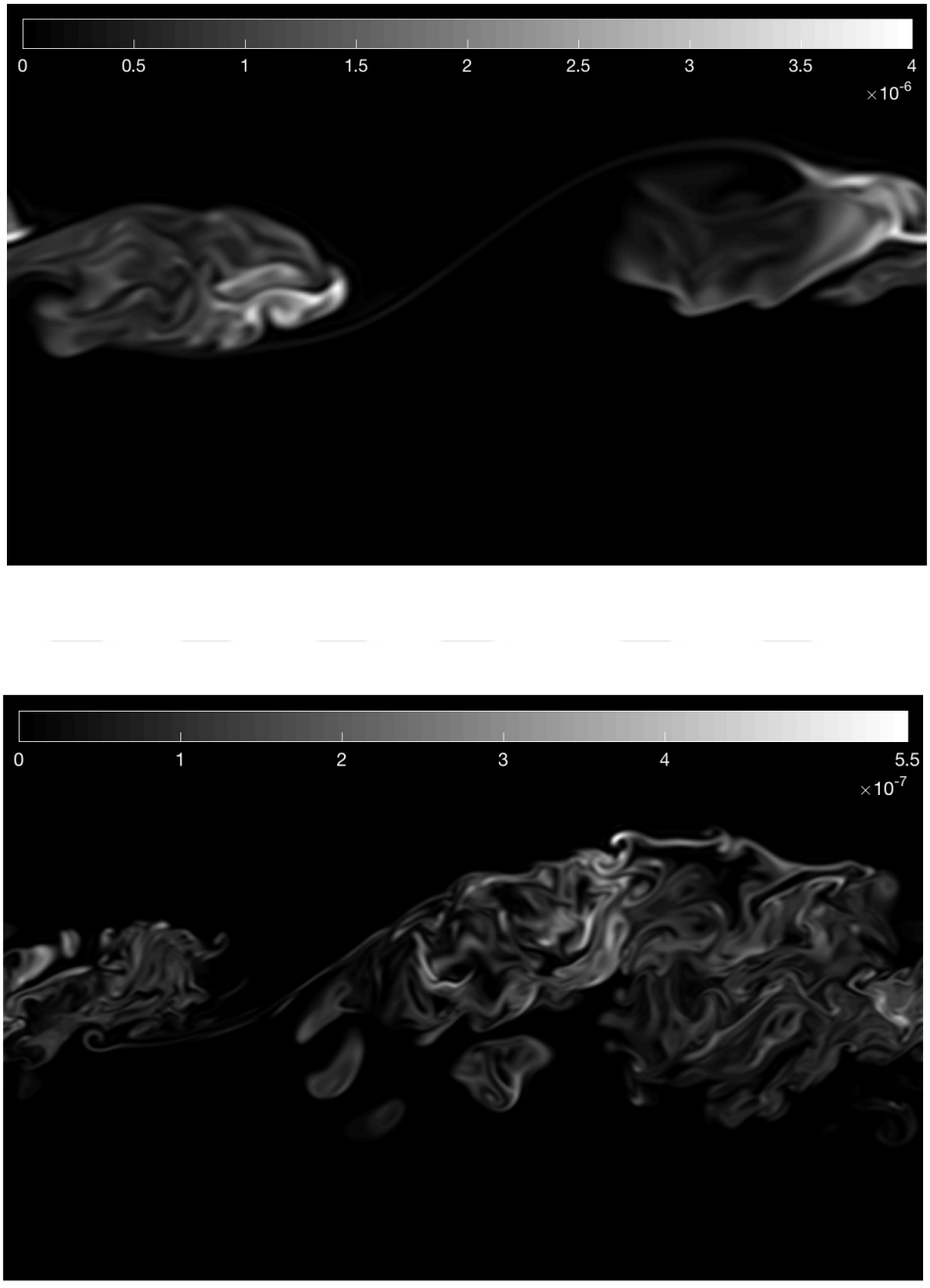


Figure 3.4: The comparison of contour plots of fv for pressure 1 atm and Re=2500, top is Le=1 and bottom is l ≠1predictions time of 65 3D data.

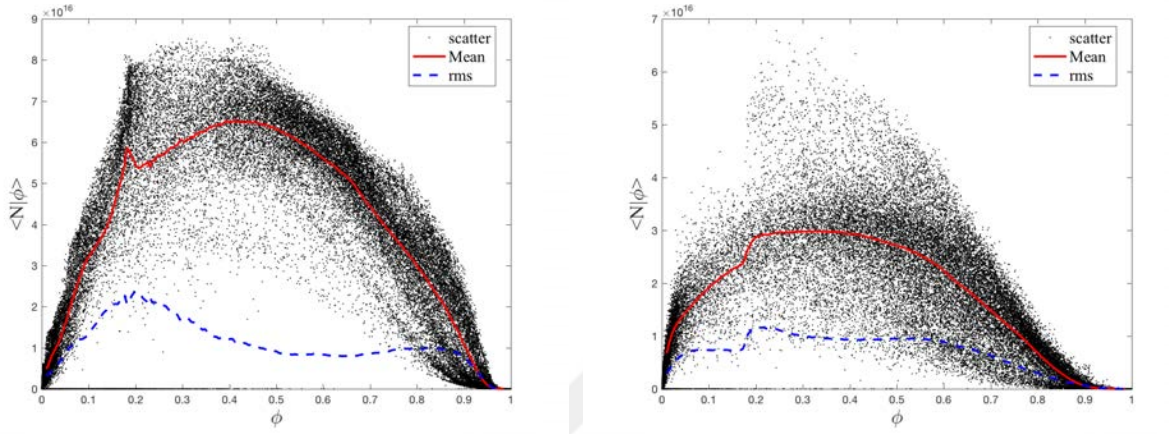


Figure 3.5: On the left the RGL EOS model Le≠1 and on the right the RGL EOS model Le=1 predictions of $< N|\phi >$ for Re= 2500, and 1 atm ambient pressure at time of 65.

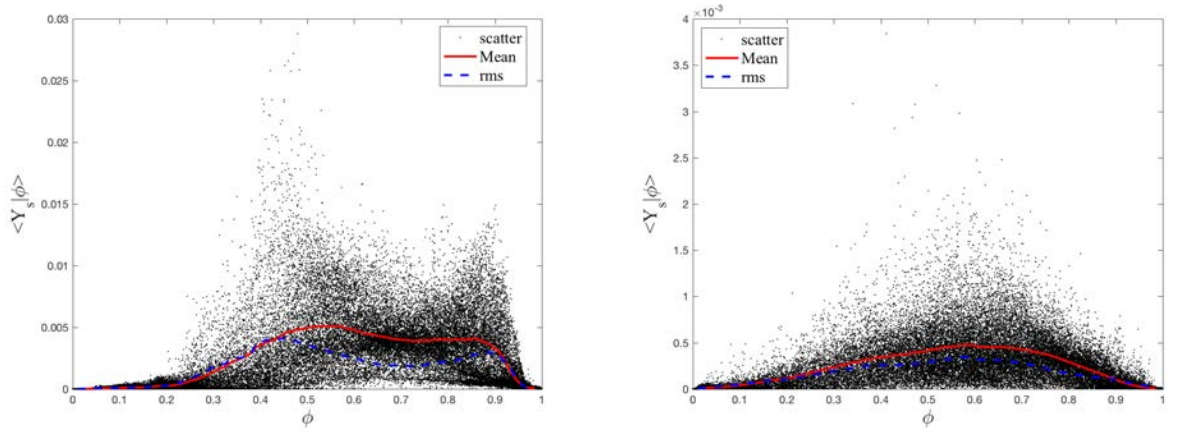


Figure 3.6: On the left the RGL EOS model Le≠1 and on the right the RGL EOS model Le=1 predictions of $< Ys|\phi >$ for Re=2500, and 1 atm ambient pressure at time of 65.

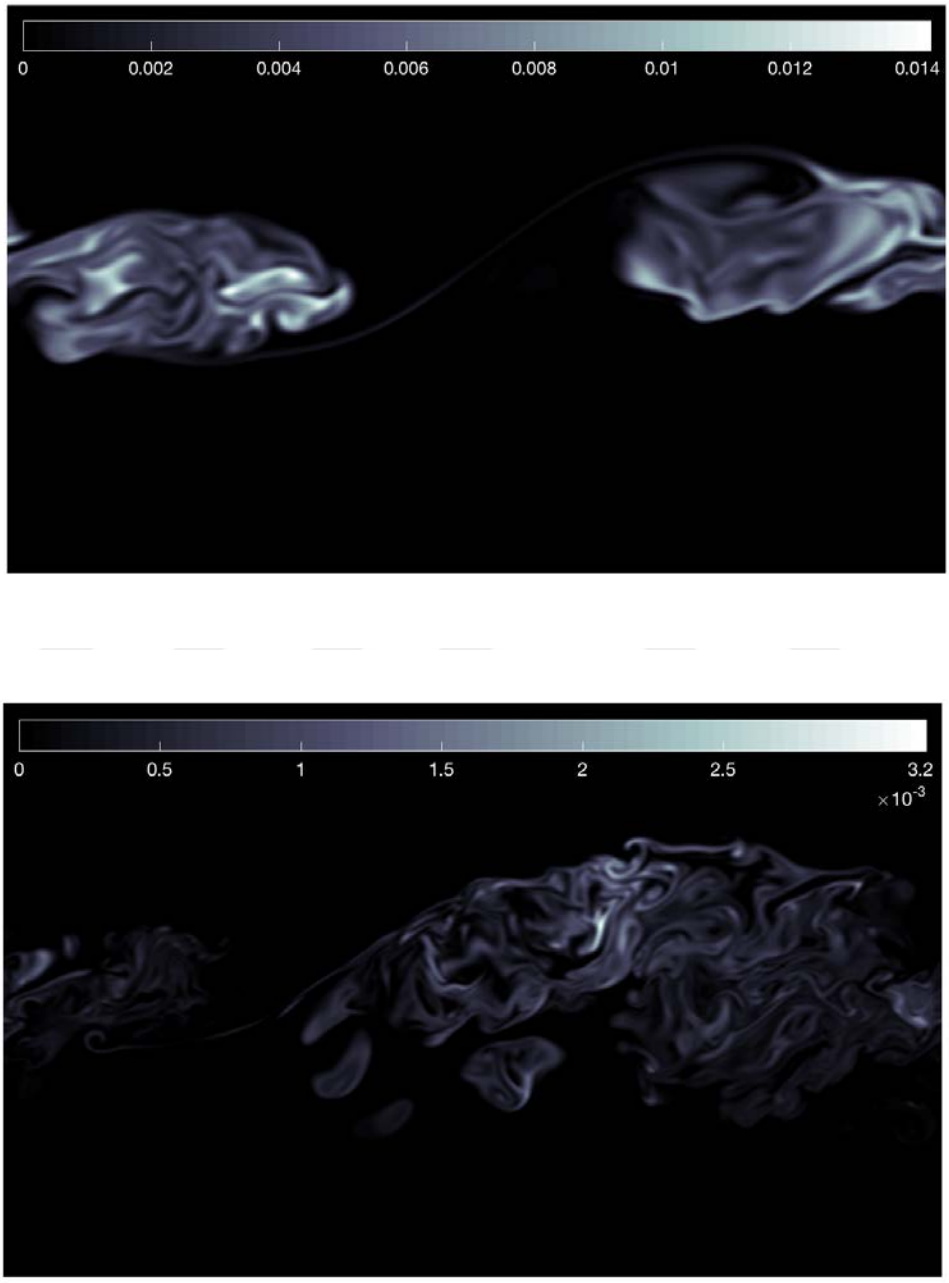


Figure 3.7: The comparison of contour plots of Ys for pressure 1 atm and Re=2500, top is Le=1 and bottom is l ≠1predictions time of 65 3D data.

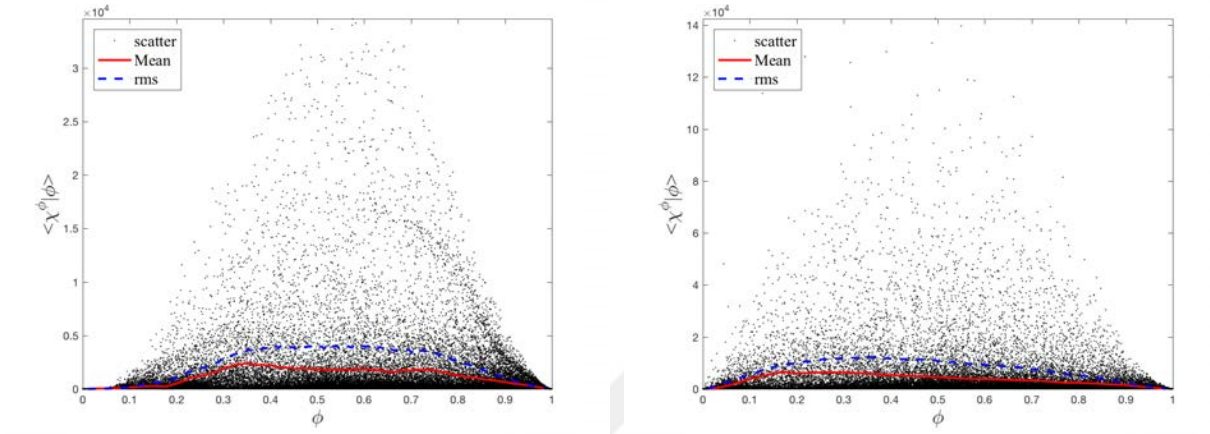


Figure 3.8: On the left the RGL EOS model Le≠1 and on the right the RGL EOS model Le=1 predictions of $< \chi|\phi >$ for Re=2500, and 1 atm ambient pressure at time of 65.

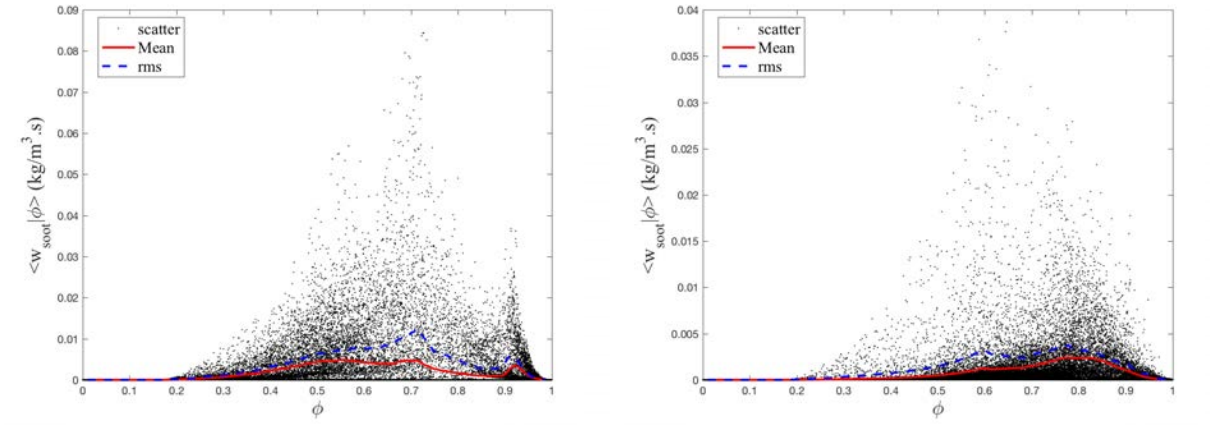


Figure 3.9: On the left the RGL EOS model Le≠1 and on the right the RGL EOS model Le=1 predictions of $< w_{soot}|\phi >$ for Re=2500, and 1 atm ambient pressure at time of 65.

ones in Figures 4.1 - 4.9. While the flame temperature and soot properties predictions are similar to the one obtained with the RGL EOS unity Le # model, the scalar dissipation rate predictions seizes a significantly abnormal profile (by having a large standard deviation in the fuel rich region Fig.[4.14]).

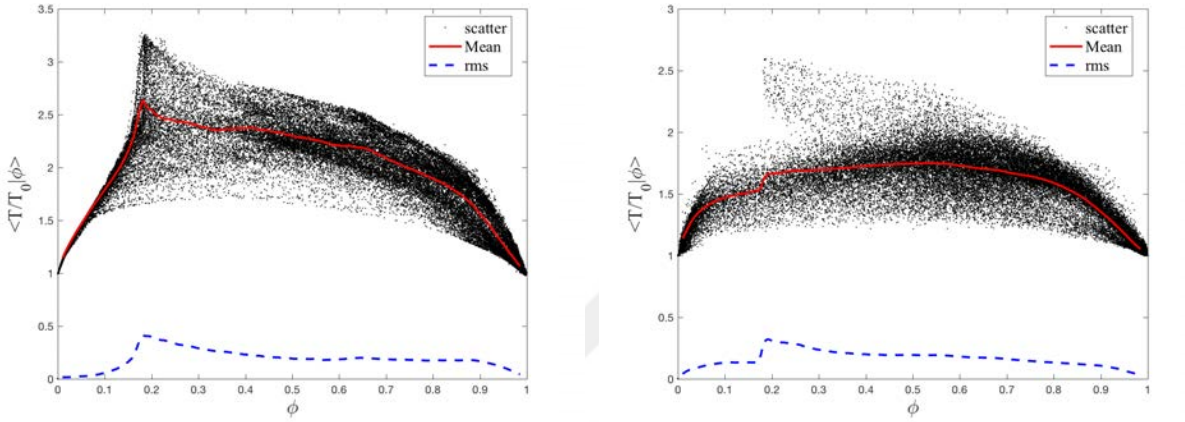


Figure 3.10: On the left the IGL EOS model Le≠1 and on the right the IGL EOS model Le=1 predictions of $< T/T_0|\phi >$ for Re=2500, and 1 atm ambient pressure at time of 65.

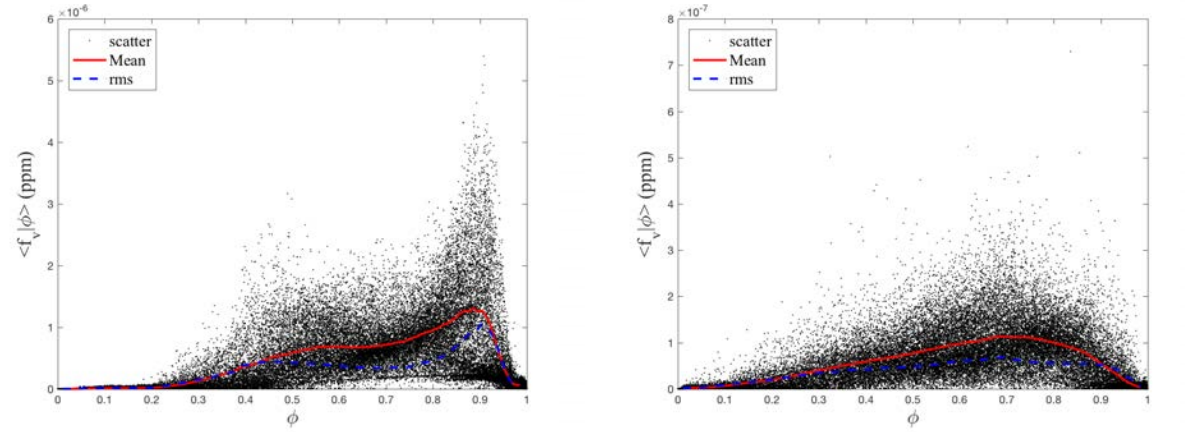


Figure 3.11: On the left the IGL EOS model Le≠1 and on the right the IGL EOS model Le=1 predictions of $< fv|\phi >$ for Re= 2500, and 1 atm ambient pressure at time of 65.

Figures 4.16 through 4.24 present a comparison of the unity Le # assumption coupled with the RGL and the IGL EOS model predictions of 3D atmospheric flames at time of 80. As the simulation time evaluates from 65 to 80, the high flame temperature packets are transported from the stoichiometric region to fuel rich region while insignificant decreases existed in both the RGL and the IGL EOS

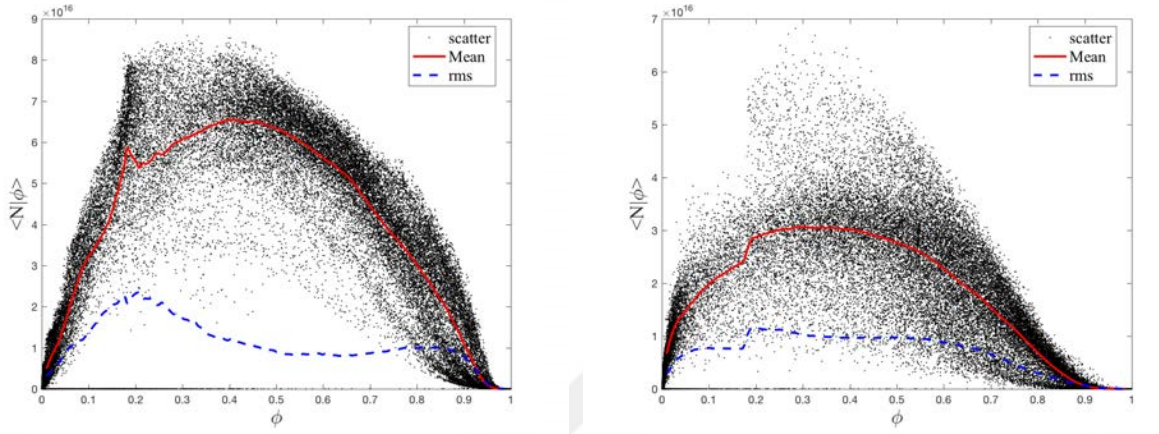


Figure 3.12: On the left the IGL EOS model Le≠1 and on the right the IGL EOS model Le=1 predictions of $< N|\phi >$ for Re= 2500, and 1 atm ambient pressure at time of 65.

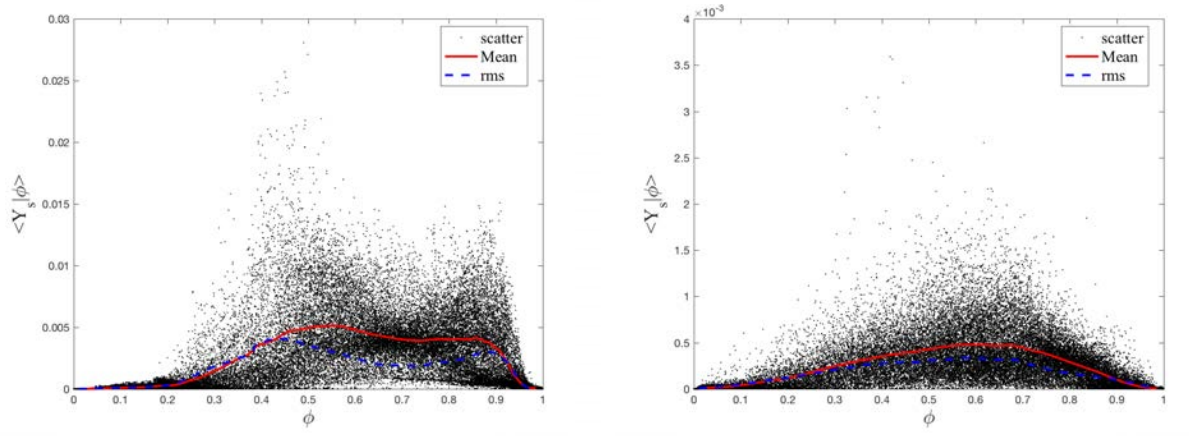


Figure 3.13: On the left the IGL EOS model Le≠1 and on the right the IGL EOS model Le=1 predictions of $< Ys|\phi >$ for Re=2500, and 1 atm ambient pressure at time of 65.

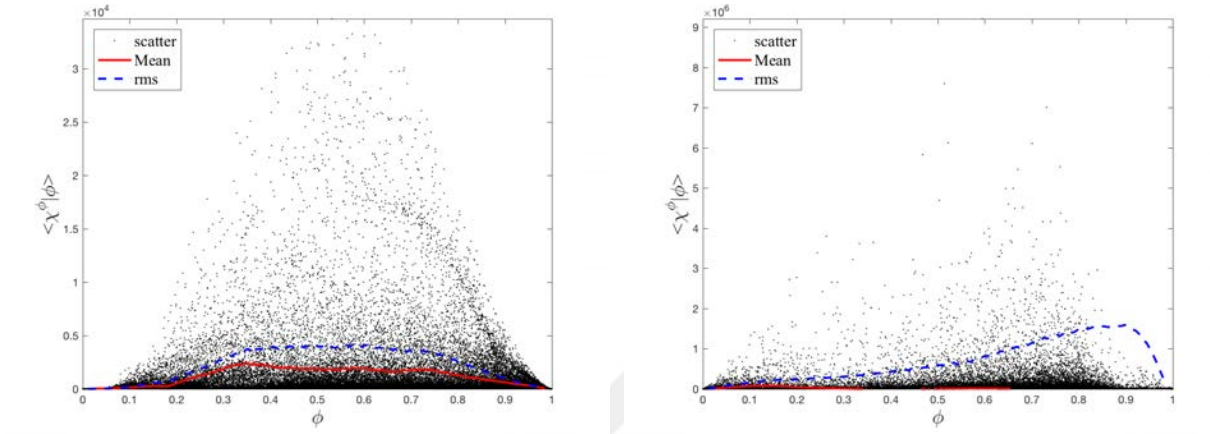


Figure 3.14: On the left the IGL EOS model Le≠1 and on the right the IGL EOS model Le=1 predictions of $< \chi|\phi >$ for Re=2500, and 1 atm ambient pressure at time of 65.

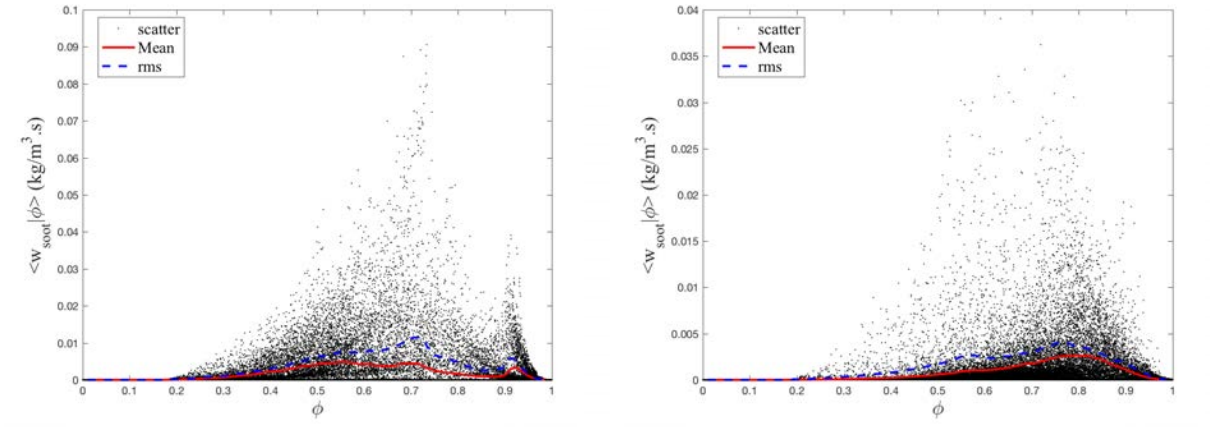


Figure 3.15: On the left the IGL EOS model Le≠1 and on the right the IGL EOS model Le=1 predictions of $< w_{soot}|\phi >$ for Re=2500, and 1 atm ambient pressure at time of 65.

models can be seen in Figures 4.16 and 4.17. The slight decreases in the flame temperature in both flames lead negligible reductions in fv, N and Y_s ([Fig.s 4.18, 4.19, 4.20, 4.21, 4.22 and 4.24]). The abnormal trend of the standard deviation of the scalar dissipation rate of the IGL EOS unity Le # model looks to be enlarged by 68% in the final time of the simulation ([Figure 4.23]).

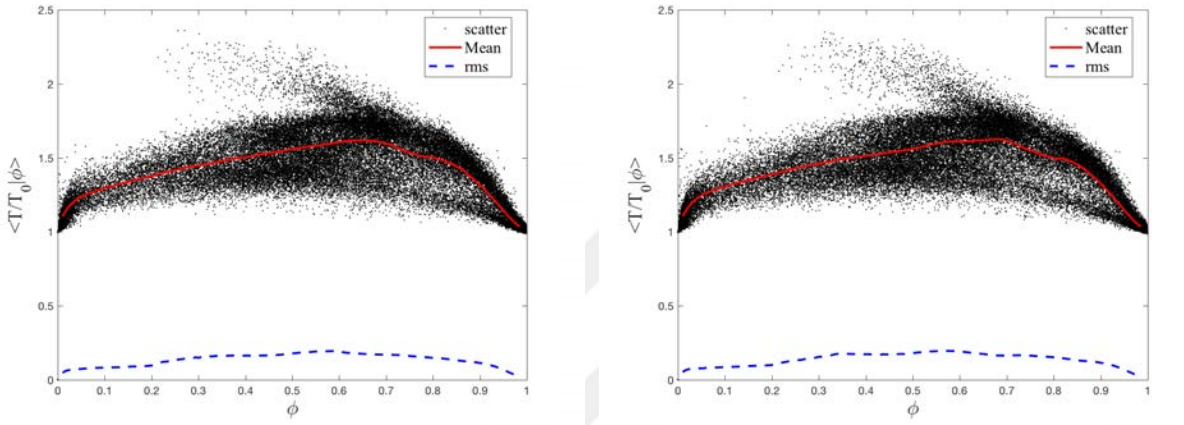


Figure 3.16: On the left the RGL EOS model and on the right the IGL EOS model predictions of $< T/T_0|\phi >$ for Re=2500, Le =1, and 1 atm ambient pressure at time of 80, 3D DNS data.

The examination of the pressure effects on the flame structure and soot load with unity Le assumption is also another focus of the current work. Figures 4.25 - 4.30 investigate how the flame temperature, soot properties (i.e. fv and Y_s) and species of CO, H and OH are influenced by the increasing ambient pressure. Figure 4.25 displays the mean temperature profile of the RGL and the IGL EOS models coupled with unity Le # assumption. For 1, 5 and 10 atm pressure flames for both the RGL and the IGL EOS models, the mean temperature flame profiles adopting either the RGL or the IGL EOS models has little impact on the mean temperature profiles, confirming a previously observed trend with the non-unity Le # assumption. However, by reaching the critical ambient pressure the IGL EOS model also over predicts the flame temperature. Predictions of fv seems to be not differentiated by the EOS model adoption ([Fig. 4.26]). In contrast to fv predictions, the soot mass fraction predictions address the importance of the EOS model adoption ([Fig. 4.27]). While the Y_s predictions of atmospheric and 5 atm flames for both models look identical, the dissimilarity in Y_s profiles starts with 10 atm flames. In the RGL EOS model predicts Y_s profile to 'mimic' Y_s prediction of 5 atm while having slightly

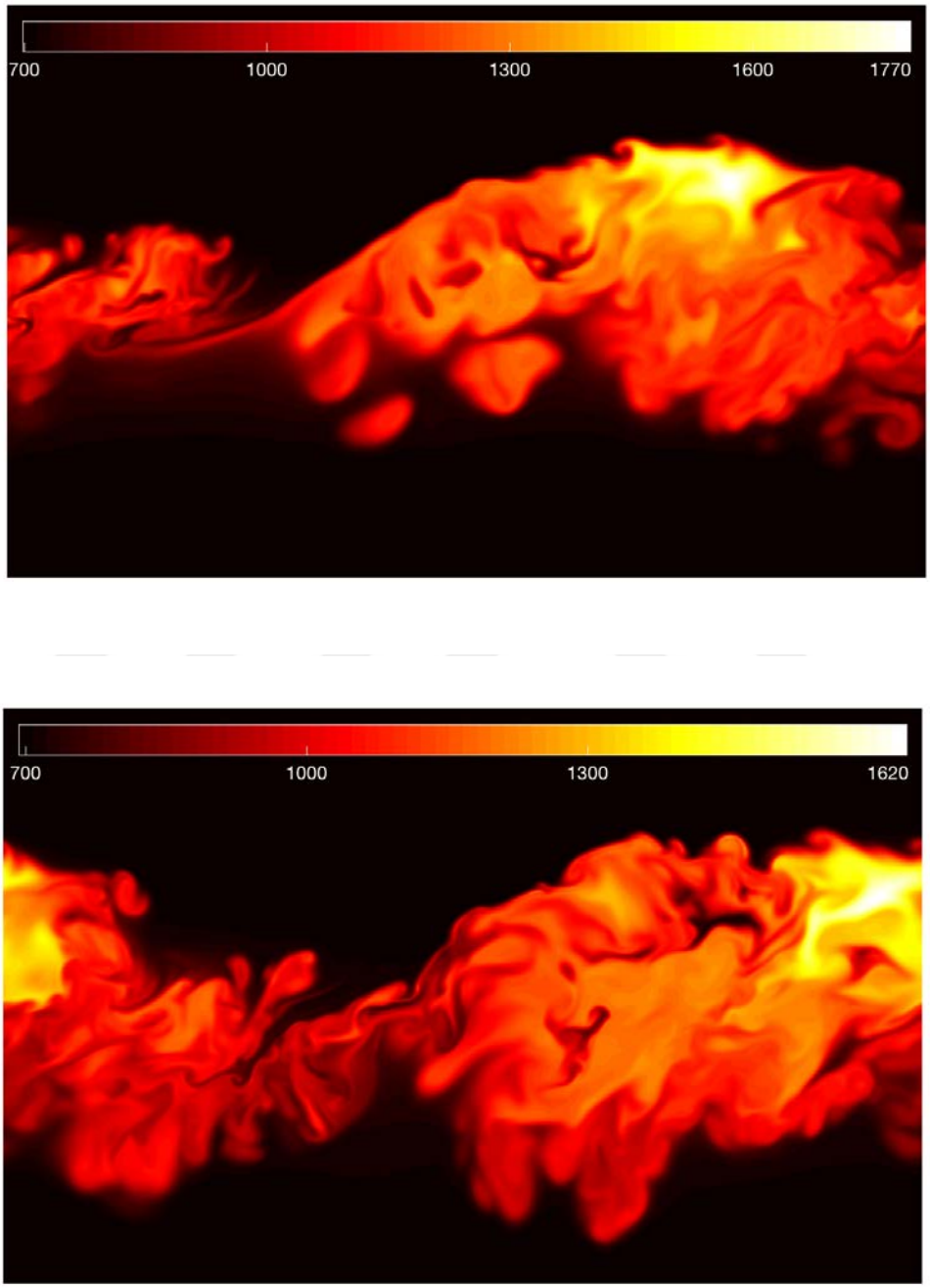


Figure 3.17: The comparison of contour plots of T(K) for pressure 1 atm, Le=1 and Re=2500, top sub-figure is created the RGL EOS, and bottom one is created with the IGL EOS model at time of 80 for 3D data.

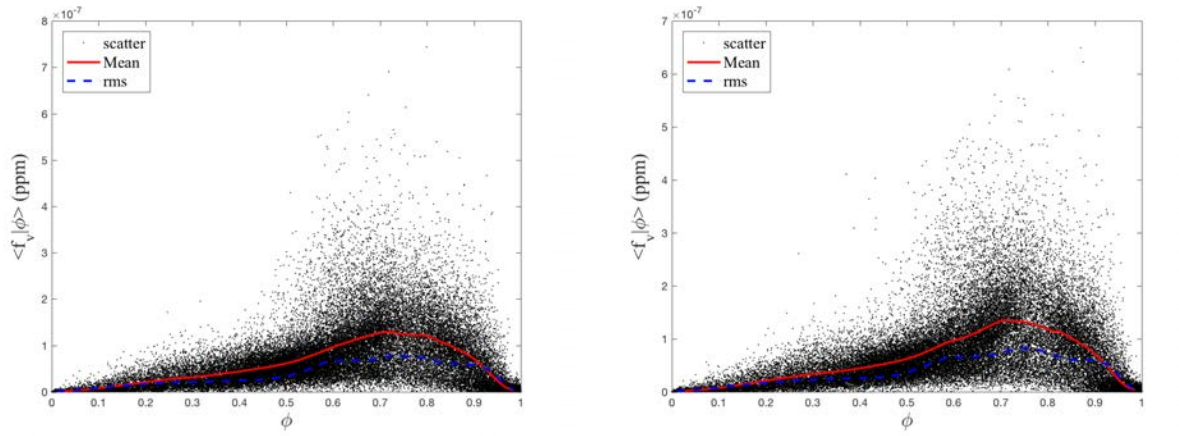


Figure 3.18: On the left the RGL EOS model and on the right the IGL EOS model predictions of $< fv|\phi >$ for Re=2500, Le =1, and 1 atm ambient pressure at time of 80, 3D DNS data.

larger peak Y_s value than 5 atm prediction. The IGL EOS model predicts the Y_s to have a similar profile with the atmospheric pressure flame Y_s prediction. The elevated pressure flame Y_s predictions differs in two different manner. First, the peak value of Y_s predictions of the IGL EOS model is larger than the RGL model prediction by 16%, and second the Y_s exhibits a more widened profile than the RGL EOS Y_s profile does.

Figures 4.28, 4.29 and 4.30 have significance to demonstrate the soot oxidation process in the flame, since during direct oxidation process CO and H is produced while OH is involved in the soot oxidation. The soot oxidation rate is seen to be almost identical for the atmospheric pressure flames for both EOS models, since Y_{CO}, Y_H and Y_{OH} have similar profiles in both flames. When pressure is increased to be 5 atm, the oxidation of soot by Y_{O_2} seems to be not affected by the EOS model adoption, since the Y_{CO} profiles of these two model predictions present similarities with each other in Figure 4.28. However, Y_{OH} affirms a slight effect of the EOS model adoption on this soot oxidation step, since Y_{OH} is predicted slightly by the IGL EOS larger than the RGL EOS model prediction. When the pressure reaches to 10 atm, Y_s, Y_{CO}, Y_H and Y_{OH} profiles support the idea that soot oxidation rate is larger in the region $\phi \approx 0.4$ to 0.75 in the RGL EOS model predictions. In contrast to 10 atm flames, in 35 atm flames soot oxidation rates becomes larger in the IGL EOS model predictions in the region $\phi \approx 0.25$ to 0.9.

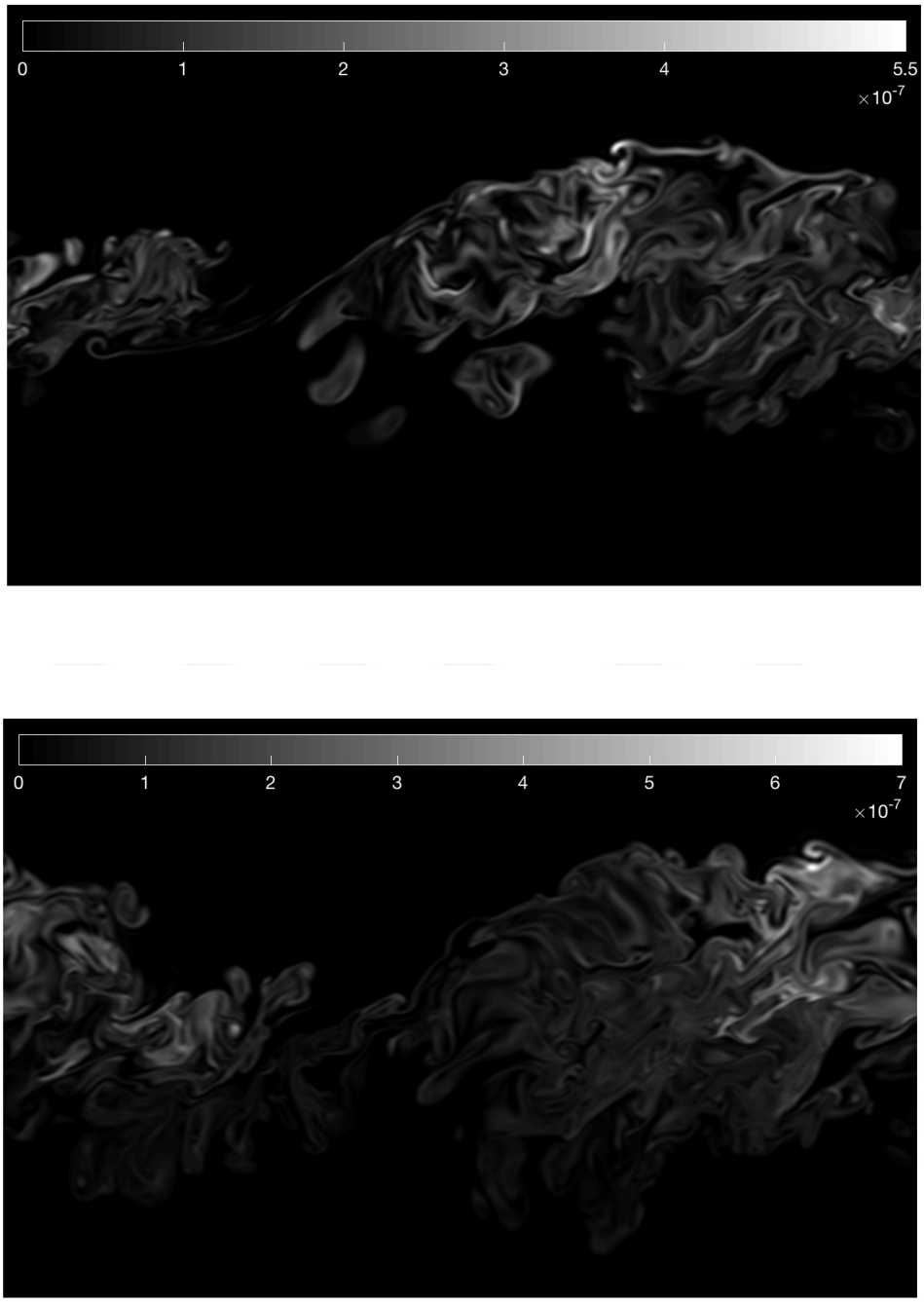


Figure 3.19: The comparison of contour plots of fv for pressure1 atm, Le=1 and Re=2500, top subfigure is created the RGL EOS, and bottom one is created with the IGL EOS model at time of 80 for 3D data.

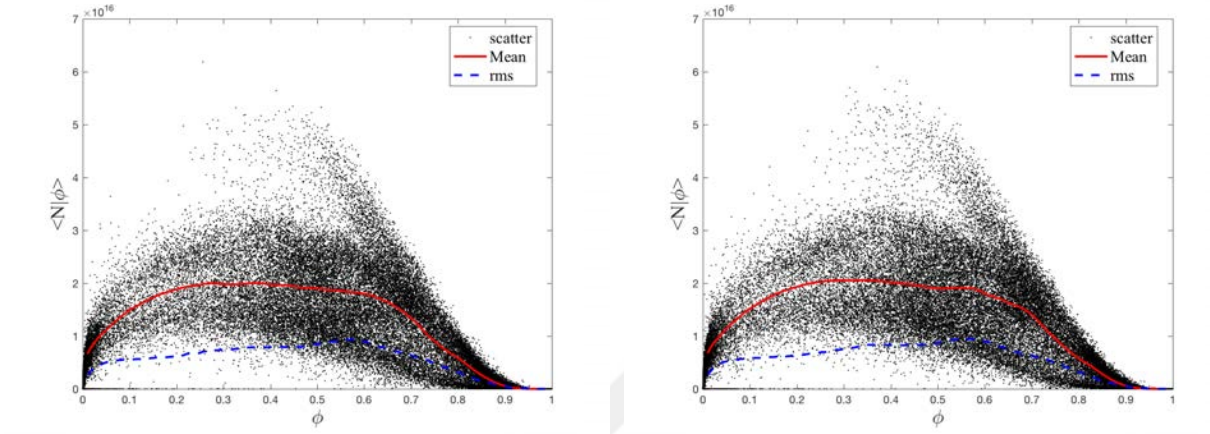


Figure 3.20: On the left the RGL EOS model and on the right the IGL EOS model predictions of $< N|\phi >$ for Re=2500, Le =1, and 1 atm ambient pressure at time of 80, 3D DNS data.

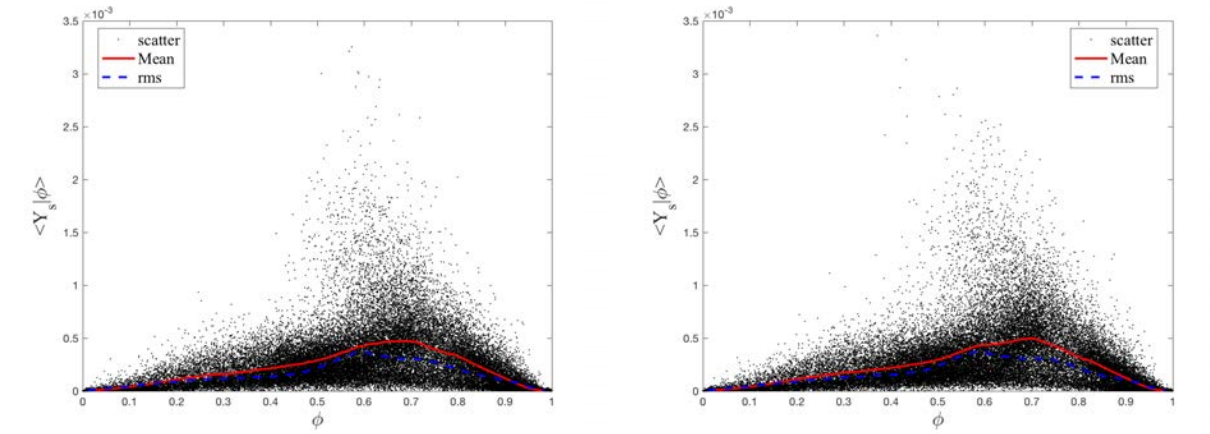


Figure 3.21: On the left the RGL EOS model and on the right the IGL EOS model predictions of $< Ys|\phi >$ for Re=2500, Le =1, and 1 atm ambient pressure at time of 80, 3D DNS data.

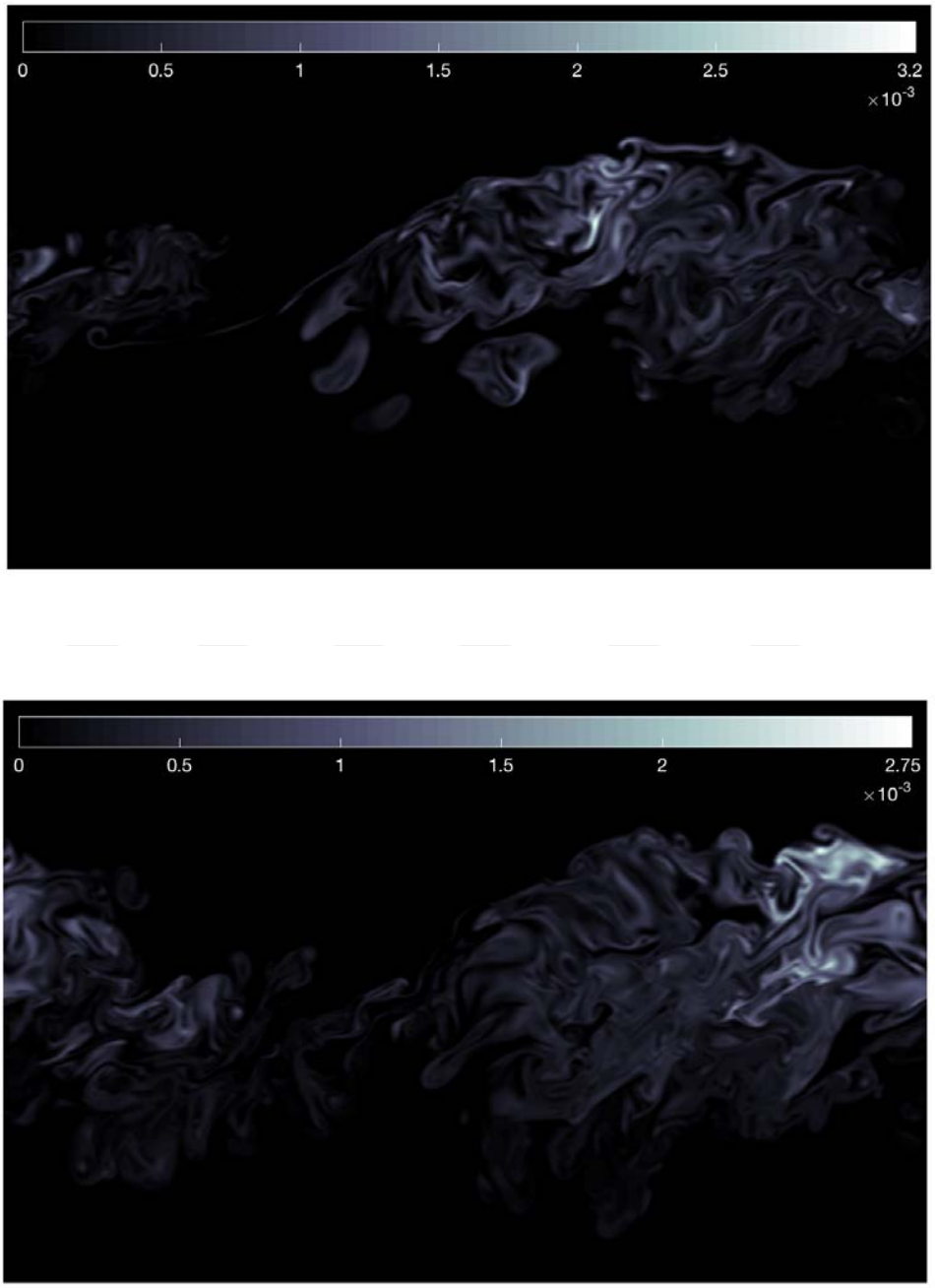


Figure 3.22: The comparison of contour plots of Ys for pressure 1 atm, Le=1 and Re=2500, top sub-figure is created the RGL EOS, and bottom one is created with the IGL EOS model at time of 80 for 3D data.

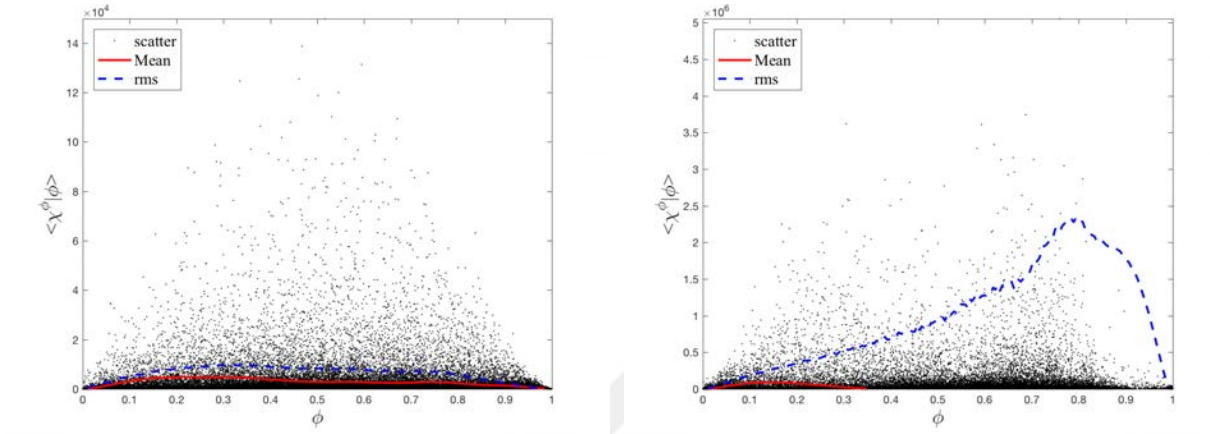


Figure 3.23: On the left the RGL EOS model and on the right the IGL EOS model predictions of $< \chi|\phi >$ for Re=2500, Le =1, and 1 atm ambient pressure at time of 80, 3D DNS data.

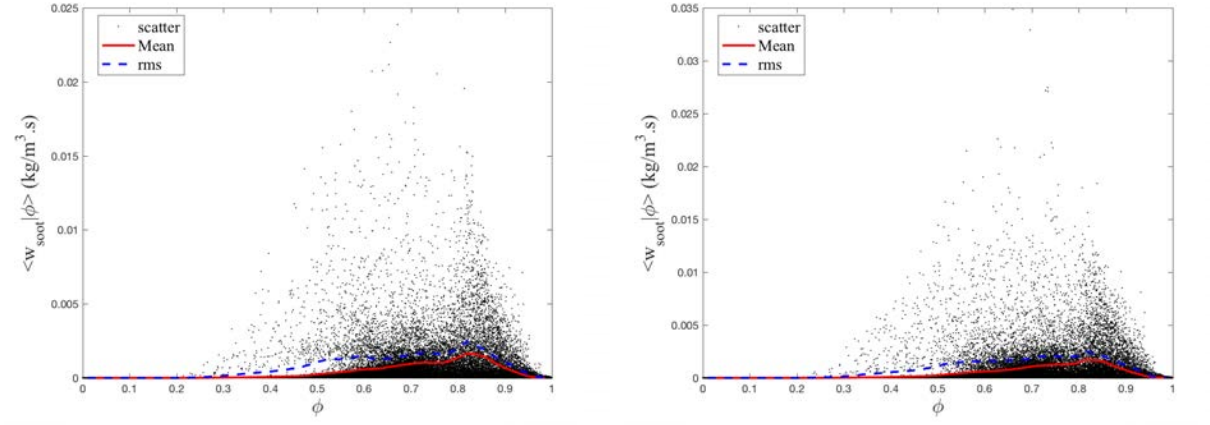


Figure 3.24: On the left the RGL EOS model and on the right the IGL EOS model predictions of $< w_{soot}|\phi >$ for Re= 2500, Le =1, and 1 atm ambient pressure at time of 80, 3D DNS data.

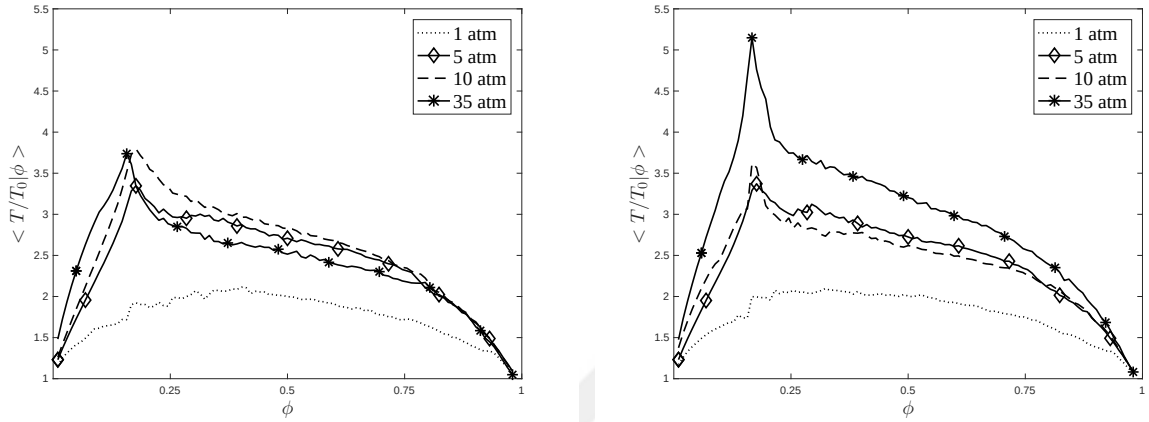


Figure 3.25: On the left the RGL EOS model and on the right the IGL EOS model predictions of $< T/T_0|\phi >$ for Re=2500, Le =1, and 1 atm ambient pressure at time of 65, 2D DNS data.

The

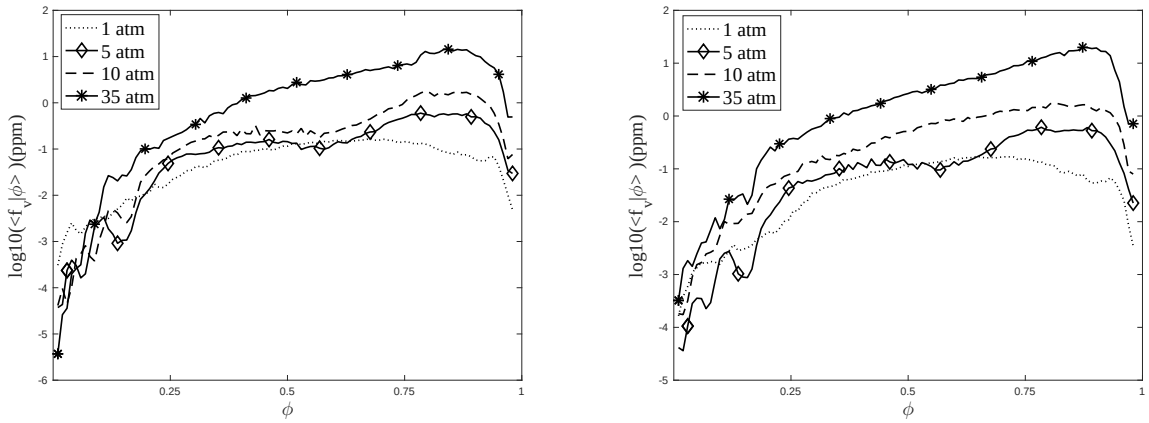


Figure 3.26: On the left the RGL EOS model and on the right the IGL EOS model predictions of log10$< fv|\phi >$ for Re=2500, Le =1, and 1 atm ambient pressure at time of 80, 2D DNS data.

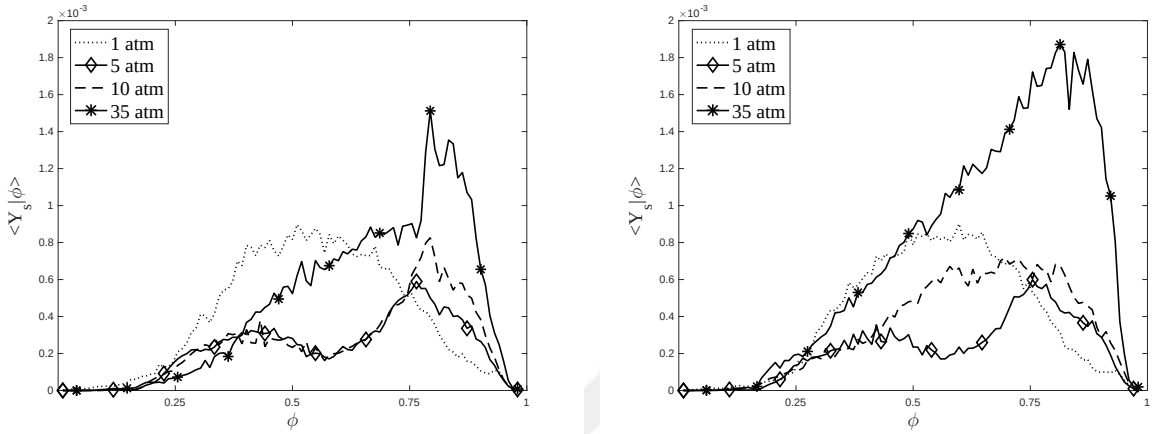


Figure 3.27: On the left the RGL EOS model and on the right the IGL EOS model predictions of $< Ys|\phi >$ for Re=2500, Le =1, and 1 atm ambient pressure at time of 80, 2D DNS data.

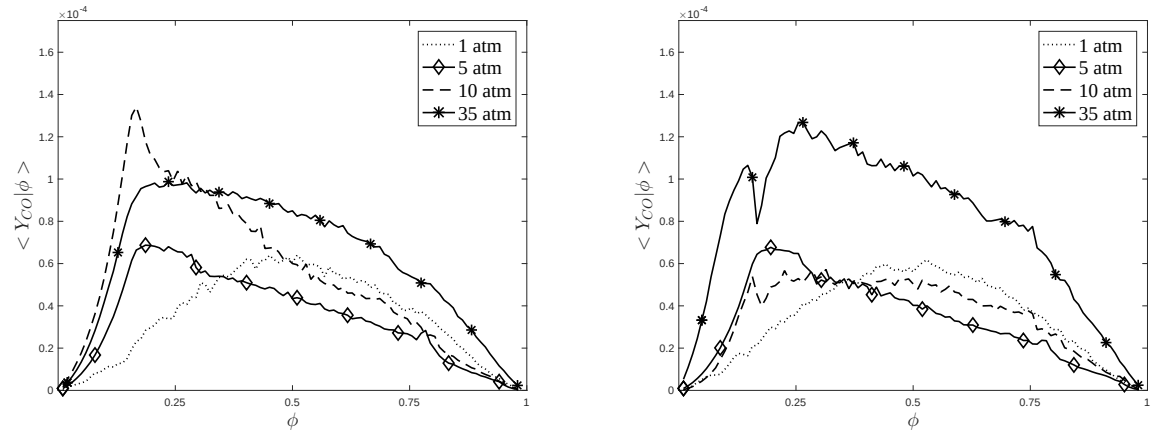


Figure 3.28: On the left the RGL EOS model and on the right the IGL EOS model predictions of $< Y_{CO}|\phi >$ for Re=2500, Le =1, and 1 atm ambient pressure at time of 80, 2D DNS data.

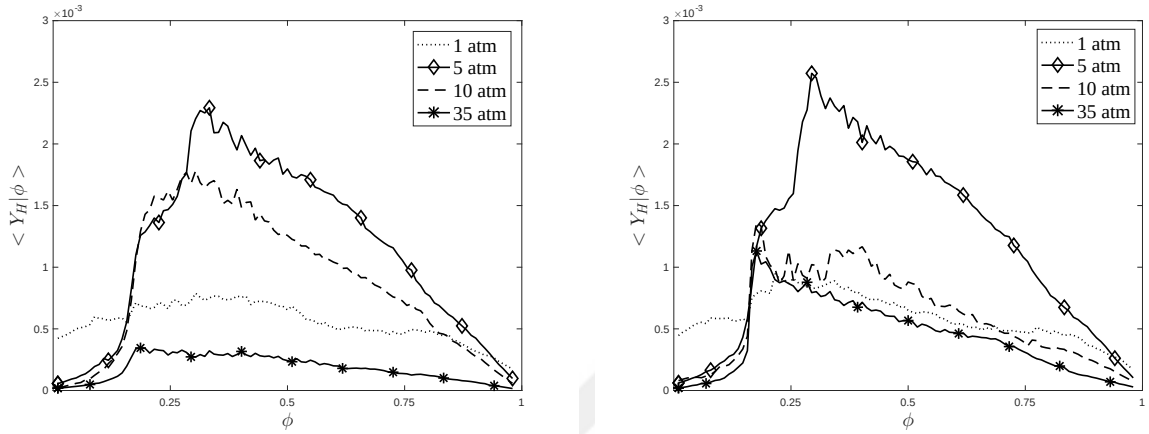


Figure 3.29: On the left the RGL EOS model and on the right the IGL EOS model predictions of $Y_H|\phi >$ for Re= 2500, Le =1, and 1 atm ambient pressure at time of 80, 2D DNS data.

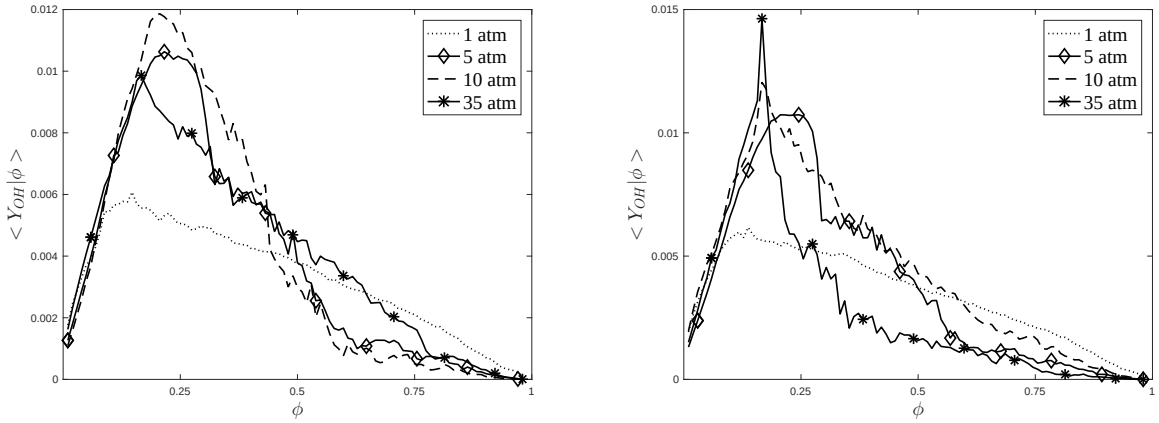


Figure 3.30: On the left the RGL EOS model and on the right the IGL EOS model predictions of $< Y_{OH}|\phi >$ for Re= 2500, Le =1, and 1 atm ambient pressure at time of 80, 2D DNS data.

So far we have compared the predictions of two different EOS model and two different diffusion assumptions for four distinct ambient pressures separately. Since the current work is the first attempt to examine the effects of the EOS and diffusion assumptions, now, we will deeply examine the EOS, diffusion and pressure effects in the following from Figures 4.31 through 4.36 for 2D data at time of 80. Figure 4.31 exhibits the mean temperature profiles for different ambient pressures while employing the RGL and the IGL EOS models coupled with the non-unity and unity Le # assumptions. Figure 4.31 (a) examines the atmospheric pressure flames by showing that employing either of the EOS models will have insignificant effects on the mean temperature, however switching from the non-unity Le # to unity Le # will cause a $\approx$ 15% temperature drop (i.e. soot load will be under-predicted). Figure 4.31 (b) displays the calculated mean temperature profiles. In the 5 atm flames we observe a slight temperature drop when the unity Le # assumption employed (i.e. $\approx$ 10% temperature drop has been observed between the non-unity Le # and the unity Le # assumptions coupled with the RGL EOS models), whereas choosing either of the EOS models. Even though both EOS models coupled with unity Le # assumptions sliglthly under-predicts the temperature profiles, it is capable of the catch the temperature behavior predicted by the non-unity Le # assumption for both EOS models for 5 and 10 atm flames ([Figure 4.31 (a) and (b)]). Lastly, we will check the mean temperature profile predictions for 35 atm flames calculated with two different EOS models coupled with either the non-unity Le or unity Le # assumption ([Figure 4.31 (d)]). Figure 4.31 (d) tells us that both EOS and diffusion assumption adoptions have significant influence on the flame predictions. Alteration of the EOS model from the RGL to the IGL coupled with the non-unity Le # assumption causes an over-prediction of the mean flame temperature by $\approx$ 21%, while switching from the non-unity Le # to unity Le # leads us to under-predict the mean peak flame temperature by $\approx$ 18% for the RGL and the $\approx$ 10% for the IGL model. Over all the unity Le # assumption again fairly captures the trends of the mean temperature profile.

Figure 4.32 (a) examines the impacts of the EOS and diffusion assumptions made in the atmospheric pressure flames. The unity Le assumption over predicts fv through from ϕ =0 to $\approx$ 0.7 in the mixture fraction region, while the trend is caught by the unity Le # for both EOS models. Figure 4.32 (b)

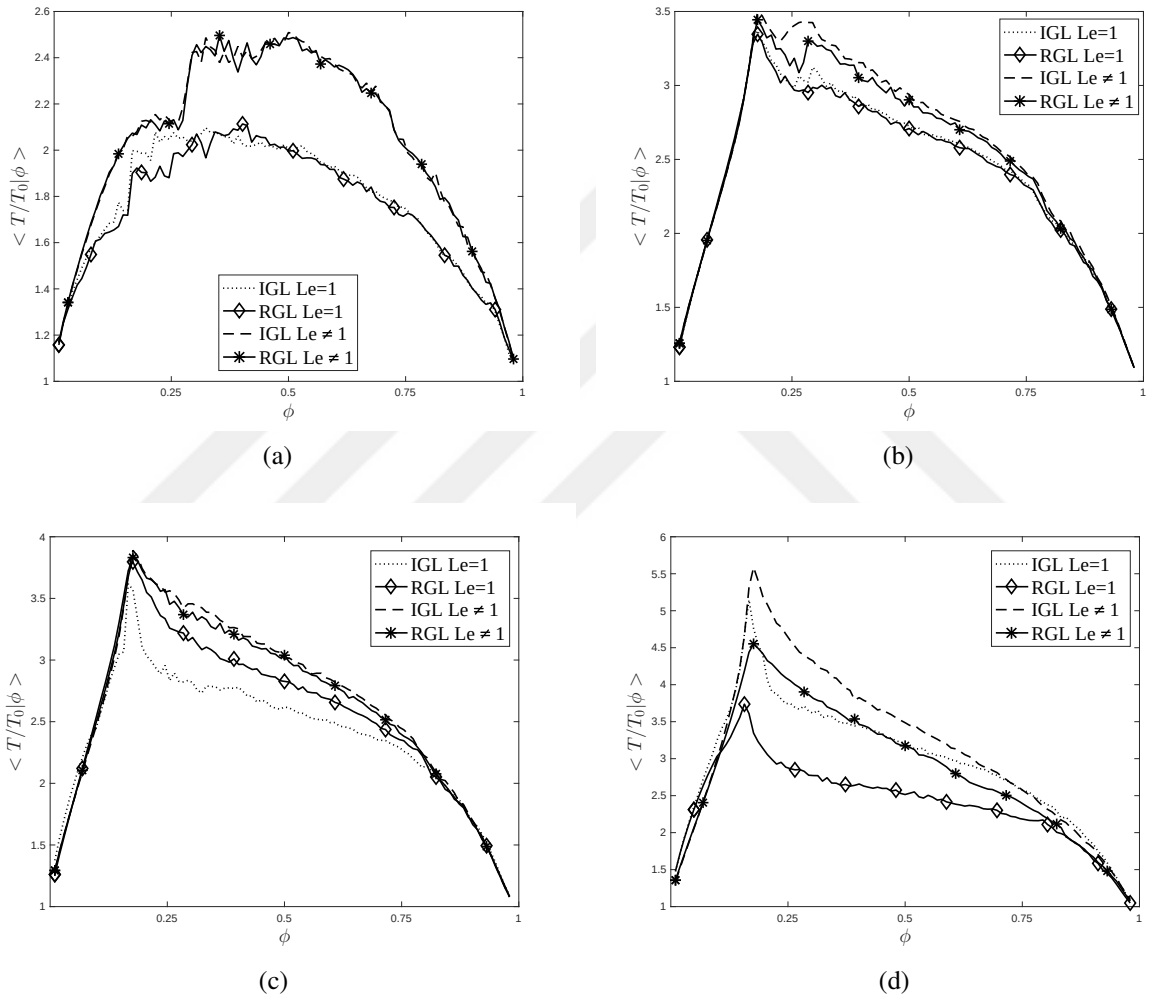


Figure 3.31: The comparison of $< T/T_0|\phi >$ for different ambient pressures, the EOS models and diffusion assumptions flames (a) 1 atm, (b) 5 atm, (c) 10 atm and (d) 35 atm ambient pressures.

displays the fv predictions of 5 atm flames, and it might be safe to say that fv predictions are not differentiated from each other for both EOS and non-unity and unity Le assumptions. 10 atm flames predictions of the IGL EOS coupled with unity Le # assumption predictions to be one order magnitude larger than other three predictions in the region of $\phi \approx 0.45$ to 0.75 in Figure 4.32 (c). When the unity Le # assumption employed with the IGL EOS model fails to predict the fv profile except the regions of $\phi \approx 0.22$ to 0.45 and $\phi \approx 0.75$ to 1. Figure 4.32 (d) shows us that either changing from the RGL to the IGL EOS or non-unity to unity Le # assumptions lead us to mis-predictions of the fv profiles in the region of $\phi \approx 0$ to 0.22 (i.e. fuel lean region).

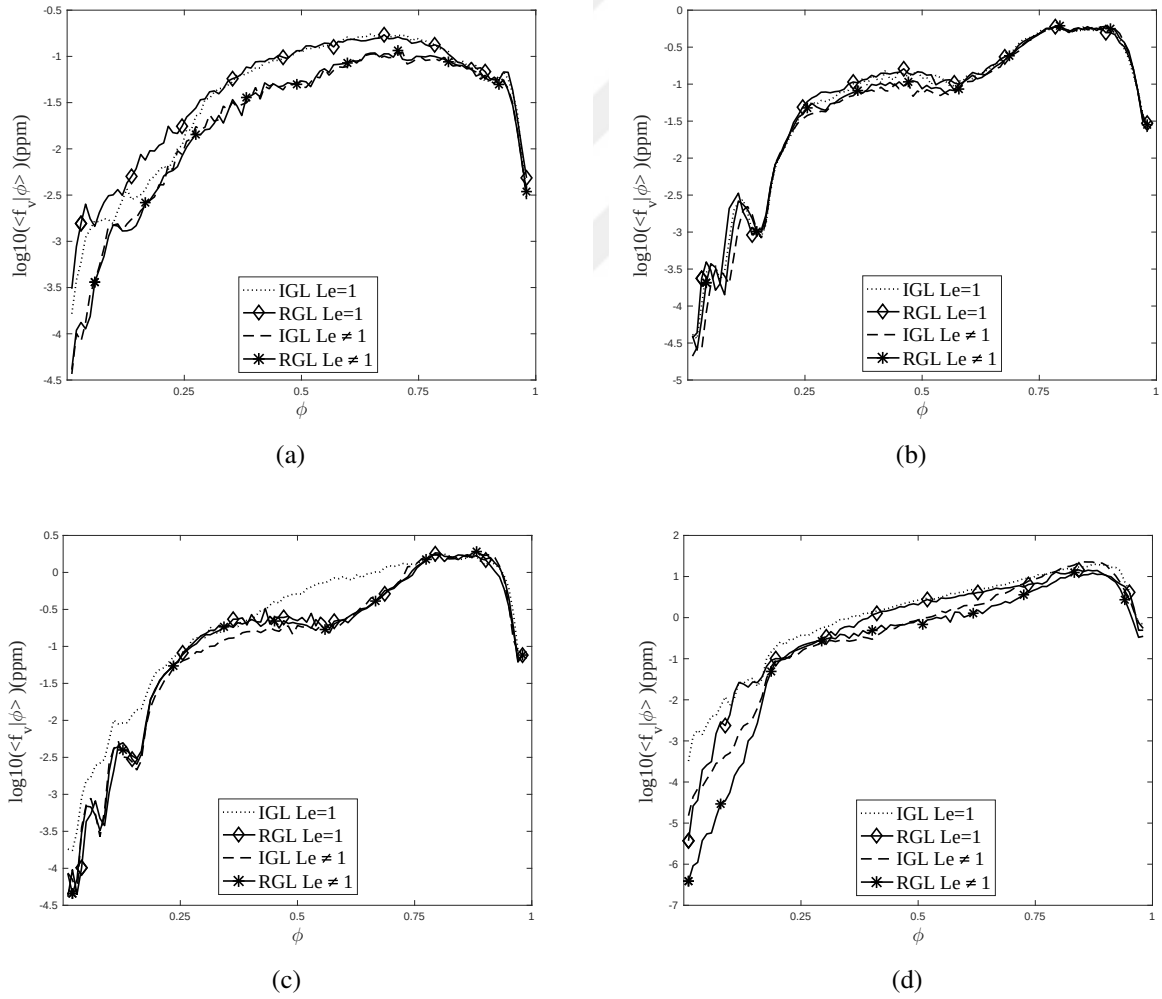


Figure 3.32: The comparison of $< fv|\phi >$ for different ambient pressures, the EOS models and diffusion assumptions flames (a) 1 atm, (b) 5 atm, (c) 10 atm and (d) 35 atm ambient pressures.

Figure 4.33 (a) investigates the Y_s in the atmospheric pressure flames. As aforementioned in the earlier chapter, switching between the EOS models has insignificant impacts on Y_s, however coupling the EOS models with the unity Le # assumption causes under-prediction of Y_s, while the trend of the Y_s profiles are fairly caught. Figure 4.33 (b) represents 5 atm flames prediction profiles of Y_s. By increasing pressure soot load starts to be transported to the fuel rich side of the flame, while it is reduced by $\approx$ 35% for the non-unity Le # predictions, while it is $\approx$ 12% for the unity Le # predictions. When we move on Figure 4.33 (c), except the Y_s prediction of the IGL EOS model coupled with the unity Le # assumption, soot load and the profiles follow the a similar trend to each other. In the $\phi \approx 0.4$ to 0.75 Y_s is over-predicted and from $\phi \approx 0.75$ to 1 under-predicted by the IGL EOS model employing unity Le # assumption. From Figures 4.31 4.32 (c) and 4.33 support each other implying that the IGL EOS coupled with the unity Le assumption will fail to predict the flame and soot properties appropriately. Figure 4.33 (d) displays predictions of Y_s profile for the 35 atm flames. As it has been stated in the above, switching from the RGL to the IGL EOS results with the over-predictions of flame temperature leading mis-predictions of the soot properties. Now, we confirm that coupling the unity Le # assumption with the IGL EOS leads us to a similar observation for Y_s through out the mixture fraction region.

Figure 4.34 (a) and (b) show that the 5 atm predictions of Y_H are very well predicted for all the models have been considered in this work, while switching between non-unity and unity Le # assumptions causes significant failures in predictions of Y_sH in atmospheric pressure flames. Figure 4.34 (c) verify the incapability of the IGL EOS model coupled with the unity Le # assumption to predict the flame characteristics by under-predicting of Y_H which is produced in the soot oxidation process. The under-prediction of the Y_H explains why we observe larger soot load in the 10 atm flames predictions of the IGL EOS model employing the unity Le # assumption. Figure 4.33 (d) implies the soot oxidation process in 35 atm flames. This sub-figure implies that the RGL and the IGL EOS models coupled with the non-unity Le # assumption predictions of Y_CO should follow a similar trend with Y_H since the heterogeneous and the homogeneous soot oxidation steps include both species to be produced. This sub-figure also reveals the fact that even though soot load is over-predicted by the IGL

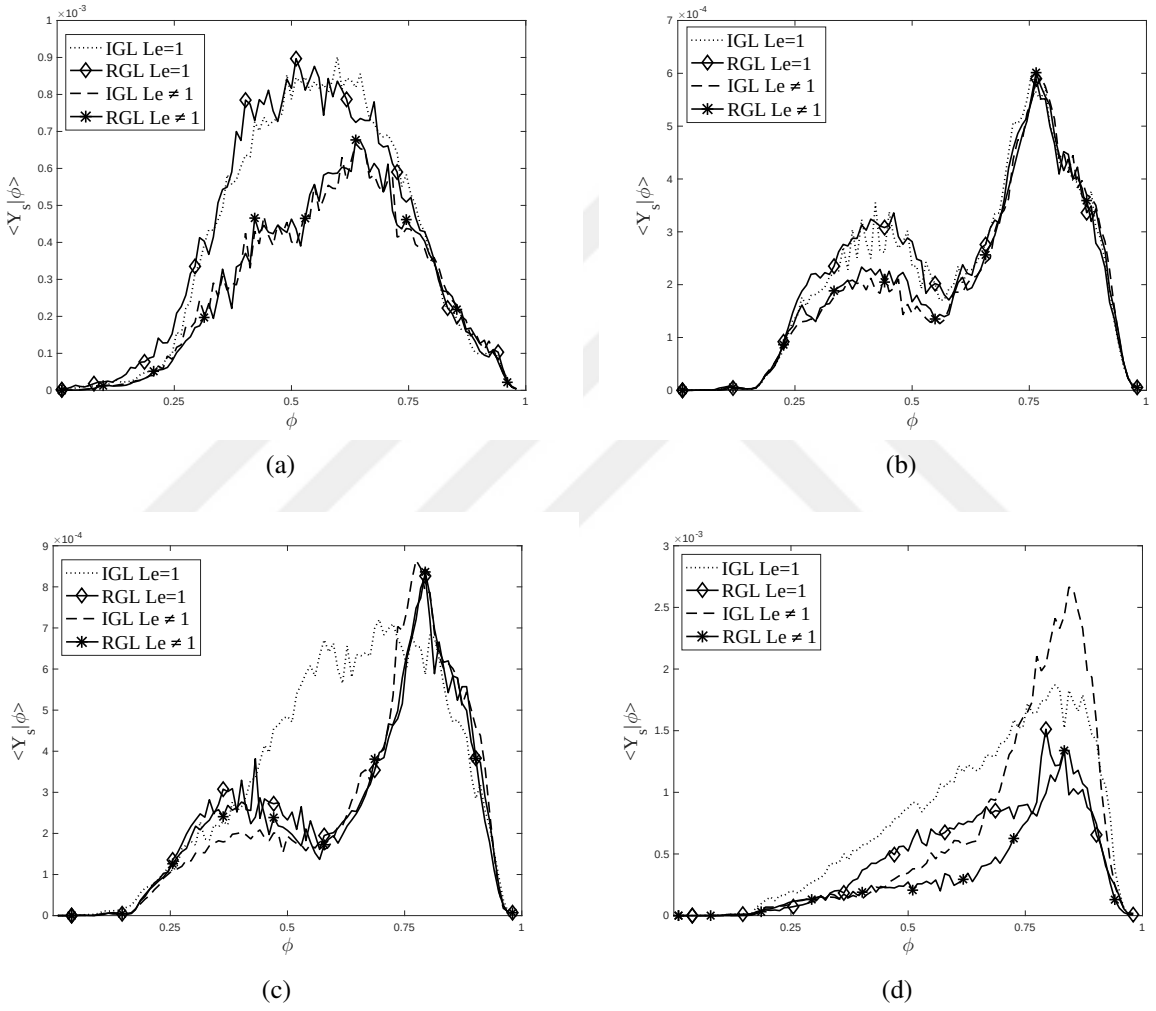


Figure 3.33: The comparison of $< Y_s|\phi >$ for different ambient pressures, the EOS models and diffusion assumptions flames (a) 1 atm, (b) 5 atm, (c) 10 atm and (d) 35 atm ambient pressures.

EOS coupling with the unity Le #, the soot oxidation process is under-predicted. In addition to that, although the RGL EOS coupling with the unity Le # assumption dramatically under-predicts the soot oxidation process.

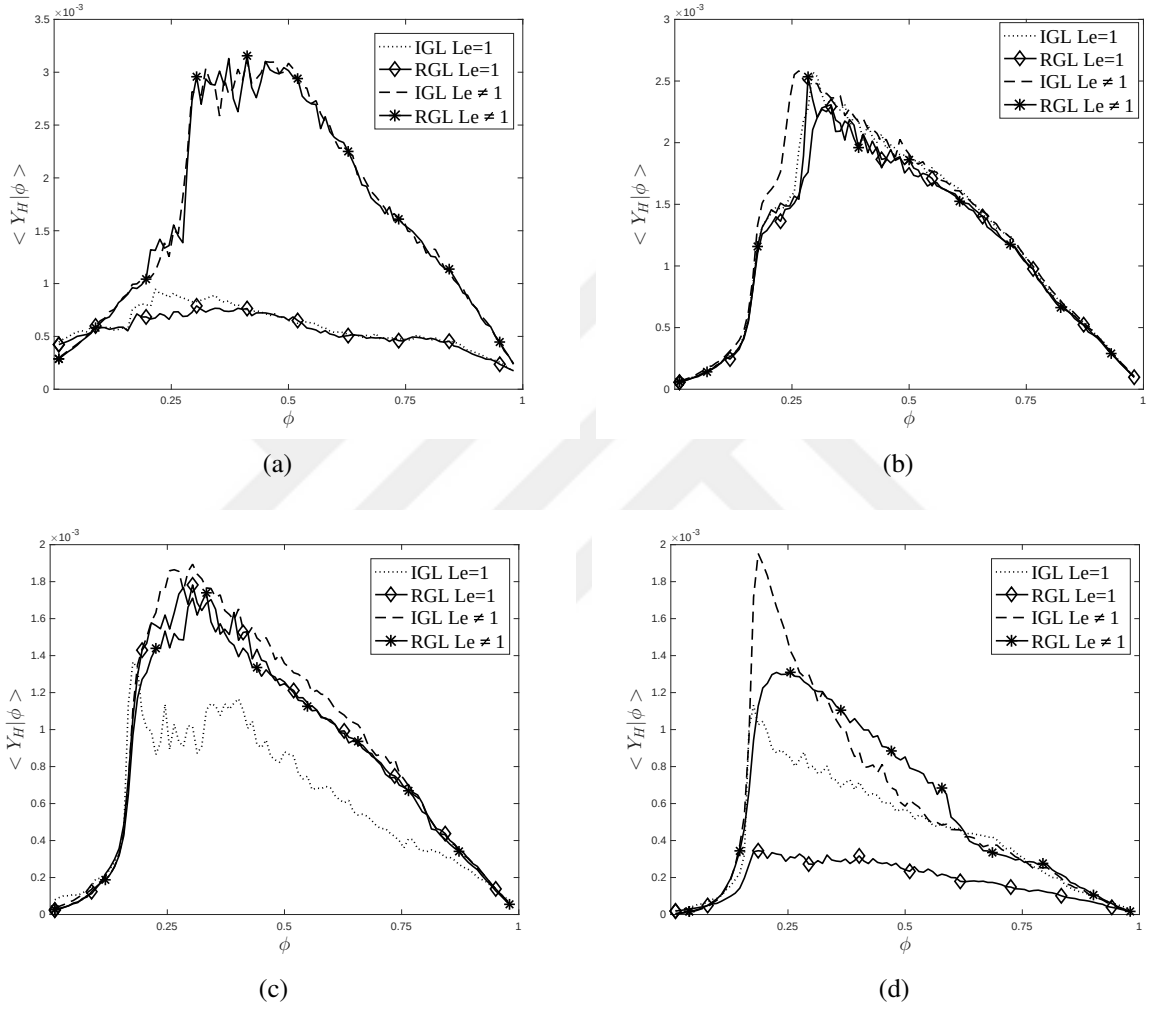


Figure 3.34: The comparison of $< Y_H|\phi >$ for different ambient pressures, the EOS models and diffusion assumptions flames (a) 1 atm, (b) 5 atm, (c) 10 atm and (d) 35 atm ambient pressures.

Figure 4.35 displays the Y_{OH} predictions for the ambient pressures of 1, 5, 10 and 35 atm flames. While in Figure 4.35 (b) and (c) the Y_H predictions are captured acceptably well for 5 and 10 atm flames, Figure 4.35 (a) and (d) reveal the incapabilities of the IGL EOS model and the unity Le # assumption on the predictions of 1 and 35 atm flames.

Figure 4.36 exhibit the Y_{CO} predictions of the RGL and the IGL EOS model employing either

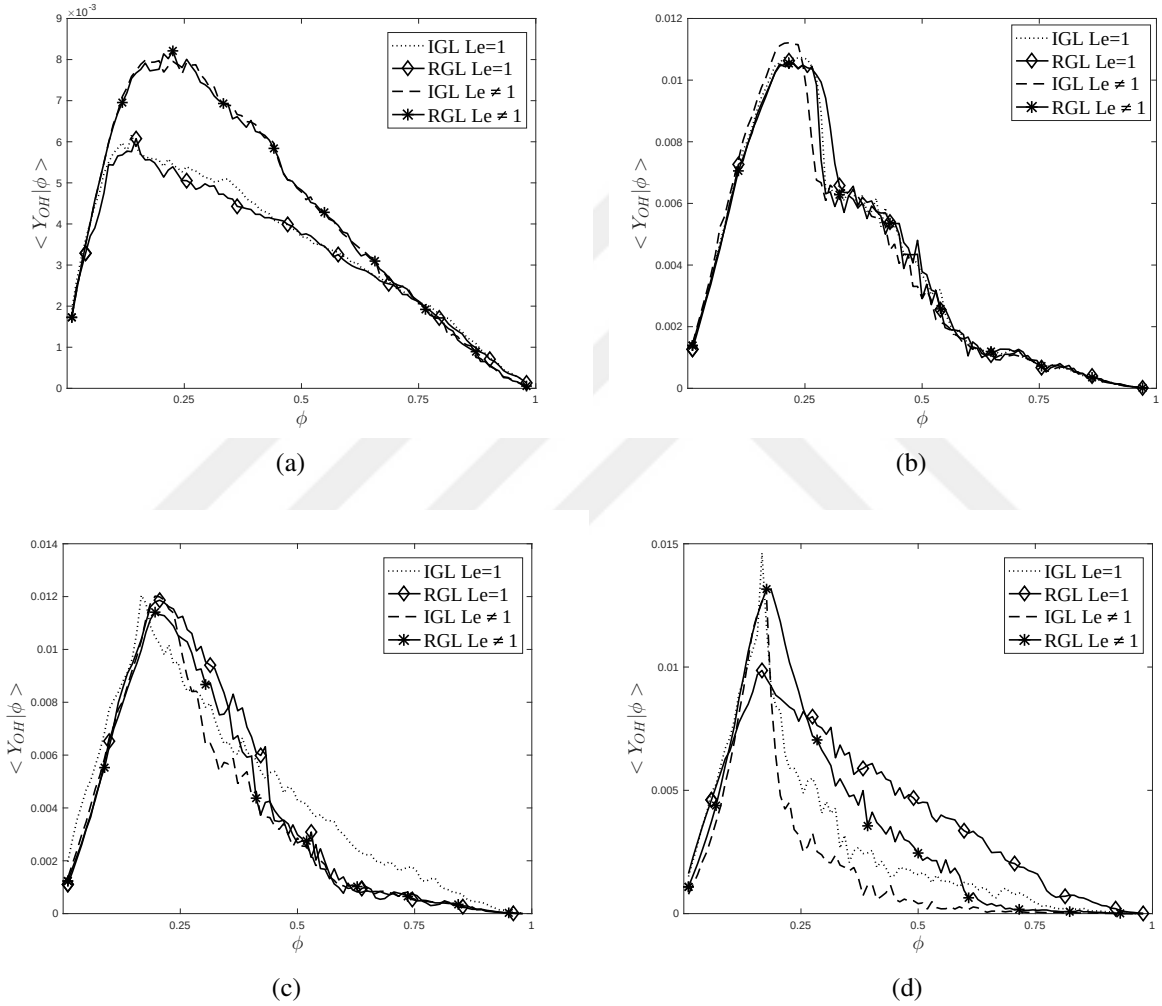


Figure 3.35: The comparison of $< Y_{OH}|\phi >$ for different ambient pressures, the EOS models and diffusion assumptions flames (a) 1 atm, (b) 5 atm, (c) 10 atm and (d) 35 atm ambient pressures.

non-unity or unity Le # assumptions. Figure **??** (a) confirms the trends have been observed in the previously on soot oxidation steps in atmospheric pressure flames. Again, Y_{CO} predictions possess the similar trends in all flames proving that soot properties are highly temperature dependent ([see Figure 4.31 (b)]). The predictions of Y_{CO} in 10 atm flames help us to have better understanding on the soot load predictions of the IGL EOS model coupled with the unity Le # assumption confirming that soot oxidation process is highly weakened by the choice of the EOS and the unity Le # assumption. Lastly, Figure 4.36 (d) display the under-predictions of the Y_{CO} supporting the idea of that the soot oxidation process weakens by increasing ambient pressure when the EOS model coupled with the unity Le # assumption.

Lastly, in this work we focus on the Le numbers of the both EOS models adopted to create adiabatic flame DSN data. The list of the species pair numbers and species pair are listed in the Table **??**. Figure 4.37 - 4.40 investigate the Le numbers calculated conditioned on the mixture fraction, $< Le|\phi >$. The red horizontal lines in each figure aim to indicate the $< Le|\phi >$ numbers for each species pair how different from unity Le number for each simulation considered in the current work. For all cases the species pairs of 1, 10,11, 12, 13, 14 and 17 possess higher values than 1, while the rest stay below the red line for all the considered cases. Figure 4.37 shows the $< Le|\phi >$ numbers for the atmospheric pressure flames. As stated before, for the atmospheric pressure flames employing the IGL EOS might be safe with a non-unity Le number assumption. Figure 4.38 displays the $< Le|\phi >$ numbers for 5 atm flames for each EOS model employed in this work, while the $< Le|\phi >$ numbers are slightly increased for most of the species pairs. The $< Le|\phi >$ numbers are to be indifferent from each other for each cases. As increasing ambient pressure, an increasing trend for the $< Le|\phi >$ are present in the 10 atm flames as well, while the $< Le|\phi >$ numbers of the RGL and the IGL EOS models still exhibit indifferent behavior from each others. Lastly, the $< Le|\phi >$ numbers for previously mentioned species pair gets $\approx$ 50% larger than the atmospheric pressure flames, and possessing the $< Le|\phi >$ numbers smaller than unity for the rest of the species pairs.

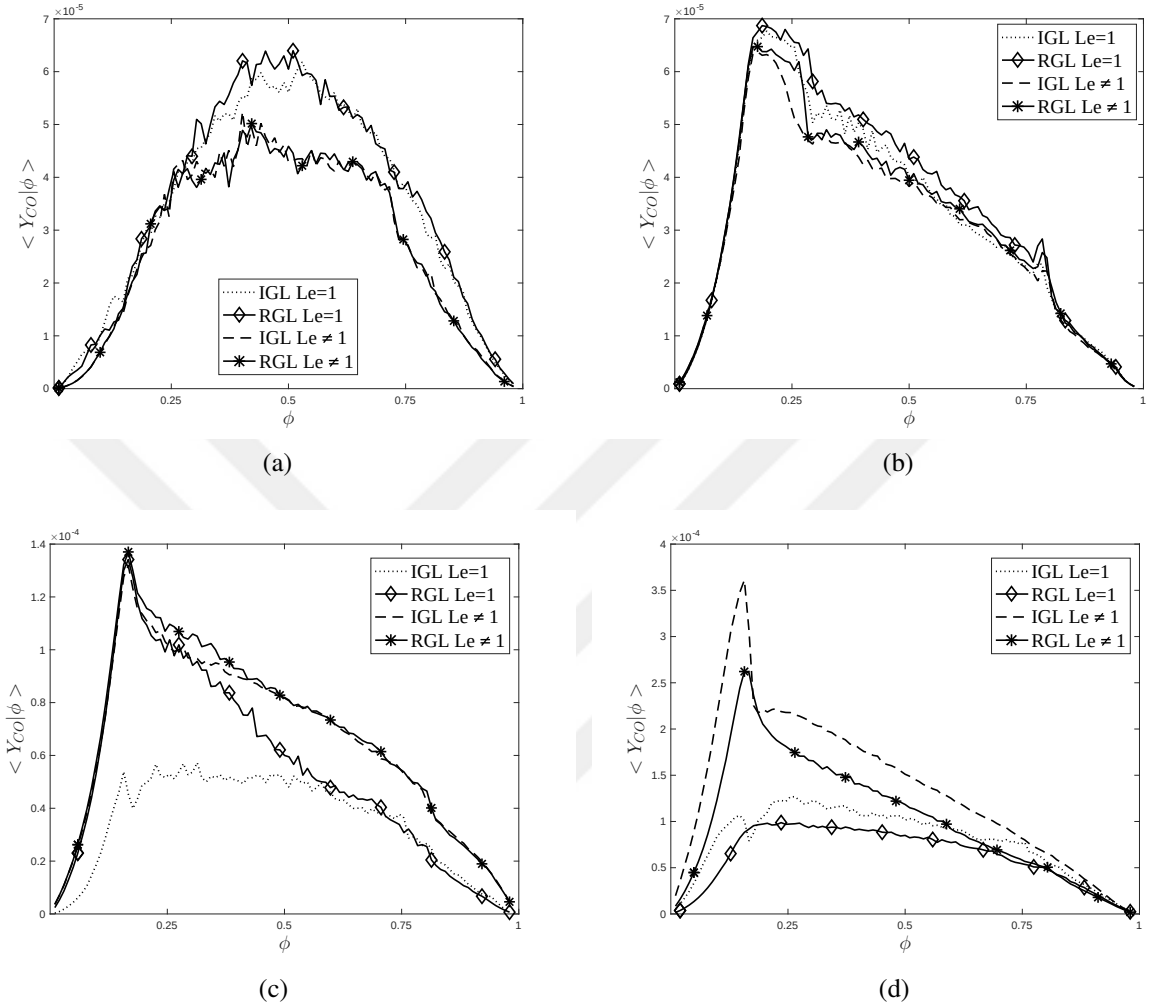


Figure 3.36: The comparison of $< Y_{CO}|\phi >$ for different ambient pressures, the EOS models and diffusion assumptions flames (a) 1 atm, (b) 5 atm, (c) 10 atm and (d) 35 atm ambient pressures.

Species Pair #	Species Pair	Species Pair #	Species Pair	Species Pair #	Species Pair	Species Pair #	Species Pair
1	$O_2 - C_{12}H_{24}$	10	$C_{12}H_{24} - OH$	19	$CO_2 - CO_2$	28	$O - CO_2$
2	$O_2 - CO$	11	$C_{12}H_{24} - O$	20	$CO_2 - H$	29	$O - H$
3	$O_2 - OH$	12	$C_{12}H_{24} - H_2O$	21	$CO_2 - N_2$	30	$O - N_2$
4	$O_2 - O$	13	$C_{12}H_{24} - CO_2$	22	$OH - O$	31	$H_2O - CO_2$
5	$O_2 - H_2O$	14	$C_{12}H_{24} - H$	23	$OH - H_2O$	32	$H_2O - H$
6	$O_2 - CO_2$	15	$C_{12}H_{24} - N_2$	24	$OH - CO_2$	33	$H_2O - N_2$
7	$O_2 - H$	16	$CO_2 - OH$	25	$OH - H$	34	$CO_2 - H$
8	$O_2 - N_2$	17	$CO_2 - O$	26	$OH - N_2$	35	$CO_2 - N_2$
9	$C_{12}H_{24} - CO$	18	$CO_2 - H_2O$	27	$O - H_2O$	36	$H - N_2$

Table 3.3: The list of Species Pair # and Species Pair.

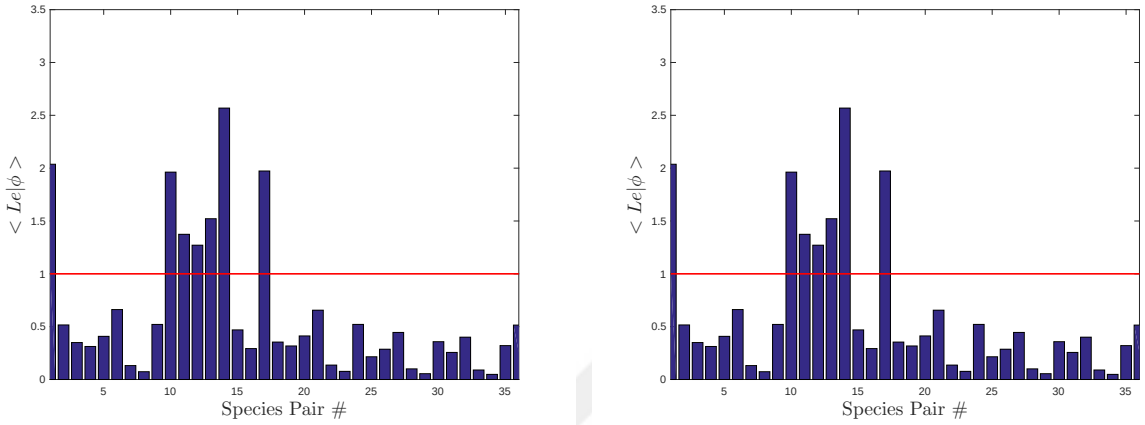


Figure 3.37: On the left the RGL EOS model and on the right the IGL EOS model Le # calculated for the adiabatic atmospheric pressure flame.

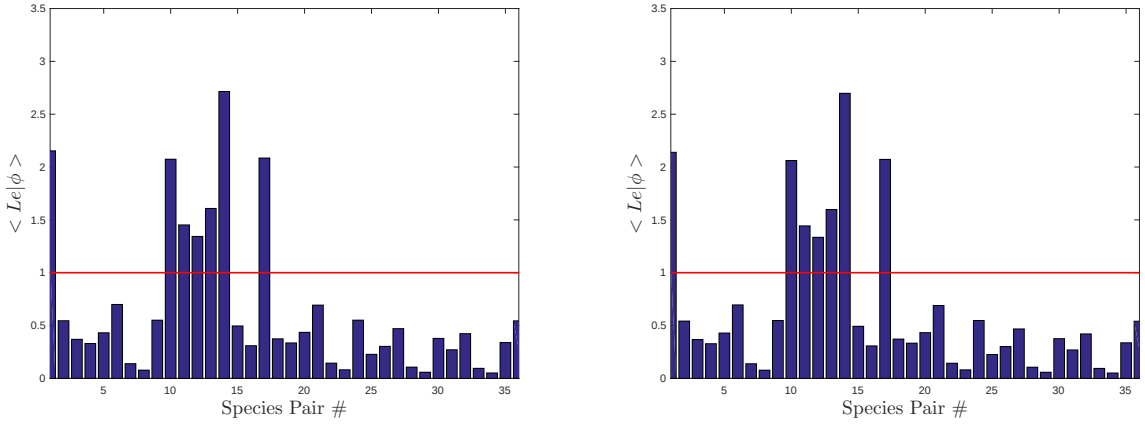


Figure 3.38: On the left the RGL EOS model and on the right the IGL EOS model Le # calculated for the adiabatic 5 atm pressure flame.

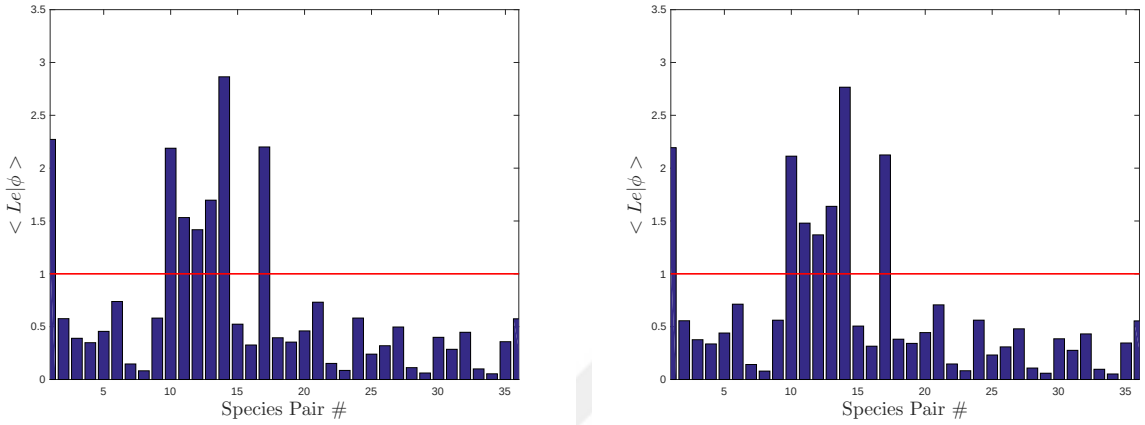


Figure 3.39: On the left the RGL EOS model and on the right the IGL EOS model Le # calculated for the adiabatic 10 atm pressure flame.

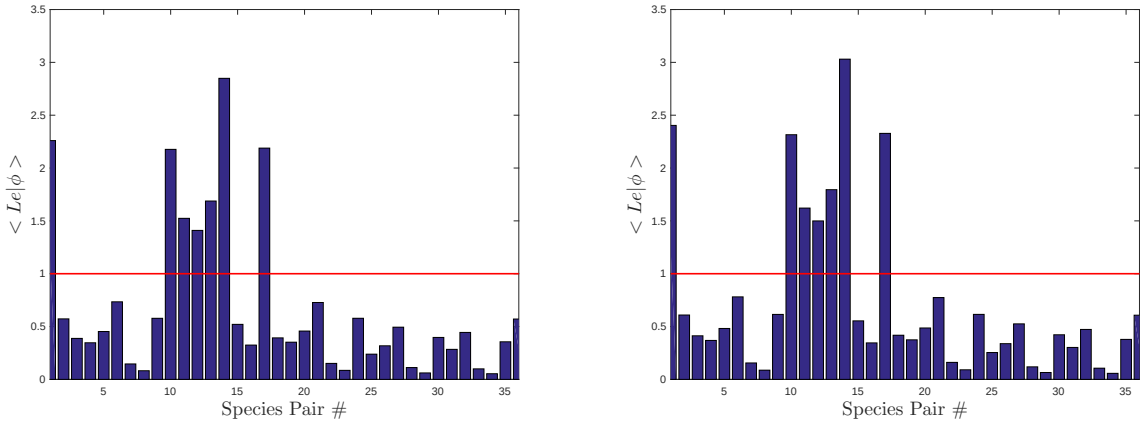


Figure 3.40: On the left the RGL EOS model and on the right the IGL EOS model Le # calculated for the adiabatic 35 atm pressure flame.

Bibliography

[1] http://www.sandia.gov/TNF/radiation.html.

[2] D.J. Glaze A.J. Chandy and S.H. Frankel. A hybrid large eddy simulation filtered mass density function for the calculation of strongly radiating turbulent flames. *J. Heat Transfer*, 131, 2009.

[3] X.S. Bai, M. Balthasar, and L Fuchs. Detailed soot modeling in turbulent jet diffusion flames. *Twenty-Seventh Symp. (Int.) Combust./Combust. Inst.*, pages 1623–1630, 1998.

[4] V. Bergmann, W. Meier, and W Wolff, D.Stricker. Application of spontaneous raman and rayleigh scattering and 2d lif for the characterization of a turbulent $CH_4/H_2/N_2$ jet diffusion flame. *Appl. Phys. B*, 66:489–502, 1998.

[5] F. Bisetti, G. Blanquart, M.E. Mueller, and H. Pitsch. On the formation and early evolution of soot in turbulent nonpremixed flames. *Combust. Flame*, 159:317–335, 2012.

[6] F. Bisetti, G. Blanquart, and H. Pitsch. Direct numerical simulation of soot formation in turbulent non-premixed flames. *Cent. Turb. Res. Ann. Res. Br*, pages 437–449, 2008.

[7] G. Borghesi and J. Bellan. *A priori* and *a posteriori* investigations for developing large eddy simulations of multi-species turbulent mixing under high-pressure conditions. *Phys. Fluids*, 27:035117, 2015.

[8] D Bradley, G. Dixon-Lewis, S.E. Habik, and E.M.J. Mushi. The oxidation of graphite powder in flame reaction zones. *Proc. of 20th Int. Symp. Combust.*, pages 931–940, 1984.

[9] N.W. Bressloff. *CFD predictions of coupled radiation heat transfer and soot production in turbulent flames*. PhD thesis, Cranfield Uni., 1996.

[10] B.S.Haynes and H.Gg. Wagner. Soot formation. *Prog. Energy Combust. Sci.*, 7:229–273, 1981.

[11] M. Chamecki. Modeling subgrid scale heat fluxes in the neutral and stratified atmospheric boundary layer. *J. Turbul.*, 11:1–16, 2010.

[12] J. Charentenay and A. Ern. Multicomponent transport impact on turbulent premixed h_2/o_2 flames. *Combust. Theor. Model.*, 6:439–462, 2002.

[13] M.R.J. Charest. *Numerical Modeling of Sooting Laminar diffusion flames at elevated pressures and micrograviti*. PhD thesis, University of Toronto, Department of Mechanical Engineering, Dec 2011.

[14] M.R.J. Charest, C.P.T. Groth, and O.L. Gulder. A computational framework for predicting laminar reactive flows with soot formation. *Combust. Theor. Model.*, 14:793–825, 2010.

[15] M.R.J. Charest, C.P.T. Groth, and O.L. Gulder. Numerical and experimental study of soot formation in laminar diffusion flames burning simulated biogas fuels at elevated pressures. *Combust. Flame*, 161:2678–2691, 2014.

[16] M.R.J. Charest, H.I. Joo, O.L. Gulder, and C.P.T. Groth. Experimental and numerical study of soot formation in laminar ethylene diffusion flames at elevated pressures from 10 to 35 atm. *Proc. Combust. Inst*, 33:549–557, 2011.

[17] P. J. Coelho and M. G. Carvalho. Modeling of soot formation and oxidation in turbulent diffusion flames. *J. Thermophys Heat Transfer*, 9:644–652, 11995.

[18] C.F. Curtiss and R.B. Bird. Multicomponent diffusion. *Ind. Eng. Chem. Res.*, 38:2515–2522, 1999.

[19] M.C. Drake, M. Lapp, M.C. Penney, and S. Warshaw. Measurements of temperature and concentration flucmations in turbulent diffusion flames using pulped raman spectroscopy. *Eighteenth Symp. (Int.) Combust./The Combust. Inst.*, 18:1521–1531, 1981.

[20] R. B. Edelman and P. T. Harsha. Laminar and turbulent gas dynamics in combustors-current status. *Prog. Energy Combust. Sci.*, 4:1–62, 1978.

[21] G. Erlebacher, M.Y. Hussaini, C.G. Speziale, and T.A. Zang. Toward the large-eddy simulation of compressible turbulent flows. Technical report, Institute for Computer Applications in Science and Engineering NASA Langley Research Center, Hampton,VA, October 1990.

[22] J.D. Felske and C.L. Tien. The use of the milne-eddington absorption coefficient for radiative heat transfer in combustion systems. *ASME J. Heat Transfer*, 99:458–465, 1977.

[23] J. Foster. Thermal diffusion coefficient modeling for high pressure combustion simulations. Master's thesis, Clemson University, May 2007.

[24] J. Foster. *A Priori Anlaysis of Subgrid Scalar Phenomena and Mass Diffusion Vectors in Turbulent Hydrogen-Oxygen Flames*. Masters Thesis, Clemson University, Department of Mechanical Engineering, 2009.

[25] J. Foster. *On Simulation and Modeling of Turbulent Non-Premixed Reacting Shear Flames at Low and High Pressure*. PhD thesis, Clemson University, 2012.

[26] J. Foster and R.S. Miller. Fundamentals of high pressure combustion. In M Lackner, editor, *High Pressure Processes in Chemical Engineering*, pages 53–75. ProcessEng Engineering GmbH, 2010.

[27] J. Foster and R.S. Miller. A priori analysis of subgrid mass diffusion vectors in high pressure turbulent hydrogen/oxygen reacting shear layer flames. *Phys. Fluids*, 075114.-24, 2012.

[28] J. Foster and R.S. Miller. Survey of turbulent combustion models for large eddy simulations of propulsive flowfields. *AIAA Paper 2015-1379*, 2015.

[29] A. Garo, R. Said, and R. Borghi. Model of soot formation: Coupling of turbulence and soot chemistry. In H. Bockhorn, editor, *Soot Formation in Combustion*, pages 527–550. Springer Berlin Heidelberg, 1994.

[30] P. Givi. Filtered density function for subgrid scale modeling of turbulent combustion. *AIAA Paper*, 44(1):16–23, 2006.

[31] S.J. Harris and A.M. Weiner. Determination of the rate constant for soot surface growth. *Combust. Sci. Technol.*, 32:267–275, 1983.

[32] K. Harstad and J. Bellan. Interactions of fluid oxygen drops in fluid hydrogen at rocket chamber pressures. *Int. J. Heat Mass Transfer*, 41:3551–3558, 1998.

[33] K. Harstad and J. Bellan. Isolated fluid oxygen drop behavior in fluid hydrogen at rocket chamber pressures. *Int. J. Heat Mass Transfer*, 41:3537–3550, 1998.

[34] K.G. Harstad, R.S. Miller, and J. Bellan. Efficient high pressure state equations. *AIChE J.*, 43(6):1605–1610, 1997.

[35] D.C Haworth. Progress in probability density function methods for turbulent reacting flows. *Prog. Energy Combust. Sci*, pages 168–259, 2010.

[36] K.A. Hoffman and S.T. Chiang. *Computational Fluid Dynamics Volume I*. Engineering Education System, 2004.

[37] F.A. Jaberi, R.S. Miller, Mashayek. F., and P. Givi. Differentail diffusion in binary scalar mixing and reaction. *Combust. Flame*, 109(4):561–577, 1997.

[38] C.A. Kennedy and M.H. Carpenter. Several new numerical methods for compressible shear-layer simulations. *Appl. Numer. Math.*, 14:397–433, 1994.

[39] I.M. Kennedy. Models of soot formation and oxidation. *Prog. Energy Combust. Sci.*, 23:95–132, 1997.

[40] A. Kronenbljrg and R.W. Bilger. Modelling differential diffusion in nonpremixed reacting turbulent flow: Model development. *Combust. Sci. Technol.*, 166:195–227, 2001.

[41] G.E Lau, G.H. Yeoh, V. Timchenko, and J.A. Reizes. Application of dynamic global-coefficient subgrid scale models to turbulent natural convection in an enclosed tall cavity. *Phys. Fluids*, 24, 2012.

[42] C.W. Lautenberger, J.L. Ris, N.A. Dembsey, J.R. Barnett, and H.R. Baum. A simplified model for soot formation and oxidation in CFDs simulation of non-premixed hydrocarbon flames. *Fire Safety J.*, 40:141—176, 2005.

[43] M. Lesieur and O. Metais. New trends in large eddy simulations of turbulence. *Annu. Rev. Fluid Mech.*, 28:45–82, 1996.

[44] K. M. Leung, R. P. Lindstedt, and W. P. Jones. A simplified reaction mechanism for soot formation in nonpremixed flames. *Combust. Flame*, 87:289–305, 1991.

[45] D Lignell, J Chen, and P Smith. Three-dimensional direct numerical simulation of soot formation and transport in a temporally evolving nonpremixed ethylene jet flame. *Combust. Flame*, 155:316–333, 2008.

[46] D Lignell, J Chen, P Smith, T Lu, and C Law. The effects of flame structure on soot formation and transport in turbulent nonpremixed flames using direct numerical simulation. *Combust. Flame*, 151:2–28, 2007.

[47] D. O. Lignell, J. H. Chen, P. J. Smith, T. F. Lu, and C. K. Law. Direct numerical simulation of soot formation and transport in non-premixed turbulent ethylene flames. *5th US Combustion Meeting 2007,Combustion Institute*, (520-554), 2007.

[48] D.O Lignell. *Direct Numerical Simulation of Soot Formation and Transport in Turbulent Nonpremixed Ethylene Flames*. PhD thesis, The Univesity of Utah, 2008.

[49] F. Liu, H. Guo, G.J. Smallwood, and O.L. Gulder. Effects of gas and soot radiation on soot formation in a coflow laminar ethylene diffusion flame. *J. Quant. Spectrosc. Radiat. Transfer.*, 73:409–421, 2002.

[50] F. Liu, K.A. Thompson, H. Guo, and G.J. Smallwood. Numerical and experimental study of an axisymmetric coflow laminar methane-air diffusion flame at pressures between 5 and 40 atmospheres. *Combust. Flame*, 146:456–471, 2006.

[51] F. Liu, K.A. Thomson, H. Guo, and J. Smallwood. Numerical modeling of a laminar axisymmetric coflow methane/air flame at pressures between 5 and 20 atm. *Combustion Institute / Canadian Section, Spring Technical Meeting, Kingston, Ontario, Canada, May 9-12, 2004*, 2004.

[52] N. Malik, T. Lovas, and F. Mauss. The effect of preferential diffusion on the soot initiation process in ethylene diffusion flames. *Flow Turbulence Combust*, 87:293–312, 2011.

[53] E. Masi, J. Bellan, K. Harstad, and N. Okong'o. Multi-species turbulent mixing under supercritical-pressure conditions: modeling, direct numerical simulation and analysis revealing species spinodal decomposition. *J. Fluid Mech.*, 721:578–626, 2013.

[54] A.R. Masri, R.W. Dibble, and R.S. Barlow. Chemical kinetic effects in nonpremixed flames of H_2/CO_2 fuel. *Combust. Flame*, 91:285–309, 1992.

[55] F Mauss, K. Netzell, and Lehtiniemi H. Aspects of modeling soot formation in turbulent diffusion flames. *Combustion Science and Technology*, 178:1871–1885, 2006.

[56] W. Meier, A. O. Vyrodov, V. Bergmann, and W. Stricker. Simultaneous $raman/LIF$ measurements of major species and NO in turbulent H_2/Air diffusion flames. *Appl. Phys. B*, 63:79–90, 1996.

[57] R.S. Miller. Long time mass fraction statistics in stationary compressible isotropic turbulence at supercritical pressure. *Phys. Fluids*, 12(8):2020–2032, 2000.

[58] R.S. Miller, K.G. Harstad, and J. Bellan. Direct numerical simulation of supercritical fluid mixing layers applied to heptane-nitrogen. *J. Fluid Mech.*, 436:1–39, 2001.

[59] M.F. Modest. *Radiative Heat Transfer*. Academic Press, 2003.

[60] J.B. Moss, C.D. Stewart, and K.J. Young. Modeling soot formation and burnout in a high temperature laminar diffusion flame burning under oxygen-enriched conditions. *Combust. Flame*, 101:491–500, 95.

[61] J. Nagle and R.F. Strickland-Constable. Oxidation of carbon between 1000-2000 $^{\circ}C$. *Proc. Fifth Conference on Carbon*, 1:161–164, 1962.

[62] K.G. Neoh, J.B. Howard, and A.F. Sarofim. Soot oxidation in flames. In D.C. Siegla and G.W. Smith, editors, *Particulate Carbon: Formation During Combustion*, pages 261–277. Springer US, 1981.

[63] V. Nilsen and G. Kosaly. Differential diffusion in turbulent reacting flows. *Combust. Flame*, pages 493–513, 1999.

[64] J. Pallares and L. Davidson. Large eddy simulation of turbulent heat transfer in stationary and rotating square ducts. *Phys. Fluids*, 14:2804–2816, 2002.

[65] S. Palle. *On Real Gas and Molecular Transport Effects in High Pressure Mixing and Combustion*. PhD thesis, Clemson University, 2006.

[66] S. Palle and R.M. Miller. Analysis of high pressure hydrogen, methane, and heptane laminar diffusion flames: Thermal diffusion factor modeling. *J. Appl. Mech.*, 73:5–15, 2006.

[67] S. Palle and R.S. Miller. Analysis of high-pressure hydrogen, methane, and heptane laminar diffusion flames: Thermal diffusion factor modeling. *Combust. Flame*, 151:581 – 600, 2007.

[68] S. Palle, C. Nolan, and R.S. Miller. On molecular transport effects in real gas laminar diffusion flames at large pressure. *Phys. Fluids*, 17:103–601, 2005.

[69] S.C. Paul and M.C. Paul. Radiative heat transfer during turbulent combustion process. *nt. Commun. Heat Mass Transfer*, 37:1–6, 2010.

[70] U. Piomelli. Large-eddy simulations: Present state and future directions. *AIAA Paper 98-0534*, 1998.

[71] H. Pitsch. Large-eddy simulation of turbulent combustion. *Annu. Rev. Fluid Mech.*, 38:453–482, 2006.

[72] H. Pitsch, O. Oesjardins, G. Balarac, and M. Ihme. Large-eddy simulation of turbulent reacting flows. *Prog. Aero. Sci.*, 44:466–478, 2008.

[73] H. PITSCH, E. RIESMEIER, and N. PETERS. Unsteady flamelet modeling of soot formation in turbulent diffusion flames. *Combust. Sci. Technol.*, 158:389–406, 2000.

[74] HEINZ PITSCH and HELFRIED STEINER. Scalar mixing and dissipation rate in large-eddy simulations of non-premixed turbulent combustion. *Proceedings of the Combustion Institute*, 28:41–49, 2000.

[75] F. Porte-Agel, C Meneveau, and M.B. Parlange. Some basic properties of the surrogate subgrid scale heat flux in the atmospheric boundary layer. *Boundary Layer Meteorol.*, 88:425–444, 1998.

[76] F. Porte-Agel, M.B. Parlange, C Meneveau, and W.E Eichinger. A priori field study of the subgrid scale heat fluxes and dissipation in the atmospheric surface layer. *J. Atmos. Sci.*, 58:2673–2698, 2001.

[77] A. Garo R. Said and R. Borghi. Soot formation modeling for turbulent flames. *Combust. Flame*, 108:71–86, 1997.

[78] J.J. Riley. Review of large eddy simulation of non-premixed turbulent combustion. *J. Fluids Eng.*, 128:209–215, 2006.

[79] R. J. Santoro, T. T. Yeha, J. J. Horvatha, and H. G. Semerjiana. The transport and growth of soot particles in laminar diffusion flames. *Combust. Sci. Technol.*, 53:89–115, 1986.

[80] R. Sarlak, M. Shams, and R. Ebrahimi. Numeircal solution of soot formation in a turbulent diffusion flame: comparison among three soot formation models. *Proc. Ints. Mech. Eng. Part C: J. Mech. Eng. Sci.*, 226:1290–1301, 2012.

[81] L.C. Selle, N.A. Okong'o, J. Bellan, and K.G. Harstad. Modeling of subgrid-scale phenomena in supercritical translational mixing layers: a priori study. *J. Fluid Mech.*, 593:57–91, 2007.

[82] L. L. Smith, R.W. Dibble, L. Talbot, R.S. Barlow, and C. Carter. Laser raman scattering measurements of differential diffusion in nonreacting and reacting laminar and turbulent jet flows. *31st Aerospace Sciences Meeting, AIAA*, 1993.

[83] M.D. Smooke, M.B. Long, B.C Connely, M.B. Colket, and R.J. Hall. Soot formation in laminar diffusion flames. *Combust. Flame*, 143:613–628, 2005.

[84] M.D. Smooke, C.S. Mcenally, L.D. Pfefferle, R.J. Hall, and M.B. Colket. Computational and experimental study of soot formation in a coflow, laminar diffusion flame. *Combust. Flame*, 117:117–139, 1999.

[85] C.H. Sohn and S.H. Chung. Effect of pressure on the extinction, acoustic pressure response, and no formation in diluted hydrogen-air diffusion flames. *Combust. Flame*, 121:288–300, 2000.

[86] C.D. Stewart, K.J. Syed, and J.B. Moss. Modelling soot formation in non-premixed kerosine-air flames. *Combust. Sci. Technol.*, 75:211–226, 1991.

[87] G. Janiga T. Chittipotula and D. Thevenin. Soot radiation models for turbulent nonpremixed ethylene air flames. *Proc. European Combust. Meeting*, 2011.

[88] E.S. Taskinoglu and J. Bellan. A posteriori study using a DNS database describing fluid disintegration and binary-species mixing under supercritical pressure: Heptane and nitrogen. *J. Fluid Mech.*, 645:211–254, 2009.

[89] E.S. Taskinoglu and J. Bellan. Subgrid-scale models and large-eddy simulation of oxygen stream disintegration and mixing with a hydrogen or helium stream at supercritical pressure. *J. Appl. Mech.*, 679:156–193, 2011.

[90] K.K. Varanasi. *Direct Numerical Simulation of a Fuel Multicomponent Droplet Laden Mixing Layer*. MS thesis, Clemson University, Department of Mechanical Engineering, May 2001.

[91] R. Vasudevan. Thermal diffusion coefficient modeling for high pressure combustion simulations. Master's thesis, Clemson University, 2007.

[92] R. Viskanta and M.P. Menguc. Radiation heat transfer in combustion systems. *Prog. Energy Combust. Sci.*, 13:97–160, 1987.

[93] B.C. Wang, E. Yee, J. Yin, and J. Bergstrom. A general dynamic linear tensor diffusivity subgrid-scale heat flux model for large-eddy simulation of turbulent thermal flows. *Num. Heat Trans., Part B*, 51:205–227, 2007.

[94] T. S. Wang. Thermophysics characterization of kerosene combustion. *J. Thermophys Heat Transfer*, 15:140–147, 2001.

[95] T.-S. Wang, R.C. Farmer, and R.B. Edelman. Turbulent combustion kinetics for complex hydrocarbon fuels. *AIAA-89-0486*, 1988.

[96] W.P. Wang and R.H. Pletcher. On the large eddy simulation of turbulent channel flow with significant heat transfer. *Phys. Fluids*, 8:3354–3366, 1996.

[97] C.S. Yoo and H.G. Im. Transient soot dynamics in turbulent nonpremixed ethylene air counterflow flames. *Proc. Combust. Inst*, 31:701–708, 2007.

[98] K.J. Young. *Soot formation in turbulent vaporised kerosine/air jet flames at elevated pressure*. PhD thesis, Cranfield Inst. Tech., 1993.

[99] K.J. Young, C.D. Stewart, and J.B. Moss. Soot formation in turbulent nonpremixed kerosine-air flames burning at elevated pressure: experimental measurement. *Twenty-Fifth Symp. (Int.) Combust./The Combust. Inst.*, 25:609–617, 1994.

[100] M.J. Thomson Z. Wen, S. Yun and M.F. Lightstone. Modeling soot formation in turbulent kerosene/air jet diffusion flames. *Combust. and Flame*, 135:323–340, 2003.

[101] Q. Zhang, H. Guo, G.J. Smallwood, and M.J. Thomson. Implementation of an advanced fixed sectional aerosol dynamics model with soot aggregate formation in a laminar methane air coflow diffusion flame. *Combust. Theor. Model.*, 12:621–641, 2008.

[102] W. Zhang and Q. Chen. A new filtered dynamic subgrid-scale model for large eddy simulation of indoor airflow. *Proceeding of the 6th International IBPSA Conference*, pages D–03, 1999.

[103] M.J. Zimberg, S.H. Frankel, J.P. Gore, and Y.R. Sivathanu. A study of coupled turbulent mixing, soot chemistry, and radiation effects using the linear eddy model. *Combust. Flame*, 113:454–469, 1998.